1-1-2012

Numerical Simulation Of Thermodiffusion Subjected To Different Gravity Fields

Ahmad Khoshnevis
Ryerson University

NUMERICAL SIMULATION OF THERMODIFFUSION SUBJECTED TO DIFFERENT GRAVITY FIELDS

By
Ahmad Khoshnevis

B.Sc. in Mechanical Engineering, University of Tabriz, Tabriz, Iran, 2009

A thesis
presented to Ryerson University
in partial fulfillment of the
requirement for the degree of
Master of Applied Science
in the Program of
Mechanical Engineering

Toronto, Ontario, Canada, 2012

AUTHOR'S DECLARATION

I hereby declare that I am the sole author of this thesis. This is a true copy of the thesis, including any required final revisions, as accepted by my examiners.

I authorize Ryerson University to lend this thesis to other institutions or individuals for the purpose of scholarly research.

I further authorize Ryerson University to reproduce this thesis by photocopying or by other means, in total or in part, at the request of other institutions or individuals for the purpose of scholarly research.

I understand that my thesis may be made electronically available to the public.

ABSTRACT

Numerical Simulation of Thermodiffusion Subjected to Different Gravity Fields

Ahmad Khoshnevis
Master of Applied Science
Mechanical and Industrial Engineering, 2012
Ryerson University, Toronto, On, M5B 2K3, Canada

In this work, a typical thermodiffusion experiment on a binary mixture is simulated numerically using a two-dimensional computational fluid dynamics (CFD) code. Three scenarios for gravity have been studied: residual, pure oscillatory, and microgravity micro-accelerations.

It was found that less separation of mixture components in the presence of strong gravity fields is due to the formation of buoyancy-driven flows. For the case of pure oscillatory gravity, the effects of the frequency and amplitude are discussed in detail. A critical vibrational Rayleigh number is proposed above which the diffusion process is highly affected by the external excitation.

For the case of the microgravity environment, quasi-steady accelerations and g-jitter, both of which are found on the International Space Station, have been considered. Results show g-jitter has a minimal effect on the thermodiffusion experiment. The effects of the residual gravity field were also found to be insignificant in stimulating a strong convection flow.

ACKNOWLEDGEMENTS

Special appreciation to Prof. Ziad Saghir; for being such a great supervisor; for providing me with the opportunity; for all of his guidance, support and trust.

I would like to thanks my family for all of their supports. Also I thank my friends in the microgravity laboratory at Ryerson and in particular Mr.Amirhosein Ahadi, Mr.Armin Kianian and Dr. Morteza Eslamian. I am grateful to Dr. Marcus Dejmek from the Canadian Space Agency for providing me with the acceleration data and the insightful discussions. This work has been financially supported by the Canadian Space Agency.

I would like to dedicate this work to all the researchers who have crossed the borders and committed responsibly to the science even though they might have been following other goals.

TABLE OF CONTENT

List of Tables

List of Figures

Nomenclature

A	Amplitude of forced vibration [m]
C	Scale factor for acceleration data [-]
c	mass fraction of a chemical species [-]
c_p	Specific heat of the mixture [J/kgK]
D_c	Diffusion coefficient [m^2/s]
D_T	Thermodiffusion coefficient [$m^2/(s.K)$]
F	Body force in momentum equation [N]
f	Frequency of the oscillatory gravity [Hz]
g	Gravity acceleration [m/s^2]
Gs	Gershuni number [-]
k	Thermal conductivity of mixture [w/(m.K)]
p	Pressure [Pa]
Ra	Rayleigh number [-]
Sr	Separation rate [-]
S_T	Soret coefficient [1/K]
t	Time [s]
T	Temperature [°C]
u	x-component velocity [m/s]
v	y-component velocity [m/s]
V^*	provisional velocity [m/s]
$\vec{V}$	Velocity vector [m/s]
x,y	Independent variables [m]

Greek symbols

α	Angle between gravity vector and applied temperature gradient [°]
β_T	Thermal expansion coefficient [1/K]
β_c	Volumetric concentration expansion coefficient [-]
ρ	Density [kg/m^3]
υ	Kinematic viscosity [m^2/s]
μ	Dynamic viscosity [Pa.s]
χ	Thermal diffusivity [m^2/s]

η	Normal unit on the boundary [m]
Γ	Boundary indication
ΔT	Temperature difference between hot and cold wall [°C]

Subscripts

~	Average value
0	Initial (reference) state
c	Cold wall
cri	Critical
h	hot wall
st	Static (residual)
vib	Vibratory
x	x direction
y	y direction

Superscripts

$\rightarrow$	Vector notation
*	Dimensionless (normalized)
n	current time
n+1	next time

Chapter 1 Introduction

1.1 Background and basic concepts of thermodiffusion

The Soret effect is the tendency of a mixture of two or more components to separate due to a spatial temperature difference. This effect acts in contrast to molecular diffusion (Fick's law), in which components spread in the domain to provide a uniform distribution or concentration of species. This interesting phenomenon was first systematically observed by Soret [1] when he noticed the formation of a non-uniform composition of a salt solution in a heated tube. He claimed that there is a tendency for the components of the mixture to separate under the influence of a temperature gradient across the tube. This phenomenon is also known as thermodiffusion, thermophoresis, or the Ludwig-Soret effect. More technically, the Soret effect is a cross-effect in irreversible thermodynamics that assumes the components and heat fluxes between the hot and cold region to be a linear function of both the concentration differences and the temperature difference [2].

As mentioned earlier, the mass flux caused by thermodiffusion acts against diffusion. There is an opposition between these two forces, the sum of which determines the separation of the components of a mixture. Empirically, the Soret coefficient determines the equilibrium condition between these two forces, and is the ratio of the thermodiffusion coefficient to the molecular diffusion coefficient [3].

For further clarification, consider the mass flux of a component in a mixture, given by:

$$J_m = -\rho D \nabla c - \rho D_T^* \nabla T \tag{1-1}$$

in which J_m is the mass flux of one species, ρ is the density of the mixture, ∇c and ∇T are the concentration and temperature gradients, respectively, and D and D_T^* are the molecular diffusion and thermodiffusion coefficients, respectively. This equation shows that the mass flux of components is the sum of the molecular diffusion process (depending on the gradient of concentration) and the thermodiffusion effect, which is dependent on the temperature gradient and thermodiffusion coefficient(D_T^*).

In most studies, the initial concentration of the molecular species is also considered in the thermodiffusion coefficient, thus:

$$D_T^* = D_T(1 - c_0)c_0 \tag{1-2}$$

in which c_0 is the initial concentration of the carrier component.

At the steady-state condition, the mass flux becomes zero. By having $J_m = 0$ in Eq(1-1), the following equation is achieved:

$$\nabla c = -\mathrm{S_T c_0}(1 - \mathrm{c_0})\nabla T \tag{1-3}$$

where $\mathrm{S_T}$ is the Soret coefficient, which is defined as the ratio between the thermodiffusion and diffusion coefficients:

$$\mathrm{S_T} = {}^{D_T}/_{D} \tag{1-4}$$

Eq(1-3) shows that for a certain thermal gradient, the Soret coefficient determines the maximum separation of components. The time that is needed to reach the steady state is related to the diffusion coefficient and is known as the diffusion time.

The Soret coefficient can be positive or negative. It is positive when the heavier component migrates to the cold side and is negative when the heavier component migrates toward the hot side. A sign change of the Soret coefficient at different component ratios is well-known for a number of small-molecule fluid mixtures. An example of these mixtures is the mixture of water and isopropanol, which has been studied by several authors [4]. The mixture with a mass fraction of 90% water has a negative Soret coefficient and magnitude of $-7.08 \times 10^{-3}\ 1/K$, while the same mixture with mass concentration of 50% water exhibits a positive Soret coefficient with value of $5.45 \times 10^{-3}\ 1/K$. This is in line with the typical order of magnitude of the Soret coefficient for aqueous solutions or organic mixtures, which is $|ST| \sim 10^{-3} - 10^{-2} K^{-1}$" [5].

Research in the field of thermodiffusion can be divided into two major areas. The first category is devoted to the study of the thermodiffusion coefficient for different mixtures. Using analytical modeling or experiments, the researchers propose models or values for the thermal diffusion coefficient (Soret coefficient) for mixtures at different concentrations and temperatures. The other research field is numerical analyses of thermodiffusion, which implements the analytical models or experimental correlations

and simulates fluid-flow characteristics in more complex situations. Furthermore, the numerical analyses are also used to discuss the credibility of experimental studies by measuring the contribution of buoyancy (secondary) flows in a process.

In the last two decades, advancements in space exploration have offered a uniquely accessible and controllable microgravity environment to perform scientific experiments in unmanned spacecraft or even space stations. By having the International Space Station (ISS) as the most complex human structure in outer space, there is a distinct opportunity to conduct various scientific experiments (including fluid experiments) in a microgravity environment. The main advantage of the space platform is the reduced gravity field. In terms diffusion experiments, the reduced gravity would result in elimination of buoyancy-driven flows (natural convection). However, convection still exists in the space platforms due to unavoidable sources of vibration. Thus the credibility of experiments performed on these platforms should be evaluated to show by how much the results deviate from the ideal, zero-gravity condition from this induced convection.

Prior to discussing the literature on thermodiffusion, it is necessary to provide some information about microgravity environments and discuss their characteristics.

1.2 Microgravity environment

As described earlier, fluid experiments that are performed in a microgravity environment benefit from the condition of reduced gravity. Therefore, having proper knowledge of characteristics of the microgravity environment is necessary. In this section typical microgravity environments are described.

A microgravity environment is defined as when the acceleration conditions of a platform is almost balanced by the inertial force. The platform can either be an orbital facility such as ISS or an airplane in parabolic flight. In practice, a pure zero-gravity field is impossible and there is always a residual value for the acceleration level. For a microgravity environment, the residual gravity is many orders of magnitude smaller than the sea level gravitational acceleration value known as g_0. Typically, the residual gravity acceleration for platforms orbiting in Low Earth Orbit (LEO) is on the order of $10^{-6} g_0$[6].

The distinct behavior of fluids in a micro gravity environment is the main interest behind the fluid experiments. The absence of hydrostatic pressure gradient in these environments may result in different phenomena including the formation of large droplets and liquid bridges [7]. Moreover, as a result of the elimination of the buoyancy force the processes are governed by diffusion rather than convection. The former consequence can be utilized for performing thermodiffusion experiments.

1.2.1 Classification of microgravity environments

Ideal zero-g conditions are established when the gravity force is balanced by the inertial forces. Thus the changes of velocity magnitude or direction along the trajectory must be equal to the gravitational acceleration of Earth. In that respect the typical microgravity platforms can be classified as follow:

1.2.1.1 Drop tower, drop tubes, sounding rockets

In these platforms, the gravity of Earth is neutralized by an accelerating vertical motion that can be either be an upward decreasing speed or a downward increasing speed. For case of sounding rockets, rockets are used to carry instruments from 50 to 1,500 kilometers above the earth's surface. The average flight time is less than 30 minutes, and is typically between 5 and 20 minutes [8]. The rocket consumes its fuel during the first stage of the flight, then separates and falls away, leaving the payload to complete an arc and return to the ground using a parachute. The main advantage of using sounding rockets is their long microgravity duration (~ 15 minutes). Moreover, compared to large orbital satellite-based experiments, sounding rockets are inexpensive.

1.2.1.2 Airplane in parabolic flight

In these platforms an aircraft is used to provide the sensation of weightlessness by following an (approximately parabolic) elliptical flight path relative to the centre of the Earth. While following this flight path, the aircraft and its payload are in free fall at certain points. A typical trajectory of a zero-g airplane is shown in Figure 1-1. Generally, this method can provide up to 30 seconds of microgravity at a cost in the range of a few dollars per pound.

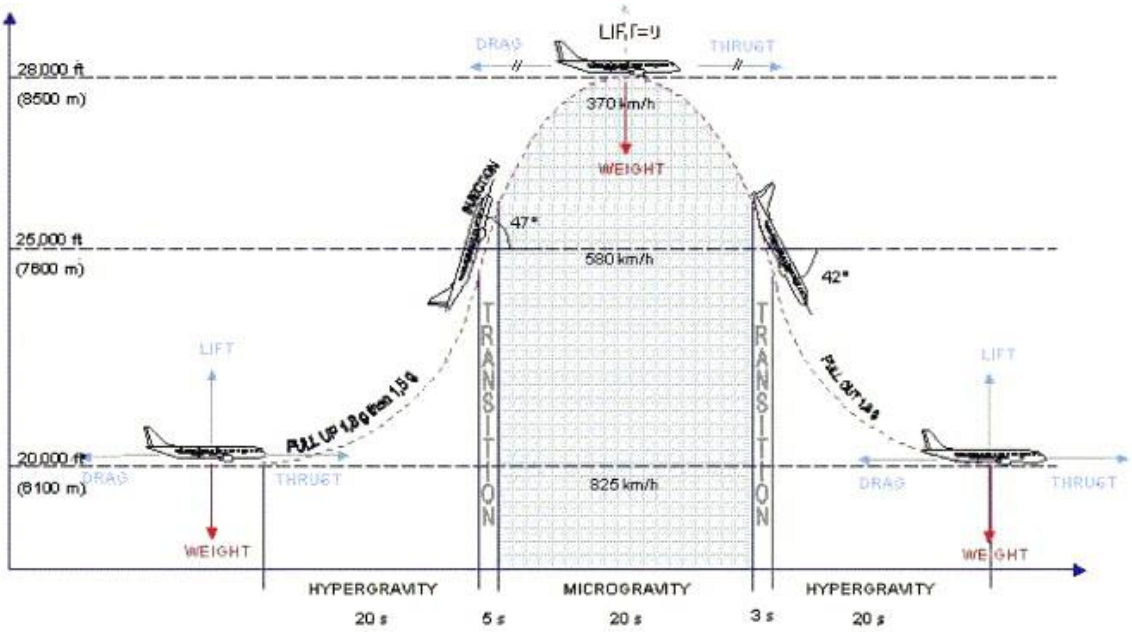

Figure 1-1:Schematic view of the trajectory of parabolic flights [9]

1.2.1.3 Point platforms

A point platform commonly refers to a spacecraft or orbiter that is moving in a circular orbit that makes the gravity force balanced by the centrifugal force. There have been numerous unmanned scientific satellites that fit into this definition. FOTON-M, for instance, is a series of robotic spacecraft used by Russia and the European Space Agency for research conducted in a microgravity environment of Earth orbit [10].

Beside of scientific satellites, the International Space Station (ISS) has proved a promising platform for microgravity investigations with human supervision. Performing science experiments has always been a part of space platforms. Previously, science experiments were conducted on the MIR space station and the space shuttles. Nevertheless, none of those platforms were as suitable as the ISS, because of the wide array of available facilities on board. At this moment, the ISS serves as a microgravity and space environment research laboratory in which crew members conduct experiments in biology, human biology, physics, astronomy, meteorology, and other fields [11]. The ISS orbits the earth in a polar orbit (between 388 and 401 km from the surface of the earth), with an average orbital speed of 7,706.6 m/s.

1.2.2 Disturbance in zero-g conditions

In all actual microgravity environments, there will be non-zero resultant accelerations that disturb the ideal zero-g condition. Generally, the non-zero difference can be separated into steady (or quasi-steady) part (g_S), which is known as residual-g, and a time dependent part $g(t)$ called g-jitter. With respect to the orbiting platforms, the disturbances can be due to two types of sources: the "External forces" which act on the platform and change its momentum, and "Internal forces" that cause a gravity gradient including mass dislocation inside the platform (e.g., crew activity, motion of mechanical parts inside facilities).

As far as the International Space Station disturbances are concerned, we can identify the following categories [6]:

1.2.2.1 Steady (or quasi –steady) residual-g

These include aerodynamic drag ($1 \sim 3 \times 10^{-7} g_0$) and radiation pressure $10^{-8} g_0$ (that are periodic with the orbit). For points distant from the centre of mass, gravity gradient and centrifugal forces due to rotation of the ISS exist.

1.2.2.2 Pulse-like (single or compensating) accelerations

The main sources of these accelerations are the thruster firing ($10^{-4} g_0$), crew activities ($10^{-3} \sim 10^{-2} g_0$), or external forces including docking/berthing ($10^{-4} g_0$), and micrometeorite impacts ($10^{-9} g_0$).

1.2.2.3 Periodic, high frequency accelerations

This category is the main concern of fluid experiments and exists due to on-board machineries and natural frequencies excited by external or internal actions ($10^{-6} < gg0 < 10-2\,; 0.1Hz < f < 300Hz$.

The former two accelerations are known as "g-jitter", which refers to random high-frequency vibrations. These vibrations are measured by probes mounted on the space station. The residual gravity does not change significantly over time. The predicted value of g_S (for the ISS) is on the order of 0.5μg for the US Lab, between 1 and 1.8μg for the European COF, and about 2μg for the Japanese module (JEM). The schematic picture of the ISS is illustrated in Figure 1-2 indicating the residual acceleration for different modules. The methodology for collecting vibration data onboard ISS will be discussed in Chapter 2.

As discussed above, the currently available microgravity environment provides a unique environment for fluid experiments. A few such experiments have been devoted to thermodiffusion. FOTON satellites (launch 2002–2007) were used for thermodiffusion experiments [12]. On the ISS, the Columbus laboratory has been the host of various fluid-flow experiments since its activation in 2008 [13]. Some of the experiments were dedicated to measurements of multi-component liquid mixtures and metallic melts that are impossible to determine (with a comparable accuracy) on the ground. However, there have been a great number of discussions about the effects of micro-accelerations that might affect what are considered to be nearly ideal results. This topic will be further discussed in the following sections.

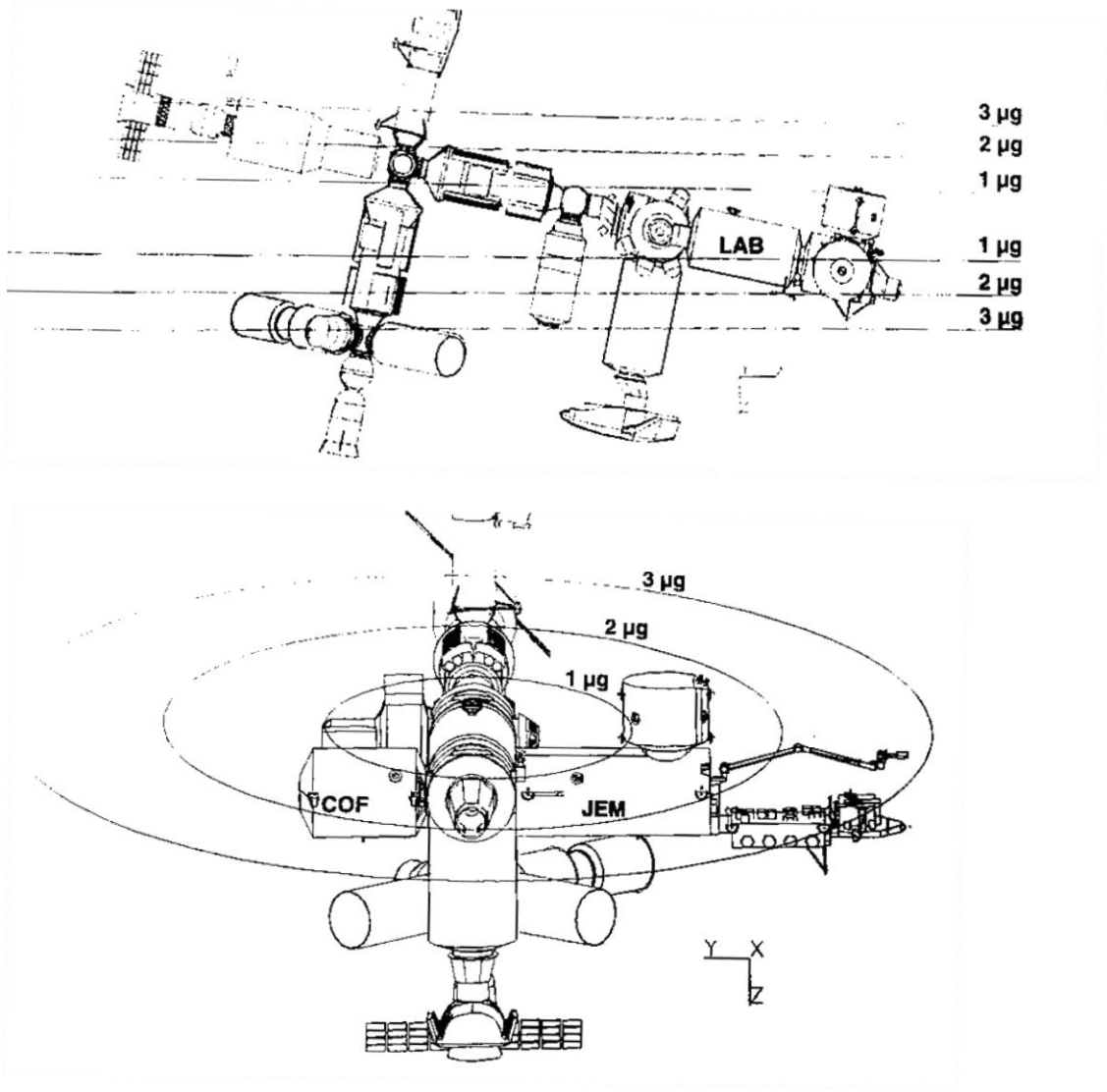

Figure 1-2: Approximate residual-g on the ISS[6]**.**

1.3 Literature review on thermodiffusion

Thermodiffusion is an unique phenomenon. Due to its small scale, thermodiffusion is usually neglected in many engineering mass transfer application where the process is dominated by inertial (turbulence) forces. Thermodiffusion is inherently a slow-process that is governed by diffusion. Nevertheless, its role in the compositional variation of fluids in oil reservoirs, mineral migrations [14], and even mass transport in living matter [3] has been demonstrated. The main cause of having non-uniform distribution of species in the oil reservoirs is thermodiffusion-driven mass flux. As described earlier, thermodiffusion is governed by the thermal diffusion coefficient which is a material property of the mixture. Like the diffusion coefficient, it is defined for each two components of a mixture. In this section, different approaches and investigations in the field of thermodiffusion are addressed and discussed.

1.3.1 Investigations to determine the Soret coefficient

The main objective of this research field is to predict the thermal coefficient or Soret coefficient value for certain mixtures. There have been numerous studies on this by different researchers. In the case of dilute gases, this phenomenon has been successfully explained and correlated with the aid of kinetic theory [15]. However, in spite of different proposed theories, thermodiffusion is not fully understood for condensed gases and other fluid mixtures. This has raised increasing scientific and engineering interests in recent years.

Molecular dynamics simulations have been used as a powerful and promising tool for evaluation of thermal diffusion coefficient (Soret) for different mixtures [16]. Fundamentally, physical movements of atoms and molecules are simulated *in silico*. The atoms and molecules are allowed to interact for a period of time, providing perspective into their motion. Many publications on the study of the Soret effect using molecular dynamics methods have appeared in the last decades. Simon *et al.* [17] were able to compute the Soret coefficient in a methane/decane mixture with reasonable agreement using molecular dynamics. Niero-Draghi *et al.* [18] employed the same method and successfully estimated the sign change in the thermal diffusion coefficient of water/alcohol mixtures.

Although the use of molecular dynamics simulation has been a promising approach, there is considerable interest for theoretical modeling in order to catch the essence of the thermodiffusion phenomenon.

Many researchers have attempted to formulate the thermodiffusion coefficients. Some of these important theories were based on irreversible thermodynamics by Hasse [19] and the kinetic theory of irreversible thermodynamics by Dougherty and Drickmer [20]. The model by Dougherty and Drickamer appears to put forward a good connection between thermodiffusion and equilibrium thermodynamics properties. Nevertheless, their work has been limited by the lack of effective methods to obtain required thermodynamic properties. This deficiency has been treated by Shukla and Firoozabadi [21]. In their approach, the thermodynamics properties of hydrocarbon mixtures are obtained from the Peng-Robinson Equation of State (PR-EoS).

In another model, Kempers [2] has suggested a thermostatic strategy based on statistical mechanics for the estimation of thermodiffusion. The single assumption in Kempers model is that a steady state will be achieved as the number of microstates in a system at a conditional maximum.

The lattice model by Luettmer-Strathmann [22] is another method following a thermostatic approach. In this approach, the fluid mixture in a two-chamber system is assumed to be of a cubic lattice configuration. Without too much effort, one can obtain the expression for the canonical partition function of this system. And consequently, the canonical partition function with two chambers at different temperatures will lead to the probability of finding different species in the mixtures and thus an expression for the Soret coefficient.

Eslamian and Saghir have published a series of investigations on the theoretical evaluation of thermodiffusion characteristics in binary and ternary mixtures [23-25], DNA thermophoresis [26], semiconductors and liquid metal mixtures, and dilute polymer solutions [27,28]. Eslamian has summarized the advancements in thermodiffusion in liquid mixtures in one recent publication [29]. It was stated that more experimental studies for binary and ternary hydrocarbon mixtures are needed to confirm the current theoretical models.

For the case of water/alcohol mixtures (associating mixtures), in spite of numerous experimental data, the theoretical modeling is still challenging due to the complex molecular interaction. They also mentioned molecular dynamics simulation (MD) to be a promising tool for evaluation of Soret characteristics for different mixtures.

One of the interesting subjects in thermodiffusion that has been a concern to theoretical models is to trace the sign change of Soret coefficient with the compositional or temperature-dependent variation. These phenomena have been observed in some mixtures, especially associating mixtures with hydrogen bounding [30]. When the Soret coefficient changes its sign, the mass flow due to the thermodiffusion effect is reversed. For instance, for the water/isopropanol mixture the Soret coefficient is negative for a water portion of 90% by mass. In this condition the water migrates toward the hot side. When the water portion is decreased50% by mass, water moves toward the cold wall as a result of a positive Soret coefficient [4].

Some of the approaches were successful in predicting this peculiar behaviour. The most successful example is the molecular dynamics study by Nieto-Draghian and co-workers [18]. They successfully estimated the sign change in the thermal diffusion factor for some water alcohol mixtures using MD simulation. Their work suggests that the interaction among molecules is a dominant factor for the Soret effect in aqueous associating mixtures. Pan *et al.* also proposed a successful method for the evaluation of the Soret coefficient in alkanol solutions which predict this sign change with good accuracy [31]. In another approach Abbasi *et al.* predicted such a change for linear-chain hydrocarbon binary mixtures [32].

Evaluation of the Soret coefficient in multicomponent mixtures is another important topic. The interest is rather due to the perspective of the oil industry in which the application of thermodiffusion is particularly relevant to multi-component mixtures (crude oil). Finding thermodiffusion coefficients in such multi-component mixtures is experimentally impossible using conventional experimental tools. Thus, a good theoretical model is in demand. Meanwhile, only two theoretical models, which are developed by Kempers [2] and Firoozabadi and co-workers [21,33] have been extended to multi-component mixtures. However, neither of them has been validated by experiments.

1.3.1.1 Experimental investigations

The current work has no focus on the experimental methods and the details of these techniques are not discussed here. The reader is referred to more informative articles regarding the experimental studies of thermodiffusion [34]. However, in this section some fundamental information is provided about different experimental methodologies.

The Soret coefficient can also be obtained experimentally. Numerous techniques and apparatus have been developed for that purpose during the last century. The main obstacle in the experiments is due to the small size of the parameters of thermodiffusion. Thus, accurate measurements are critical for such experiments. Furthermore, certain precautions should be taken in order to avoid any source of disturbance in the system that might affect the results. Natural convection is the main concern in thermodiffusion experiments, and it can be caused by the spatial density gradient as well as by imperfections of the experimental technique. The buoyancy-driven flows might affect the measurements by inducing mixing in the system that fundamentally is in competition with the Soret effect.

Different experimental approaches can be subdivided into two major categories. The first category is the classical methods, due to their basic functionality. This category includes the classical Soret cell [35], thermogravitational column [5], and two-chamber thermodiffusion cell [34]. The other group uses optical methods for the determination of Soret coefficient. Optical methods have been used to study the thermodiffusion process in liquid mixtures, polymer solutions, and colloidal suspensions [34]. The examples of these methods are as laser beam deflection techniques, thermal diffusion forced Rayleigh scattering, and thermal lens techniques.

Optical methods are more recent and provide significant advantages. The most important advantage of these techniques is that they are non-intrusive and the transient processes can be surveyed with high-resolution accuracy [36,37]. There has been considerable interest in applying optical interferometry techniques in measuring thermodiffusion. This method has been used in one of the most expensive experimental studies of thermodiffusion in microgravity environment onboard the International Space Station (ISS), named IVIDIL, which will be discussed in the next section.

1.3.2 IVIDIL project

In 2000, a projected named IVIDIL (Influence of Vibration in Diffusion in Liquids) [38] proposed to the European Space Agency (ESA) by an international team including the Microgravity research Center of ULB (Brussels, Belgium), the Microgravity laboratory of Ryerson University (Toronto, Canada), and the Institute of Continuous Media Mechanics UB RAS (Perm, Russia). The project proposed to study the influence of vibrations on the measurement of diffusion and Soret coefficients in well-known two-component mixtures (water/isopropanol) by monitoring the temperature and concentration fields. Optical Digital Interferometry and Particle Image Velocimetry (PIV) are employed in this experiment.

The project started in October 2009 and completed in January 2010. In total, 55 experimental runs (41 original and 14 re-runs) were conducted. The first 26 runs were devoted to the mixture of 10% IPA[1] and 90% water, a mixture which has a negative Soret coefficient. The rest of the 29 runs used the mixture of 50% IPA and 50% water (positive Soret coefficient).

IVIDIL project has been insightful in understanding the complex process of thermal diffusion in the presence of controlled vibrations. Detailed study of the IVIDIL project is still in progress.

1.3.2.1 IVIDIL experimental apparatus and procedure

IVIDIL apparatus consists of three main parts: An interferometry system in combination with equipment for digital recording of the phase information, the diffusion cell, and the vibrational platform.

The apparatus was installed in a special facility known as MGS[2]. This facility offers an enclosed 255-liter (9 cubic foot) work area accessible to the crew through glove ports and to ground-based scientists through real-time data links.

---

[1] The abbreviation form of isopropanol

[2]Microgravity Science Glovebox

Because the work area is sealed and held at a negative pressure, the crew can manipulate experimental hardware and samples without the danger of small parts, particulates, fluids, or gasses escaping into the open laboratory module. The MGS is located in the European Space Agency's Columbus Orbital Facility (COF) laboratory module. Figure 1-3 is a picture of IVIDIL experimental apparatus mounted in the MGS.

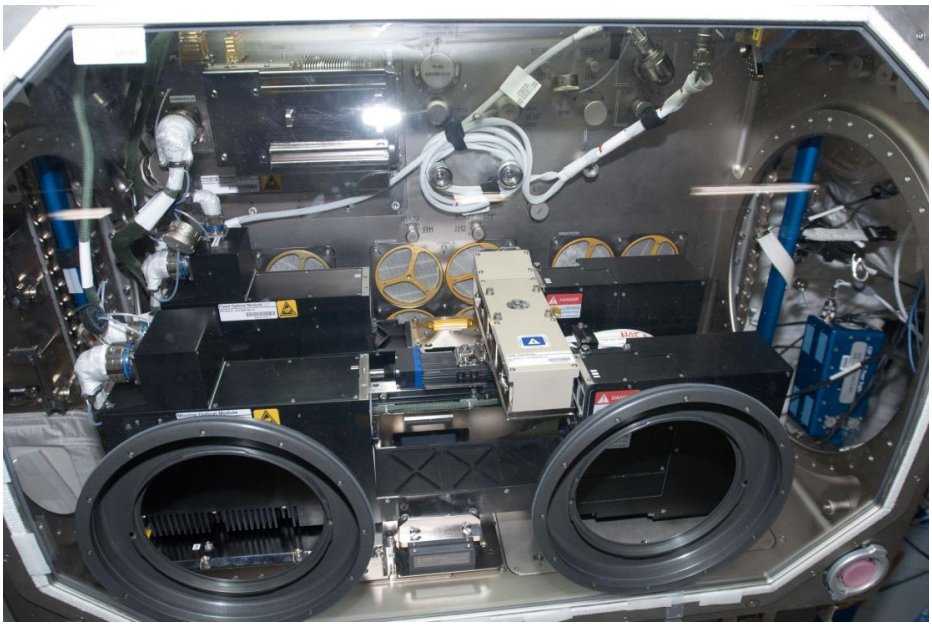

Figure 1-3: IVIDIL installed in the Microgravity Science Glovebox (MGS)

Each experimental run was performed in two steps. During the first step, a concentration gradient was established by imposing a temperature gradient across the experimental cell. Due to the Soret effect, the concentration profile was slowly generated in an initially homogeneous binary mixture. After 12h, the temperature gradient was removed and diffusion occurred during the next 6 hours. External vibrations of different amplitudes and frequencies were applied during the whole 18 hours. The light beam of a constant frequency He-Ne laser was expanded by the spatial filter and then passed through the beam splitter where it was divided into two beams of equal intensity. One of the beams went through the experimental cell and the other bypassed it. After passing mirrors, the object and reference beams interfered with each other at a second beam splitter. Finally, interference fringes were captured by the CCD camera sensors. The images were sent to the earth-based laboratories and analyzed through image processing to obtain the variation in the temperature and composition of the mixture.

1.3.2.2 IVIDIL experimental runs

As described earlier, in the IVIDL project 55experimental runs were performed, in which 26 of them were for an IPA/water mixture with water mass percentage of 90%. Since this study was focused on this mixture (10%IPA, 90%water), the same related runs of IVIDIL projects are of interest. The first 25 runs of the project are shown in Table 1-1. As shown, most of the runs were conducted in the presence of forced vibration. Only Run2 and Run2R were accomplished in the pure microgravity environment of ISS. These runs are informative in terms of indicating the effects of random g-jitter vibrations. The results of the IVIDIL project have been published in a few investigations [39], and the post-processing of this insightful experiment is still in progress [40].

Table 1-1: List of IVIDL experimental runs for IPA:water (90:10 wt%)

Run number	Start Time	Frequency [Hz]	Amplitude of vibration [mm]	Temperature differences [°C]	Vibration Rayleigh number [-]
1	5-10-09 18:36	0.5	70	5	32
2	7-10-09 11:37	0	0	5	0
3	8-10-09 6:12	2	25	5	64
4	9-10-09 0:48	1	50	5	64
5	2-11-09 9:06	2	44	10	801
6	3-11-09 14:52	2.8	25	10	507
7	4-11-09 9:26	2	33	10	451
8	27-10-09 11:30	1	70	10	507
9	14-10-09 15:21	0.5	70	10	127
10	15-10-09 9:56	0.2	70	10	20
11	28-10-09 14:59	2	58	10	1393
12	29-10-09 19:48	0.05	70	10	1.3
13	19-10-09 19:48	2	52	15	2518
14	20-10-09 14:23	2.8	31	15	1754
15	21-10-09 8:58	2	61	15	3465
16	22-10-09 3:33	1	70	15	1141
17	22-10-09 22:08	2	27	15	679
18	5-11-09 4:18	2	57	15	3026
19	5-11-09 22:54	2	48	15	2146
Ext8	13-10-09 8:52	1	70	10	507
15R	10-11-09 19:20	2	61	15	3465
2R	11-11-09 13:58	0	0	5	0
12R	12-11-09 8:34	0.05	70	10	1.3
13R	16-11-09 14:19	2	52	15	2518

1.3.3 Fluid-flow investigation

The main objective of fluid-flow investigations is to determine the characteristics of flow in presence of thermodiffusion. Using analytical or numerical methods (CFD) the role of thermally induced convection during a thermodiffusion experiment is determined. Most of the investigations are devoted to answer this question of the extent to which the diffusion process is affected by these secondary flows.

In numerical simulations, a model is used to calculate the Soret coefficient. The easiest approach is to consider the Soret coefficient to be a constant value. The value can be obtained from experimental or molecular simulations. For more sophisticated simulations, which might cover larger temperature or concentration variations, theoretical models can be implemented in which the Soret coefficient is calculated based on the flow characteristics.

Since the initiation of diffusion experiments in microgravity environments such as space shuttles and scientific satellites, a large amount of publications have attempted to discuss the effects of microgravity on diffusion experiments. In fact numerical simulations have the potential advantage of being less expensive and often provide the only means to understand g-jitter effects. CFD simulations of diffusion processes under the effect of random vibrations have been the subject of numerous studies. In the following we will address and discuss some of the previous numerical surveys.

Alexander [41] carried out a numerical investigation on the effect of g-jitter on dopant concentration in a modeled crystal-growth reactor. He concluded that low-frequency g-jitter can have a significant effect on dopant concentration.

More than 30 years ago, Gershuni and Zhukhovitskii [42]did a series of studies on the hydrodynamics and stability of fluid flow subjected to an oscillatory gravity field. Their contribution on the development of the averaging method is substantial. The flow was induced in a system with a density gradient. Depending on the case, when the density gradient is due to temperature or concentration variation it is known as thermovibrational and solutovibrational convection, respectively. The averaging method is based on the presentation of flow characteristics (e.g., pressure, velocity, temperature) as a superposition of mean (average) and pulsational parts.

With this method, the average flow could be solved in the system using averaged governing equations, which end up with a steady-state solution for mean flow. This method is only valid only for cases of high-frequency vibrations. The period of the excitations should be less than the viscous (L^2/ν), thermal (L^2/χ), and mass diffusion (L^2/D) times, where L is a characteristic length of the computational domain, ν, χ, and D, are the kinematic viscosity, thermal diffusivity, and mass diffusion coefficients of the mixture, respectively.

Gershuni *et al.* investigated single-liquid and binary mixtures in detail for different geometric configurations. Analytical methods have been employed for linear cases and for non-linear conditions (flow inside a cavity) the numerical solution of the average equations is presented. A detailed review of their work can be found in reference [42]. For cavity flow, they investigated different flow regimes and heat transfer for different vibrational Rayleigh numbers.

Gershuni and co-workers also studied the stability of a mixture layer in presence of the Soret effect [43]. Their study was focused on fluid between two-endless parallel horizontal plates. A constant temperature was applied to the walls. They studied the effects of longitudinal vibration on the onset and instability of thermo-gravitational convection. It was found that the transverse vibration mechanisms cause no instability and have purely a stabilizational role.

Monti and Savino *et al.* [44-47] studied thermophysical experiments in typical microgravity conditions. Using a time-averaged method they investigated the disturbing effects of g-jitter vibrations by considering the quasi-steady residual-g and single frequency oscillations. They have shown that error in the experiments may arise for residual-g on the order of μg as well as for extremely large g-jitter. The optimized alignment of the cell was found by orienting the density gradient in the direction of vibrations at which the error can be minimized.

Monti [48] investigated the suitability of different labs on the ISS for conducting crystallization experiments. They have assumed a cavity (1 by 1 cm) filled with a metal alloy subjected to residual and g-jitter vibrations. They showed that single frequency g-jitter has a greater effect in generating convection motion when orientated orthogonal to the density gradient.

Shu *et al.* [49] used a finite-element method to study double-diffusive convection driven by g-jitter in a microgravity environment. They have considered idealized single-frequency and multi-frequency g-jitter as well as using real g-jitter data taken during an actual space shuttle flight. Their results indicate that the temperature field is undisturbed by convection. The disturbance of the concentration field, however, is pronounced, and the local variation of the concentration follows the velocity oscillation in time. Their numerical study indicates that with an increase in g-jitter force (amplitude), the nonlinear convective effects become more pronounced which in turn drastically changes the concentration fields.

More recently, Savino [50] presented a numerical study of the effect of residual gravity and g-jitter on the thermodiffusion experiments. The results show similar results between the direct integration of the full Navier-Stokes equations (that compute the instantaneous time-dependent flow) and the solutions of the equations for the time-averaged quantities (thermovibrational theory). Moreover, it was concluded that in the range of their experiment the residual gravity and g-jitter generate convective motions when not aligned to the density gradient and stabilizes (or stratifies the flow) when oriented parallel to the density gradient.

Chacha *et al.* [51,52] have considered the thermodiffusion process of methane and butane mixtures by considering residual and single frequency vibrations, by assuming g-jitter to be a single frequency vibration ($f = 0.1, 1, 10\ Hz$) with fixed amplitude. They have investigated the fluctuations in temperature and concentration for different g-jitter frequencies. It was concluded that when g-jitter and residual gravity act in the orthogonal direction to the main density gradient, the induced velocities are larger and the distortion of the isotherms from the purely diffusive regime reaches its maximum. The duration of their simulations were limited to half an hour, which is small compared to diffusion time of their system.

In a brief report, Lyubimova et al. [53] numerically surveyed the effect of forced vibration applied in two directions: normal and tangent to the imposed temperature gradient in the framework of the averaged approach. They have shown that the induced flow in the presence of a low-gravity condition can be damped when the cell is oriented in the appropriate direction.

Sharidan *et al.* [54] presented an analytical method to investigate the heat transfer and mixed convection flow in a vertical parallel-plate channel subjected to g-jitter vibrations. In their method, simplifications were considered including assuming g-jitter to be a single-frequency harmonic vibration. The authors illustrated induced velocity and temperature profiles for different conditions.

Yan and Saghir have performed a series of numerical investigations on the impact of g-jitter on thermodiffusion experiments. In their surveys [55,56], thermal diffusion processes of a binary mixture of water/IPA (90:10 wt%) were studied numerically in a cubic cell in the presence of single-frequency g-jitter ranging from 0.001 Hz to 0.025Hz. These frequencies are in the low-frequency spectrum of the micro-accelerations onboard FOTON satellites. The governing equations were solved using a finite volume method and the variation of density was obtained by using the Boussinesq approximation.

Different scenarios were studied with respect to the amplitude and frequency of g-jitters that may exist alone or simultaneously with static residual gravities. Residual gravities of $10^{-4}g_0$ and 0 were considered, while an amplitude of g-jitter of $10^{-3}g_0$ was chosen, which is one order larger than the residual acceleration. The result of their study suggests that the impact of vibration on diffusion is a combination of the effect caused by each individual g-jitter component. However, the interaction between different g-jitter components, such as the static and oscillatory components, is nonlinear. This adds more complexity to the phenomenon of double diffusion convection. It was also found that the static residual gravity may cause a very strong fluid flow depending on its magnitude. This is especially pronounced at large static residual gravities. Under such conditions, the accuracy of the diffusion measurements will be affected significantly.

While in the presence of oscillatory g-jitter, the flow field is characterized by oscillating convection, which has a frequency identical to the external excitation. The strength of the flow field is enhanced when the static residual gravity exists simultaneously with the oscillatory g-jitter components in the direction perpendicular to the temperature gradient.

The effect of convection of the concentration distribution becomes very dramatic when the g-jitter oscillates in a low frequency whether or not the static residual gravity exists. The temperature field might also be affected by g-jitter vibration for the case of low-frequency g-jitter, as reported in the same study.

In other investigations, Yan *et al.* [57,58] studied the thermal diffusion process of a ternary mixture of methane, n-butane, and dodecane (50:20:30 mol%) under different microgravity environments onboard the ISS and FOTON spacecraft. Their work was intuitive from two points of view: the studied mixture and g-jitter vibration model. A few recent studies were found to focus on the dynamics of a ternary mixture in microgravity. Moreover, the applied g-jitters were in the form of a Fourier series with coefficients derived from actual micro-acceleration measurements during space missions.

The micro-acceleration data was measured by the onboard accelerometers system SAMS (Space Acceleration Measurement System), which measures the vibratory/transient micro-accelerations that occur in the frequency range of 0.01 to 400Hz. The characteristics of these probes will be discussed in the next Chapter. The vibration data was filtered to remove the high frequency content of the signal, and only data with a frequency lower than 2 Hz has been used in their model. Likewise, for simulations for the FOTON environment the measured g-jitter data during mission 12 was used. Different scenarios with respect to the crew being active/inactive have been investigated.

It was found that the diffusion process is negatively affected when subjected to g-jitter. The degree of this effect varies depending on the magnitude of the g-jitters. Local oscillations are observed for all investigated cases in component concentration, velocity, temperature, and diffusion coefficients. The results show that good accuracy in the diffusion experiments onboard ISS is possible, though, the magnitudes of g-jitter vibration should be properly controlled. A threshold value of about 10 μg was suggested by the authors, above which experiments can be negatively impacted by the micro-accelerations. It was also indicated that the magnitude of g-jitter is not the only influential factor on the accuracy of the results of the experiments.

A benchmark numerical solution of thermodiffusion is presented in reference [59], which covers the results of several different teams: the Microgravity Research Center, ULB, Belgium; Ryerson University, Toronto, Canada; and CNRS-Universitésd'Aix-Marseille, France in collaboration with a Russian team from Perm. All the groups solved the governing equations using different methods as listed in the following table.

Table 1-2:Comparison between the numerical methods of different teams[59]

Team	Method of discretization	Highlights of solving technique
Microgravity Research Center ULB	Finite volumes Staggered grid Centered second-order	Projection method for momentum equation Combination of FFT and an implicit ADI for the pressure equation
CNRS-Université d'Aix-Marseille	Finite difference centered second-order	Projection method for momentum equation Successive over-relaxation method for the pressure equation parallel processing algorithm
Microgravity Lab Ryerson University	Finite volumes	SIMPLE algorithm for momentum equation Fully implicit scheme for other governing equations.

The use of an implicit scheme by Saghir's team at Ryerson University had the advantage of using large time steps without incurring stability issues. However, for simulations in the presence of vibration (especially g-jitter), in which very small time step sizes are needed, using implicit methods was not efficient in terms of excessive computational time compared to the explicit schemes.

Simulations were performed by the teams for mixture of water (90%) and isopropanol (10%). A 3-D cubic domain was chosen, which was filled with the mixture and subjected to different gravity fields. The direction of applied gravitational acceleration was perpendicular to the thermal gradient. Various combination of gravity fields were examined in this study. For the cases with a residual gravity field, different values of a static gravity field were simulated. Their results are included in Figure 1-4, in which the separation of species has been normalized in accordance with the ideal condition. This figure demonstrates the negative effect of convection inside the cell on the separation of the species.

The authors have simplified the g-jitter to a single frequency vibration, and, along with various combinations of static and oscillatory components, vibrations with two different frequencies were examined: High frequency (0.2Hz), in which the period is smaller than any characteristic time (viscous, thermal, and diffusion), and lower frequency (f=0.01Hz), in which the period of excitations is comparable with the viscous time.

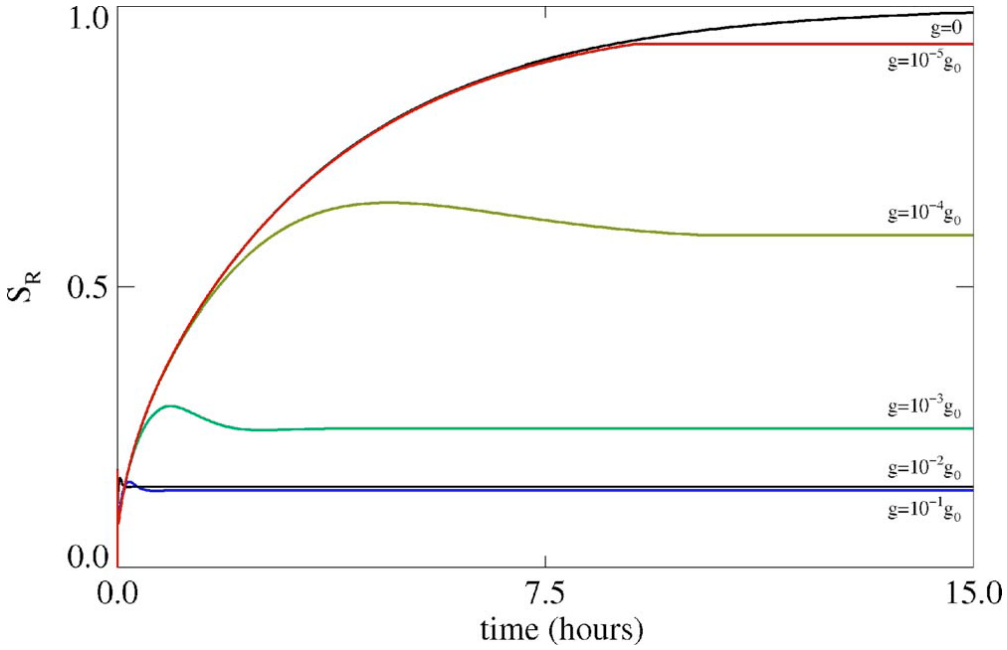

Figure 1-4: Transient Soret separation (Sr)for different gravity levels.[59]

The result of this benchmark study indicates that vibration influences the flow pattern depending on the frequency (low or high). Both heat and mass transport are increased when excitations with lower frequencies are applied. It was observed that in case of pure oscillatory excitations the flow characteristics including velocity, temperature, and concentration periodically oscillate around their values. It was found that the average flow is highly affected by the frequency. For instance, for case of f = 0.2 Hz, extremely weak mean flow was observed. Consequently, the separation process is not affected and follows the weightlessness condition. On the other hand, it was shown that low-frequency vibrations (f = 0.01 Hz) have more impact on the temperature and concentration field for the same amplitude of vibration.

In addition it was concluded that “the periodic oscillations of temperature and concentration had nonsinusoidal shapes displaying a second harmonic twice as large as the forcing fundamental”. When the static field was superimposed with high-frequency g-jitter, buoyancy dominates the process. The authors have mentioned the non-linear interaction between the static and vibrational actions that results in larger deviations in the temperature and concentration fields.

Srinivasan *et al.* [60] performed a CFD investigation on a ternary hydrocarbon mixture of methane, n-butane, and n-dodecane subjected to the micro-acceleration microgravity environment of the FOTON-M3 spacecraft. Due to their methodology for extracting vibrational data from raw measurements, all the applied accelerations were positive in sign. This resulted in formation of a single convection cell in the domain. It was shown that the effect of micro-vibration on FOTON M3 is insignificant. The induced convective flow is not strong enough to dominate the diffusion process due to the small magnitudes of recorded vibrations.

Some of the experimental results of IVIDIL project have been presented by Shevtsova *et al.* in reference [39]. They have briefly reported the results of six experiments which were performed in the natural environment of the ISS (in the presence of random g-jitter vibrations of the ISS). Results were extracted using image processing techniques for water/IPA mixtures with either 90% or 50% mass percentages of water. The results show great reproducibility of the experiments and noticeable agreement with numerical calculations of ideal, zero gravity separations for the 90% water mixture. The time lag between the two similar experiments (Run2 and Run2R) was considerably large and the authors concluded limited contribution of g-jitter vibrations during the normal operating condition of the ISS. The separation profile of Run-2 and Run-2R are shown in Figure 1-5.

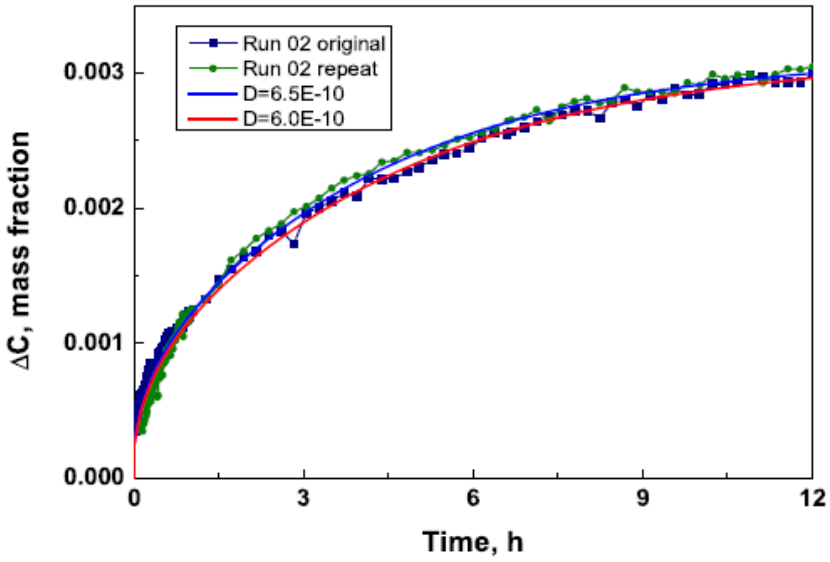

Figure 1-5: Water/isopropanol mixture separation (90% wt) in IVIDIL project[39]

Please not that Run02 corresponds to Run2 in this dissertation. The same results were demonstrated for the 50%-50% mixture. However, for the sample run of "1N", considerable deviation from the ideal state was reported that, according to the authors, was due to non-nominal g-jitter vibration during some special activities such as orbit correction, docking, or undocking.

More recently, Ahadi and Saghir [61] performed a numerical study on the effect of g-jitter vibrations on thermodiffusion experiments for two space platforms: ISS and FOTON. They have studied water/IPA mixtures (50%wt or 90%wt water). The actual acceleration data (measured onboard the platforms) were used. However, on board the ISS, instead of using Fourier series for different frequencies, they considered the Root Mean Square (RMS) value of the recorded acceleration within time intervals equal to the simulations' time step. On board FOTON, the time interval between the raw data was 30s and they used spline interpolation to provide acceleration data for CFD analysis. Prediction of the density was conducted using PC-SAFT equation of state which has been widely used to study the associating mixtures.

The results show relatively significant effect of g-jitter vibrations on the thermodiffusion. The mixing effect is considerable when the RMS values of g-jitter were applied.

For the case of FOTON, it was concluded that the environment is more suitable for performing such experiments where 75% of the separation of the ideal condition was achieved. Ahadi et al. [61] also investigated the role of cavity size and suggested that choosing a smaller length for the cavity (0.5 cm) can result in weaker convection inside the cell.

1.3.3.1 Summary of the numerical investigation

As cited earlier, numerous studies have been devoted to identify the role of g-jitter vibrations on quality of the thermodiffusion experiments in various microgravity environments. Different scientists have considered different models for applying the g-jitter vibrations in computer models. Roughly, these methods can be categorized to single frequency models, multi-frequencies models (using Fourier series), and using raw acceleration data. These different approaches are included in Table 1-3.

The common agreement among the studies was that, when applied individually, the effects of high frequency vibrations on the thermodiffusion experiments are negligible. However, in the case of g-jitter vibration, since the summation of a range of frequencies is of interest, one cannot readily neglect the effect of high frequency vibrations due to the non-linear nature of the system.

Table 1-3: Different approaches in Modeling of g-jitter random vibrations.

g-jitter modeling method	Researchers
Single Frequency	(Shu et al. 2001) [49] (Chacha et al. 2002) [51] (Lyubimova et al. 2005) [53] (Sharidan et al. 2005) [54] (Yan et al. 2005 -2008) [55,56]
Multi Frequency (Fourier Series)	(Monti and Savino 2001) [48] (Shu et al. 2001) [18] (Yan et al. 2007) [58] (Yan et al. 2007) [57]
Actual raw measured data	(Shu et al. 2001) [49] (Ahadi and Saghir 2012) [61]

In general, the attention of cited studies was on the effect of g-jitter vibrations on the

fluid flow and concentration distribution during a thermodiffusion experiment. The important properties of g-jitter vibration can be characterized in their magnitude, frequency, and orientation. The following table summarizes the findings of cited studies.

Table 1-4: Summery of finding of cited references based on influential factors

Influential Factors	Findings	Researchers
Magnitude	The threshold magnitude for the g-jitter acceleration ~ 10μg	(Yan et al. 2008) [56]
	The increase of g-jitter magnitude strengthens the nonlinear convective effects	(Shu et al. 2001) [49]
	Increasing the g-jitter magnitude enhances the mixing of the fluid and therefore reduces species separation	(Chacha et al. 2002) [51]
Frequency	The effect of g-jitter on diffusion increase with the decrease of frequency and the increase of magnitude. The nonlinear convective effects are very significant when the g-jitter have low frequency but high amplitude	(Yan et al. 2005) [55] (Yan et al. 2008) [56] (Lyubimova et al. 2005) [53] (Sharidan et al. 2005) [54]
Orientation	The experimental cell should be oriented in such a way that the g-jitters are parallel to the density gradient (temperature gradient)	(Alexander 1990) [41] (Monti and Savino 2001) [48] (Chacha et al. 2002) [51]

1.3.3.2 Equation of State

Equilibrium thermodynamics properties are widely used in thermodiffusion models to calculate the thermal diffusion coefficients. Therefore, it is a prerequisite to know reliable thermodynamic properties for the theoretical research on thermal diffusion. Otherwise, an accurate prediction of thermodiffusion will never be attained even if a perfect model is available. However, the thermodynamic properties are difficult to obtain fully from the literature, and some of the properties are also very difficult to measure accurately.

One reasonable approach to obtain the required thermodynamic properties is to use an Equation of State (EOS). Details about Equations of State can be found in literature, including reference [62].

Two “Equations of State” have been widely used for thermodiffusion processes owing to their advantages for hydrocarbon mixtures or associating mixtures. The first is the Peng-Robinson Equation of State (PR-EOS) [63], which is widely used for hydrocarbon mixtures due to its simplicity and accuracy. The other Equation of State is Perturbed Chain Statistical Association Fluid Theory (PC-SAFT). The essence of the SAFT EOS is to sum various contributions from hard sphere, hard chain, dispersion, and association mixtures. This approach calculates the association term by thermodynamic perturbation theory (TPT) using a reference fluid. The SAFT Equation of State has been shown to offer a great improvement in predicting the properties of associating and chain-molecule fluids [64]. The PC-SAFT EOS has shown a sound predictive capability for associating systems as well. As such, it has become popular in industry and the research community recently.

In terms of computation fluid dynamics for simulating thermodiffusion processes, the most important thermodynamic property is the density of the mixture. The density variation in a thermodiffusion cell is the result of temperature and concentration variation. The effect of pressure on the density can be neglected due to insignificant variation of pressure. In the presence of gravity, density variation induces convection in the cavity. This means in the case of higher density difference in the domain, the induced convective flow becomes stronger. Thus, proper prediction of density is essential when the interaction of buoyancy-induced flow and diffusion mass fluxes is of interest. The effects of the gravity field on thermodiffusion might be over or underestimated as a consequence of employing inaccurate equations of state.

This issue is investigated by Parsa *et al.* [65]. They have considered two methods for prediction of the density in the binary mixture of water/isopropanol (90/10 wt.%). These methods were using the mixing law and using the PC-SAFT EOS. They have shown that the variation in density is larger for case of PC-SAFT EOS. Mixing law provides a mole-weighted average density by considering the mole fraction of components in each grid point.

Yet, the authors have not considered the effect of temperature on density variation when using the mixing law. Consequently, variation of density between the heated walls was fairly small. The authors claimed that better results were achieved when employing the PC-SAFT equation of state. They also compared the results with the Boussinesq approximation. The maximum changes in the density for the case of PC-SAFT EOS and Boussinesq were about 11 and 5 kg/m^3, respectively. This shows that when using PC-SAFT EOS, stronger convective motion is expected. The validity of such a numerical approach through experiment is needed.

The methods for prediction of density among cited references are included in Table 1-5. As shown, a great number of studies have used the Boussinesq method for simulation of fluid flow for thermodiffusion applications. Moreover, in all of those studies other properties of the mixture were assumed to be constant including viscosity, specific heat, and thermal conductivity. In this study, we have also used the Boussinesq method for calculation of the buoyancy force while keeping other mixture properties constant, as will be discussed in Chapter 3.

Table 1-5: List of the used models for prediction of density variation

Density model	Researchers
Boussinesq	(Monti and Savino 2001) [48] (Lyubimova et al. 2005) [53] (Sharidan et al. 2005) [54] (Yan et al. 2005) [55] (Yan et al. 2008) [56] (Shevtsova et al. 2010) [66]
Ping Robinson EOS	(Chacha, et al. 2002) [51] (Yan et al. 2007) [57] (Yan et al. 2007) [58]
PC SAFT EOS	(Ahadi et al. 2012) [61] (Parsa et al. 2012) [65]

1.4 Objectives and Scopes

The main objective of this study is to survey the effects of different gravity fields on a typical thermodiffusion experiment. This study will be discussing three different gravity fields including residual (static), pure oscillatory (forced vibration) and random g-jitter vibrations in the International Space Station (ISS) environment.

For this aim, a complete CFD code has been developed by the author which is used to perform unsteady fluid flow simulations in presence of the above-mentioned gravity fields. The main goals of this study are as follows:

1- To investigate the optimized case for orientation of the cell with respect to the direction of the applied gravity to obtain the most stable flow regime.

2- To investigate the Soret effect in the presence of static gravity fields and to find proper criteria to avoid convection.

3- To survey the effects of pure-oscillatory gravity fields on thermodiffusion experiments and to find the role of frequency and magnitude of gravitational acceleration. Also, to propose proper criteria to discuss composition variation.

4- To simulate the experimental runs of the IVIDIL project in order to visualize the flow fields and discuss the findings of this project.

5- To investigate the negative effects of g-jitter vibrations onboard the International Space Station in a typical experiment (IVIDIL-Run2). This includes evaluation of the applicability of different methods for implementing acceleration raw data and considering the effects low-frequency contribution of g-jitter as well as prevailing quasi-steady state acceleration on the experiments conducted onboard ISS.

The results of this study convey valuable information about the conditions of a microgravity environment as a base for future experimental studies.

Chapter 2 International Space Station Acceleration Measurement

The most accurate method for simulation of a microgravity environment is indeed using the acceleration data that are recorded onboard the space facilities. Any space platform including the International Space Station (ISS) and even small scientific satellites are equipped with hi-resolution vibration measurement systems. The acceleration data are very important from different aspects in order to survey the characteristics of the microgravity environment. There is always demand for acceleration measurements, and for the case of ISS, the complex is well-equipped with necessary probes. In this chapter we will briefly discuss the acceleration measurement systems onboard the ISS. Furthermore, different methodologies for extracting the data for CFD analysis are described.

2.1Acceleration measurement system

The acceleration measurements from the ISS are sponsored by NASA Glenn Research Center (GRC) Principal Investigator Microgravity Services (PIMS). The responsibility of PIMS is to process and archive the acceleration measurements. PIMS also provides technical analysis of the measurements for a variety of platforms including the space shuttle, parabolic flights, sounding rockets, drop towers, and of course the International Space Station [67]. PIMS supports ISS for various scientific disciplines such as biotechnology, combustion, fluid physics, material science, and fundamental physics. The acceleration measurements of ISS are performed by two systems known as the Microgravity Acceleration Measurement System (MAMS) and the Space Acceleration Microgravity System (SAMS). These systems were launched on April 2001 and installed on the ISS. The main objective of these systems is to verify the vehicle microgravity environment. Brief information about these systems is provided in the following sections.

2.1.1 MAMS[3]

The main task of the MAMS unit is to assist science experiments requiring quasi-steady acceleration data measurements. The MAMS system includes two different acceleration measurement systems known as MAMS Orbital Acceleration Research Experiment Sensor Subsystem (MAMS-OSS) and MAMS High Resolution Accelerometer Package (MAMS-HiRAP), each with a distinct measurement objective.

MAMS-OSS records the quasi-steady accelerations, known as the residual gravitational acceleration, with a cut-off frequency of 1 Hz (maximum). The data recorded in MAMS are constantly transmitted to ground-based facilities at a rate of between 20 and 200kbps. Only about 24 hours of MAMS data can be stored onboard. The raw data of MAMS needs additional data processing for bias compensation. However, the MAMS-OSS data provided on the PIMS webpage [68] have been filtered and bias compensated and are ready for use with a time interval of 16 seconds.

The MAMS HiRAP is used to characterize the ISS vibratory environment up to 100 Hz. The sampling rate is 1000 samples per second and low pass filtered with a cut-off frequency of 100 Hz. The purpose of the MAMS HiRAP is to measure the vibratory and transient accelerations on the ISS. The data of MAMS HiRAP cannot be stored onboard and are sent to earth instantly. The data of HiRAP is also available on the PIMS webpage [68]. The data also need to be demeaned for bias compensation before use.

In this study (section 4.6.1Quasi-steady (residual) acceleration) the data of MAMS-OSS are used to evaluate the quasi-steady residual acceleration onboard ISS in the time of the IVIDIL-Run2 experiment. For vibratory data, the data of SAMS is used (section 4.6.2

[3]Microgravity Acceleration Measurement System

Vibratory full-range g-jitter.)

2.1.2 SAMS[4]

SAMS measures vibratory acceleration data in the range of 0.01 to 300 Hz. SAMS-II is a multi-probe system scattered throughout the ISS. Currently there are 7 probes installed in the station. SAMS is currently measuring the acceleration environment in all three ISS laboratories: the USLAB, Columbus Orbital Facility (COF), and the Japanese Experiment Module (JEM).One of the SAMS-II sensors (SAMS-ES08) is located in the MSG facility where the IVIDIL experimental apparatus was installed. The data are collected with a sample rate of 500 data per second. The raw data are available on the PIMS website [68]. The raw data needs be demeaned for bias compensation before use.

2.1.2.1 Low frequency contribution

As described above, SAMS records the oscillatory g-jitter accelerations in the range of 0.01 to 300Hz with a high-resolution sampling rate. However, we are interested in extracting the low-frequency contribution of the accelerations. As discussed in Chapter 1, the effects of high-frequency vibrations are limited. In other words, it is probable that the thermodiffusion system does not react to the high-frequency contribution of g-jitter. Thus, to extract low-frequency contribution of g-jitter, it is possible to provide PSD[5] diagrams of the raw data for successive time intervals. When the PSD values are plotted for different times, a spectrogram results which is a road map of how acceleration signals vary with respect to both time and frequency. Generally, the PSD is calculated using Fast Fourier Transform (FFT) for an interval of 1 second using 500 data points. In order to get the low frequency contribution of g-jitter one should integrate the PSD for the required range (for instance 0-10Hz). PSD diagram of IVIDIL-run2 is illustrated in Figure 2-1, which demonstrates the contribution of the 0-10Hz frequencies.

It should be noted that the results that are obtained from PSD analysis are in units of g^2/Hz. Thus the acceleration data generated with this method are all positive in sign.

---

[4]Space Acceleration Microgravity System

[5]power spectral density

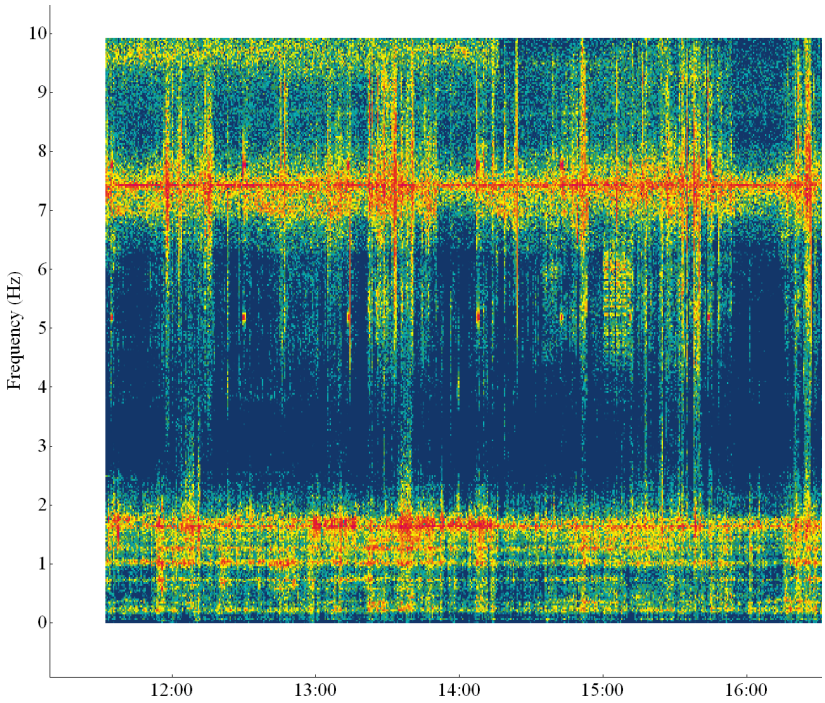

Figure 2-1: PSD diagram of (0-10Hz) for the first 5 hours of IVIDIL-run2 [Color]

2.2 Extracting acceleration data for the CFD code

For a CFD analysis an acceleration vector is needed for each time-step to be implemented in the momentum equation. In this study, three different acceleration sources are considered, according to Table 2-1. As shown for the case of the low-frequency contribution and quasi-steady acceleration, the time intervals between the raw data are larger than the CFD code time-step (0.01s). Thus for these cases no special treatment is needed.

Table 2-1: ISS vibratory data used in the simulations

Acceleration	Full frequency range [0-300 Hz]	Low-frequency range [0 – 10Hz]	Quasi steady
Regime	Vibratory (g-jitter)	Vibratory (g-jitter)	residual
Sensor	SAMS-ES08	SAMS-ES08	MAMS-OSS
Raw data Time interval [s]	0.002	1	16

However, for the case of the full frequency range g-jitter, the time-step in the CFD code is 5 times larger than the sampling rate. Thus an appropriate method is required to change the raw data to the values that can be used in the CFD code for any arbitrary time step.

It is noteworthy to mention that the time-step of the CFD code should not be smaller than the acceleration data interval. The reason is that the process is governed by the overall regime of the g-jitter and sudden (temporary) pulses have no permanent effect on the system. The experiment takes about 12 hours as the separation progresses slowly. As a result, even if some acceleration data are neglected by choosing larger time-steps, the final result of this long-term experiment will not be affected.

Nevertheless, as will be discussed in the next Chapter, a time-step of 0.01s was chosen for simulations. Thus to be more specific, one single data point should be extracted for each 0.01s (CFD code) from 5 raw acceleration data points (time interval of 0.002s). However, for this purpose, a proper methodology needs to be implemented.

There are two important concerns regarding this issue. First of all, the nature of the raw data should be maintained. For the case of g-jitter (high-frequency vibrations), the sign of the acceleration changes from positive to negative (or vice versa) rapidly. Secondly, it is preferred to use all of the available raw data. In the following section four methods for achieving this are presented and discussed.

2.2.1 Interval Average (AVE)

One simple method is to get the average value of the acceleration data within the chosen timestep. The interval average plots are used for acceleration analysis to show net accelerations which last for a number of seconds equal to or greater than the interval parameter used. Short duration, high amplitude accelerations can also be detected with this type of plot, however, the exact timing and magnitude of specific acceleration events cannot be extracted.

This method successfully models the sign change of accelerations. However, the average method results in smaller values (comparing to other methods) for acceleration. This is due to the fact that the raw data are already demeaned for bias compensation. In order to illustrate this fact, a sample of normalized raw data is plotted in Figure 2-2. The time interval of the raw data is 0.002 s and we extracted one value for each 0.01 s. In the same figure the calculated values using the average method are plotted.

2.2.2 Interval Root-Mean-Square (RMS)

Another method is to get the Root-Mean-Square (RMS) of data within the arbitrary timestep. For our case, we evaluated the RMS value of 5 data points. The RMS was calculated according to the following equation in which X is the demeaned acceleration data:

$$\mathrm{X_{RMS}} = \left(\frac{1}{\mathrm{n}} \sum_{i=1}^{n} X_i^2 \right)^{\frac{1}{2}} \tag{2-1}$$

RMS plots are frequently used to show oscillatory content in the acceleration data. For the considered period of time, this quantity gives a measure of the variance of the acceleration signal. This data representation is useful for identifying gross changes in acceleration levels usually caused by the initiation or cessation of activities such as crew exercise or equipment operations [69].

Although this method has been widely used for statistical approaches, its applicability to preparing data for CFD code is not well accepted. The reason is that the output of an RMS analysis is always positive in sign, which is a major modification in the nature of the problem. In Figure 2-2, the interval RMS method for the sample raw data is also shown.

2.2.3 Interval Maximum/Minimum (Max/Min)

Another method is to consider the maximum or minimum amount of the raw data within a certain timestep. In this method it is assumed that the cell is subjected to the highest acceleration (in magnitude) that has been measured by the probes within the timestep. Obviously, the results of this method have the largest possible amplitude. This method supports both negative and positive signs for acceleration data. Implementation of this method leads to the simulation of the worst-case scenario for g-jitter vibrations. Results from this method are plotted in Figure 2-3 for the same sample acceleration data of Figure 2-2.

2.2.4 Interval Root-Mean-Square with Interval average sign (RMS-AVE)

The significance of interval Root-Mean-Square method is that all data points contribute to the final outcome. Thus, no single data point is missed. However, the output data in this method is always positive that is a substantial deficiency of that method.

One remedy for this deficiency is to calculate the RMS values within each time step but consider it with the sign of the average value in the same period. The sign of average value within the timestep indicates that most of the vibrations are positive or negative. This method has not been used previously. However, it might provide the best solution for the CFD analysis. With this method, not only are all of the raw data considered, but so is the vibratory nature of the recorded accelerations. For ease of citation this method will be addressed as RMS-AVE.

The summary of this discussion is included in Table 2-2, which shows a comparison between the different methods in the calculation of acceleration data for the CFD code.

Table 2-2: Methods for calculation of CFD acceleration data

Method	*Deficiency*
Interval average (AVE)	Relatively smaller outcome
Interval Root Mean Square (RMS)	No sign-change in the acceleration data
Interval Maximum/Minimum (Max/Min)	Presenting the worst scenario
Interval Root-Mean-Square with interval average sign (RMS-AVE)	Not used in the literature

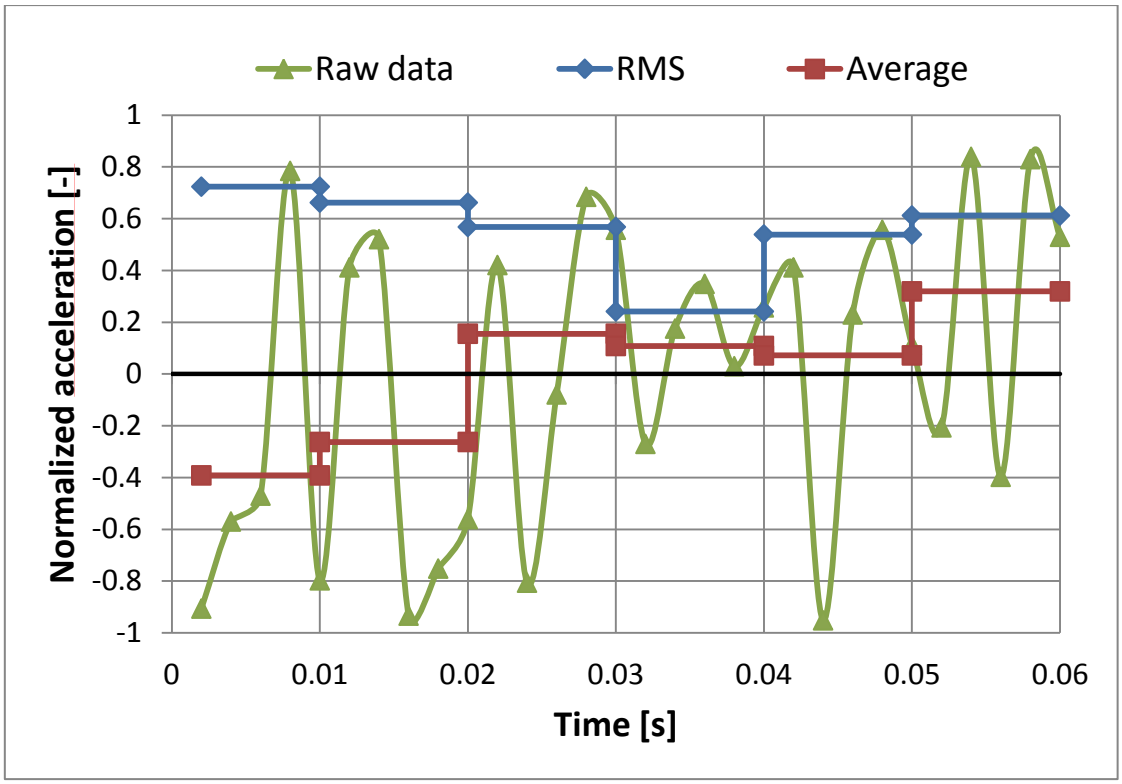

Figure 2-2: Interval Average and RMS methods for a sample normalized raw data

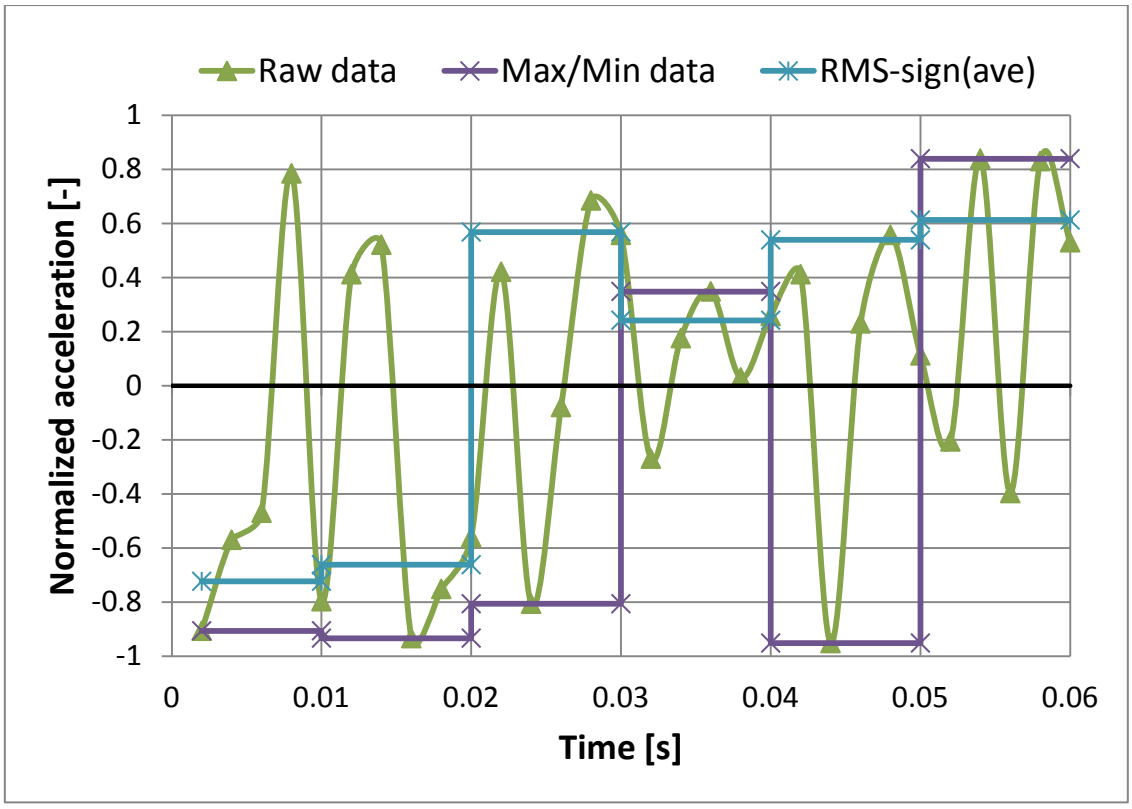

Figure 2-3: Interval Max/Min and RMS-Ave for a sample normalized raw data

2.3 Acceleration data preparation

Based on the discussion presented above, the acceleration raw data have been downloaded from the PIMS website [68] for the period of IVIIDL-run2. It should be noted that all the vibrational raw data of PIMS are normalized with respect to the gravitation of the earth and are in g_0 units.

The residual raw (MAMS-OSS) data are ready to be used without any special treatment. The g-jitter vibration data are provided from SAMS-ES08 sensor for the 18 hours of IVIDIL-Run2. The raw data files are in 4 column binary format for a duration of 10 minutes. A Matlab® code has been developed for data processing of the raw data. The procedure of generating CFD input files are as follows. The binary data are imported and demeaned in the duration of 10 minutes. Then the calculation of raw data proceeds according to the interval methods explained earlier. The output is written in ASCII format that can be used by the CFD code. The Matlab® codes for reading and processing the raw data are included in Appendix A. The input acceleration data files (for CFD code) are provided for up to 14 hours (more than 5 million time steps).

The low-frequency contribution of g-jitter acceleration data has been provided by our contributors in the Canadian Space Agency (CSA). For the case after the calculation of PSD, the contribution of 0-10 Hz is calculated by integrating through the mentioned frequency range.

Chapter 3 Governing Equations and Numerical Method

The main goal of this dissertation is to survey the effects of different gravity fields on a typical thermodiffusion experiment. In this chapter the problem is tackled in terms of computational domain and governing equations. Furthermore, information is provided for the numerical technique including methodologies for solving governing equations, independence of the solution, and testing the accuracy of the code.

3.1Problem specification

The computational domain of this study consists of a square cavity filled with the mixture (water/isopropanol 90%/10% wt.%) that is subjected to a certain temperature difference. This geometry was adopted from the IVIDIL project, in which the size of the cavity was 1 by 1 cm. The temperatures of the upper and lower walls are maintained at constant values with a set difference from the reference temperature. The reference temperature was set to be 25°C. Thus, for example, for a temperature difference of 10 °C, the temperature of the upper and lower wall was fixed at 30 °C and 20 °C, respectively. The reason for such temperature control was to eliminate the excess pressure due to changes in the total volume of the mixture. The schematic of the computational domain is illustrated in Figure 3-1. As shown, the side walls were considered to be ideally adiabatic. The applied boundary conditions will be discussed in more detail in 3.3.3.

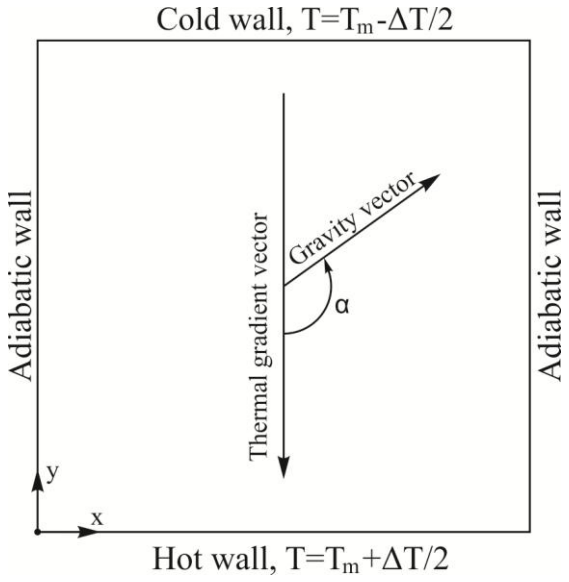

Figure 3-1: Schematic of computational domain

The effects of gravity were also considered. The gravitational vector can change its direction and magnitude throughout the simulations. Thus, the gravitational acceleration was split into its components along the coordinate parameters (x,y). The angle between the gravitational vector and applied temperature gradient is α. For instance, in the case of heating from below, these two vectors are in the same direction (α = 0).

3.2 Governing equations

The numerical solutions for fluid flow, heat transfer, and other related processes such as mass transfer can be performed when these processes have been expressed in terms of mathematical governing laws generally in the form of differential equations. The detailed derivation of these equations is outside of the scope of this work, but the reader is referred to standard textbooks for further reading [70,71]. The governing equations of the current study that have been included are the conservation of mass, momentum, energy, and chemical species which will be discussed in the following sections.

3.2.1 Conservation of mass

The conservation of mass law applied to a fluid passing through an infinitesimal fixed control volume yields the following equation in the Lagrangian approach:

$$\frac{\partial \rho}{\partial t} + \frac{\partial (\rho u)}{\partial x} + \frac{\partial (\rho v)}{\partial y} = 0 \tag{3-1}$$

in which ρ is the density of the mixture and u and v are the velocity vector components.

In this study, since the working fluid is a liquid mixture, assuming an incompressible condition is valid. Thus, the density of the fluid within each control volume is assumed to be constant. Consequently the velocity field becomes divergence free and the continuity equation becomes:

$$\nabla . \vec{V} = \frac{\partial u}{\partial x} + \frac{\partial v}{\partial y} = 0 \tag{3-2}$$

3.2.2 Conservation of momentum

The differential equation governing the conservation of momentum in a given direction for a Newtonian fluid can be written along similar lines as the conservation of mass equation. However, it is more complicated because both shear and normal stresses must be considered. The momentum equation in tensor notation can be written as [70]:

$$\frac{\partial(\rho u_j)}{\partial t} + \mathrm{u_k}\frac{\partial(\rho u_j)}{\partial x_k} = -\frac{\partial P}{\partial x_j} + \frac{\partial}{\partial x_j}\left[\mu\left(\frac{\partial u_i}{\partial x_j} + \frac{\partial u_j}{\partial x_i}\right)\right] + \rho F \tag{3-3}$$

in which P is the pressure, μ is the kinematic viscosity, and F is the body force. By assuming incompressible flow, the momentum equations can be written for each direction as [72]:

$$\frac{\partial u}{\partial t} + \mathrm{u}\frac{\partial u}{\partial x} + v\frac{\partial u}{\partial y} = -\frac{1}{\rho}\frac{\partial P}{\partial x} + \nu\left(\frac{\partial^2 u}{\partial x^2} + \frac{\partial^2 u}{\partial y^2}\right) + F_x \tag{3-4}$$

$$\frac{\partial v}{\partial t} + \mathrm{u}\frac{\partial v}{\partial x} + v\frac{\partial v}{\partial y} = -\frac{1}{\rho}\frac{\partial P}{\partial v} + \nu\left(\frac{\partial^2 v}{\partial x^2} + \frac{\partial^2 v}{\partial y^2}\right) + F_y \tag{3-5}$$

or in vector notations:

$$\frac{\mathrm{D}\vec{V}}{Dt} = -\frac{1}{\rho}\nabla p + \nu\nabla^2\vec{V} + \vec{F} \tag{3-6}$$

where the operator$\frac{D}{Dt}$ is the material derivative and is defined as:

$$\frac{D}{Dt} = \frac{\partial}{\partial t} + u\frac{\partial}{\partial x} + v\frac{\partial}{\partial y} \tag{3-7}$$

3.2.3 Conservation of energy

The principle of conservation energy amounts to an application of the first law of thermodynamics to a fluid element as it flows. For a steady, low-velocity flow with negligible viscous dissipation and no energy source, the energy equation can be written as [73]:

$$\nabla.(\rho u T) = \nabla.(\frac{k}{c_p}\nabla T) \tag{3-8}$$

in which T is the temperature of the mixture and k and c_p are the thermal conductivity and the constant-pressure specific heat capacity, respectively. For an incompressible flow, Eq(3-8) becomes:

$$\frac{DT}{Dt} = \frac{k}{\rho c_p} \nabla^2 T \tag{3-9}$$

3.2.4 Conservation of chemical species

The mass fraction c_i of a chemical species "i" in the mixture is described by the mass of species i (contained in a given volume) to the total mass of the mixture (contained in the same volume). Thus, by having c_i as the mass fraction of a chemical species in the presence of velocity field and non-reacting mixture, the conservation of c_i is expressed as [73]:

$$\frac{\partial}{\partial t}(\rho c_i) + \nabla \cdot \left(\rho u c_i + \vec{J}_i\right) = 0 \tag{3-10}$$

Here the first term denotes the change of rate of the chemical species as mass per unit volume. The second term is the divergence of two fluxes: convection and diffusion. The convection flux is the flux that is caused by the flow field.

The diffusion flux J_i is normally caused by the gradient of the mass fraction of a species when the composition of a mixture is non-uniform. This is the principle of Fick's law in which the diffusion flux is defined as:

$$\vec{J_1} = -\rho D_{ic} \nabla c_i \tag{3-11}$$

where D_{ic} is the molecular diffusion coefficient of the species i in the mixture. However, mass diffusion can occur by factors other than concentration differences, although the concentration differences are of primary importance. When thermal diffusion or the Soret effect comes into the picture, a temperature gradient is also responsible for mass diffusion. The diffusional mass flux as a result of both temperature and concentration gradients in a binary fluid mixture can be expressed as [6]:

$$\vec{J_1} = -\rho(D_c \nabla c + c_0(1 - c_0) D_T \nabla T) \tag{3-12}$$

where D_c and D_T are the molecular diffusion and thermal diffusion coefficients of the mixture, respectively, and c_0 is the initial mass fraction of the carrier species. Since in this study we are dealing with a binary mixture, the conservation of chemical species is solved for only one of the species. We used the carrier component, i.e. water. Using Eq(3-12) and Eq(3-7), the conservation of chemical species equation becomes:

$$\frac{\mathrm{Dc}}{\mathrm{Dt}} = D_c \nabla^2 c + c_0(1 - c_0) D_T \nabla^2 T \quad (3\text{-}13)$$

It is also conventional to use the Soret coefficient instead of thermal diffusion coefficient. The Soret coefficient is defined as the ratio between D_T and D_c;

$$\mathrm{S_T} = \frac{D_T}{D_c} \quad (3\text{-}14)$$

Thus, Eq(3-13) can be rearranged to the following form:

$$\frac{\mathrm{Dc}}{\mathrm{Dt}} = D_c(\nabla^2 c + c_0(1 - c_0) S_T \nabla^2 T) \quad (3\text{-}15)$$

3.2.5 Buoyancy force

In general, a buoyancy driven flow is characterized by a fluid whose density is dependent on temperature, on the concentration of chemical species, and on the static pressure. Thus, the density can be written as a function of temperature, concentration, and pressure:

$$\rho = \rho(\mathrm{T}, \mathrm{m}, \mathrm{P}) \quad (3\text{-}16)$$

When such a fluid is subjected to a gravitational field of strength g, fluid motion is induced as a result of non-uniform distribution of hydrostatic pressure (gradient) in the environment. The various locations in the region have different densities compared to the reference density (ρ_r). Therefore, the difference in the pressure gradient drives the motion by the buoyancy force *B*. Its magnitude is calculated as [72];

$$\mathrm{B} = \mathrm{g}(\rho_\mathrm{r} - \rho) \quad (3\text{-}17)$$

This force is applied as a body force in the Navier-Stokes equation. As seen, to predict the magnitude of the buoyancy force a model is needed for calculation of the density. In the scope of the current study, variation of static pressure is rather limited and since the fluid is assumed incompressible, the effect of pressure on the density is neglected. Thus, the density is only a function of temperature and concentration. The density is a thermodynamic property and should be predicted according to experimental or theoretical models which are known as the “equations of state” (EOS).

One of the most convenient models for the prediction of density is the Boussinesq approximation [72]. In which the variation of density is related to the changes of one property (such as temperature or concentration) by the proper expansion factor. In the current study, the density of the mixture is calculated using this method according to the following equation:

$$\rho = \rho(T, c) = \rho_0[1 - \beta_T(T - T_0) + \beta_c(c - c_0)] \quad (3\text{-}18)$$

in which β_T and β_c are the thermal expansion coefficient and volumetric concentration expansion coefficient, respectively, and T_0 and c_0 are the initial (reference) temperature and concentration of the mixture, respectively. The credibility of the Boussinesq approximation has been proven in many studies.

However, since this method considers only a linear variation in density (with respect to the temperature or concentration), the application is limited to the cases with a small variation of temperature and concentration. This method has been widely used in the simulation of thermodiffusion [53-56,66]. A relatively recent benchmark numerical study confirms the applicability of the Boussinesq approximation for thermodiffusion simulations [59]. When the Boussinesq approximation is applied, the body force in Eq(3-4)and Eq(3-5) becomes:

$$\vec{F} = \vec{g}\,[-\beta_T(T - T_0) + \beta_c(c - c_0)] \quad (3\text{-}19)$$

Besides the Boussinesq approximation, there are other equations of state that have been employed by different researchers. The Peng-Robinson EOS [63] has been widely used for natural gas systems in the petroleum industry. This model has the ability to provide reasonable accuracy near the critical point, particularly for calculations of the compressibility factor and liquid density. This model has shown accurate predictions for non-associating mixtures such as hydrocarbons, which have been employed in some thermodiffusion studies [51,57,58].

3.3 Numerical method

A numerical code has been developed by the author to solve the governing equations cited in above (Eq(3-2), Eq(3-6), Eq(3-9)Eq(3-15)). In the following sections the methodology and procedure of the numerical method is described.

3.3.1 Grid type

One of the major difficulties in solving first order derivatives (such as pressure terms in the momentum equation or the continuity equation) is the appearance of wavy velocity or pressure fields which are also known as checkerboard fields. This difficulty rises when a single grid is used for discretization of the equation, in which the difference of a property for cell is computed based on the difference between two alternate grid points and not between adjacent ones. A sample demonstration of such a problem is shown in Figure 3-2. There is no guarantee that such checkerboard fields will be avoided during the calculations.

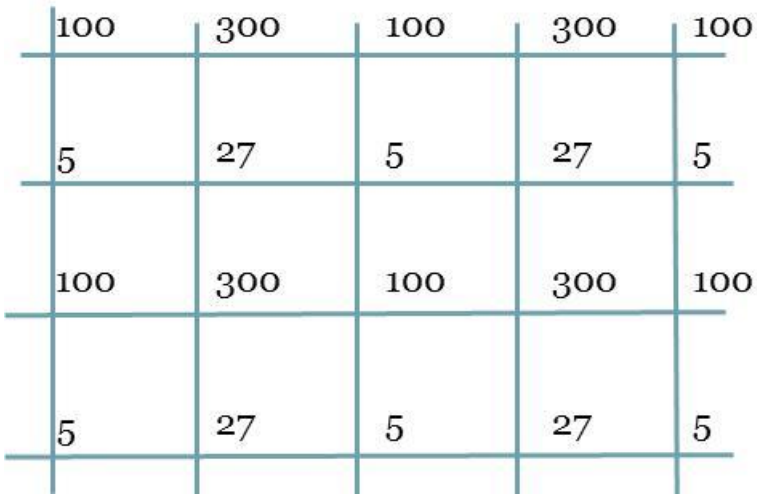

Figure 3-2: Sample checkerboard (pressure or velocity) field[73]

In the case of a pressure checkerboard field, zero pressure force is applied on the momentum equation because the pressure gradient for each grid point is calculated based on the difference between the neighbour grid values, which are zero. In case of a velocity checkerboard (wavy) field, the continuity equation is satisfied based on the same discretization.

This difficulty can be minimized by over-specification of the boundary conditions or under-relaxation with respect to a smooth initial guess. However, there is a secure remedy for such difficulty which to use a staggered grid.

In a staggered grid, each dependent variable is obtained on its own grid. By arranging the velocity components on grids that are different from the grid used for other variables (pressure, temperature, etc.), the difficulty described above is eliminated. Therefore, only a reasonable velocity field will result from this approach. Such a displaced or staggered grid for the velocity components was first used by Harlow and Welch [75]. A sample configuration of a staggered grid is shown in Figure 3-3.

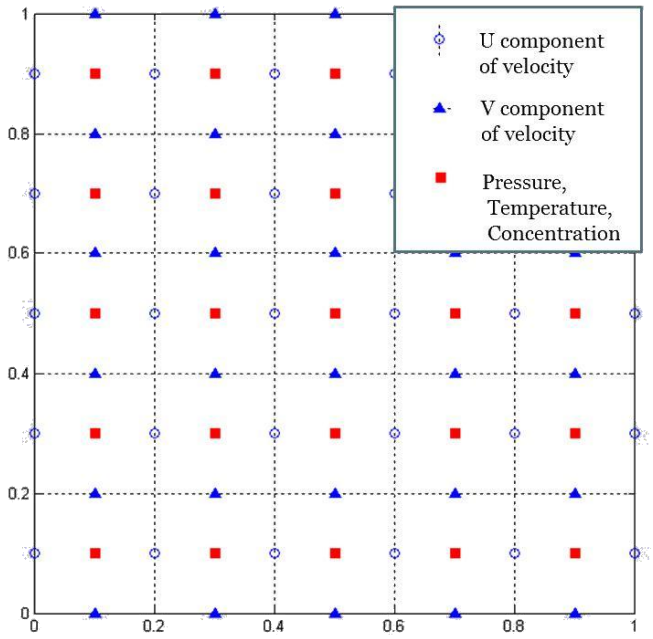

Figure 3-3: A sample configuration of implemented staggered grid

As demonstrated in Figure 3-3, the pressure grid points are placed in the centre of the control volume and the velocities are obtained on the faces. It is also shown that the velocity components are positioned on the boundary conditions. There is no pressure grid point on the boundaries.

3.3.2 Projection method

The difficulty in solving Navier-Stokes equations is that these equations are non-linear and also the velocity field is coupled with the pressure field. The first problem of non-linearity can be diminished by using iterative methods. However, the real difficulty is that the calculation of the velocity field lies in an unknown pressure field. Fortunately, there are numerous numerical techniques to overcome this difficulty. Use of vorticity-based methods [76] is an alternative option to eliminate pressure from the governing equation. There are also other pressure and velocity correction methods such as SIMPLE or SIMPLER [73].

In this study, the Navier-Stokes equations are solved using an explicit method known as projection method. In this multi-step method, an auxiliary velocity v* is obtained by neglecting the pressure gradient in the momentum equations:

$$\frac{\vec{V}^* - \vec{V}^n}{\Delta t} + \left((\vec{V}.\nabla).\vec{V}\right)^n = \nu(\nabla^2 V)^n \tag{3-20}$$

In the next step the provisional velocity field is corrected by considering the pressure terms as shown in below:

$$\frac{\vec{V}^{n+1} - \vec{V}^*}{\Delta t} + \frac{\nabla p^{n+1}}{\rho} = 0 \tag{3-21}$$

The continuity equation can be written as:

$$\nabla.\vec{V}^{n+1} = 0 \tag{3-22}$$

By getting divergence from Eq(3-21) and considering the fact that the velocity field is divergence-free (Eq(3-22)), pressure can be obtained by solving the following Poisson equation within each time step:

$$\nabla^2 p^{n+1} = \frac{\rho}{\Delta t}\nabla.\vec{V}^* \tag{3-23}$$

Due to the explicit discretization scheme, time step (Δt) as well as grid spacing should be chosen to satisfy the stability criteria. The conditions of stability of this finite-difference scheme are [73]:

$$\frac{1}{2}\frac{\rho}{\mu}(u^2+v^2)\Delta t \leq 1 \tag{3-24}$$

$$\frac{4\mu\,\Delta t}{\rho\,\Delta x^2} \leq 1 \tag{3-25}$$

3.3.3 Boundary conditions

A no-slip, no-penetration boundary condition on the solid wall is applied by setting the components of velocity to zero on the wall surfaces.

For the energy equation, a constant temperature is considered on the top and bottom walls, while the side walls are considered to be ideally insulated by setting the derivative of temperature to be zero there.

A condition of zero-mass flux is enforced on the solid walls for the conservation of species equation. According to Eq(3-12) by setting $\overrightarrow{j_1} = 0$, the zero-mass flux condition on the boundaries can be written as:

$$\frac{\partial c}{\partial \eta} = -c_0(1-c_0)S_T\frac{\partial T}{\partial \eta} \tag{3-26}$$

in which η is the normal unit on the boundary. Eq(3-26) indicates that mass flux on the surface is related to a temperature gradient as a result of the Soret effect. The magnitude of the flux is strengthened by the Soret coefficient and the temperature gradient on the surface. Species separate on the heated walls and then diffuse toward the domain as a result of mass diffusion (Fick's law). Thus, it can be concluded that the maximum separation in the cell is governed by the Soret coefficient and the applied temperature gradient, and the time in which this maximum separation is achieved (steady-state time) is governed by the molecular diffusion coefficient as the diffusion time.

As shown earlier, the pressure is obtained by solving a Poisson equation (Eq((3-23)). However, the values of pressure on the boundaries are unknown and proper boundary conditions are needed for the pressure field. It has been shown [73] that it is possible to apply a Neumann boundary condition when using a projection method with a staggered grid. This can be achieved by projecting the vector equation (3-21) on the boundary Γ. Thus, the following expression will be obtained:

$$\left(\frac{\partial P}{\partial \eta}\right)_{\Gamma}^{n+1} = -\frac{1}{\Delta t}\left({V_{\Gamma}}^{n+1} - {V_{\Gamma}}^{*}\right) \cdot \eta \qquad (3\text{-}27)$$

where the value of ${V_{\Gamma}}^{*}$ is not yet defined. By considering the value of the provisional velocity (${V_{\Gamma}}^{*}$) to be equal to the value of velocity on the boundary, the Neumann boundary condition is obtained.

3.3.4 Discretization and solvers

The discretization of the equations is conducted using a finite-difference second-order central scheme. As described earlier, pressure-velocity decoupling is performed using a projection method (explicit first-order in time) on a staggered grid domain. The convective terms are treated in a non-conservative form. The diffusion terms are discretized using a second-order central finite-difference scheme. The Poisson equation of pressure is solved using SOR (Successive over-relaxation method). Other governing equations including conservation of energy and chemical species are solved using an implicit scheme: forward in time (first-order), central in space (second-order), and using PGS (Point Gauss–Seidel) with relaxation.

3.4 Solution control

The numerical solution is controlled by different factors and parameters. Several investigations should be performed in order to check the independency and the efficiency (in terms of computation time) of obtained solution.

3.4.1 Convergence criteria

In any iterative method, the solution has not converged until a convergence criterion is satisfied. If the convergence criteria are not chosen appropriately, the accuracy of the solution is affected through time. On the other hand, applying very strict criteria would result in larger computational time. In the scope of the current study, this is a major concern. The thermodiffusion process is a slow process and a typical simulation takes more than 12 hours (15E6 time steps). Thus, the simulations might last from weeks to even a couple of months depending on the convergence conditions chosen. Therefore, using proper criteria is of great importance.

The residual for the current study is defined as the relative difference between two successive iterations. However, for the concentration field, since we are dealing with very small values (order of 10^{-11} in each time step) we have chosen the absolute difference of two successive iterations. A summary of the convergence criteria used in the simulations are included in Table 3-1. Several simulations have been performed to verify the independency of the solution from the convergence criteria.

Table 3-1: Convergence criteria used in the numerical code.

Equation	Solving parameter	Residual calculation method	Convergence criteria
Pressure Poisson	Pressure	Relative	10^{-6}
Energy	Temperature	Relative	10^{-5}
Chemical Species	Mass fraction	Absolute	10^{-13}

3.4.2 Relaxation factors

Relaxation factors can speed up the convergence process. In the current study, it was found that more than 90% of the CPU time was devoted to the calculation of the pressure field. The pressure field is directly related to the applied gravitational acceleration and changes considerably in each time step (in case of oscillatory gravity or g-jitter). The over-relaxation factor for the SOR solver can save considerable amount of time for the user. Figure 3-4 illustrates the CPU-time for the first 100 timesteps of a typical case (in the presence of oscillatory gravity).

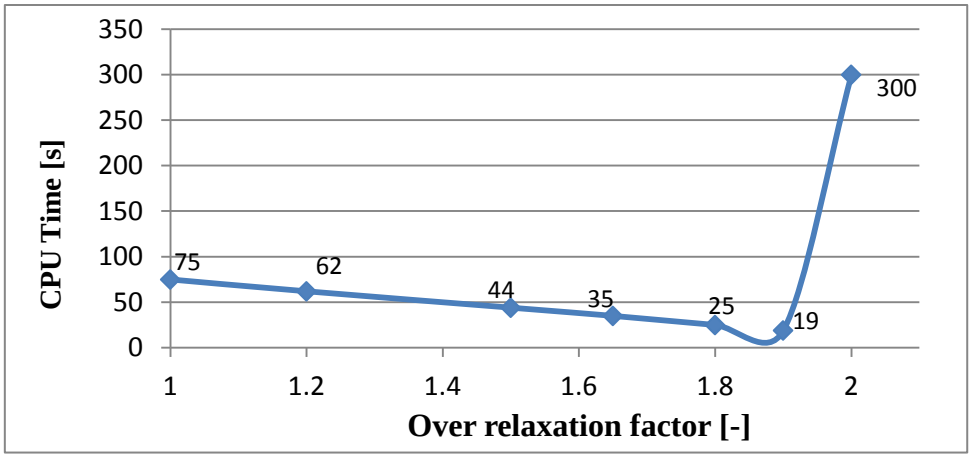

Figure 3-4: The effect of over-relaxation-factor of SOR solver on the Cpu time

As shown, the value of the over-relaxation factor has a significant effect on the computational time. For instance, by choosing 1.9, the process is accomplished 4 times faster when compared with the case when no relaxation factor is used (equal to 1). This can reduce a month-long simulation to a week. This figure also shows that the over-relaxation factor should be maintained between 1 and 2 as the CPU-time increases abruptly for values close to 2.

The simulations in the current study have been performed by choosing relaxation factor of SOR solver equal to 1.8. The other relaxation factors (for energy and chemical species equations) were set to 1 as their effect on the CPU-time was found to be insignificant.

3.4.3 Grid dependency

The simulations have been performed on 4 different mesh resolutions for a sample case with $\Delta T = 10℃$ and a constant gravity vector applied perpendicularly to the temperature gradient (g_x=*0.0005 m/s*^{2}). The results are shown in Table 3-2 where the normalized separation rate of the species and maximum temperature deviation with respect to the ideal zero-gravity case is compared to the steady-state condition. The normalized separation rate is the difference between the mass fraction of the carrier component (water) on the hot and cold walls (separation) divided by the maximum achievable separation in an ideal zero-gravity condition. The numerical results at different mesh sizes clearly indicate the grid independency of the numerical solution.

Table 3-2: Grid independency of the numerical solution (g_x = 0.0005 m/s^2)

Grid size	Normalized separation rate [%]	maximum temperature deviation [K]	Cpu time [Hours] for total simulation
12 x 12	78.02	1.206E-02	3
22 x 22	81.08	1.113E-02	11
32 x 32	81.63	1.094E-02	40
42 x 42	81.81	1.088E-02	70

The results of Table 3-2 are plotted in Figure 3-5, where the dependent variables are plotted versus the inverse of the total number of grid points. As shown, the values converge when the system tends toward a fully continuum condition (number of grids^{-1} ~ 0).

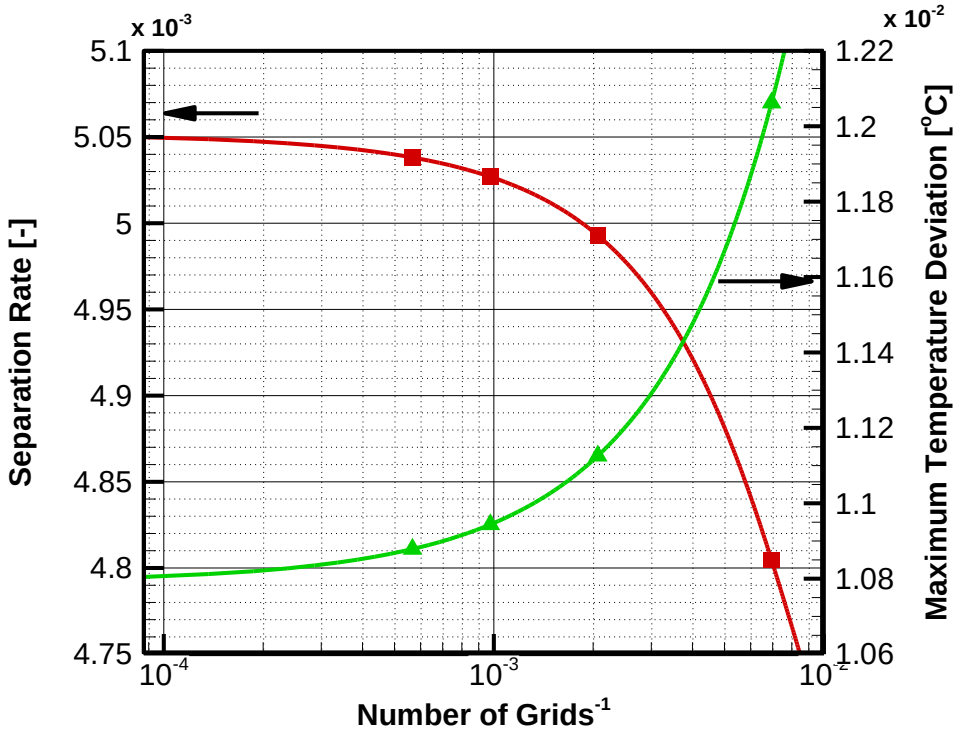

Figure 3-5: Variation of depended variables for different grid densities

The grid independency of the solution is also evident in Figure 3-6, where the transient separation profile is plotted. The solution converges as the mesh resolution increases. Accordingly, the grid size of 32x32 has been chosen for the rest of simulations, which is the case of optimized computational time and accuracy.

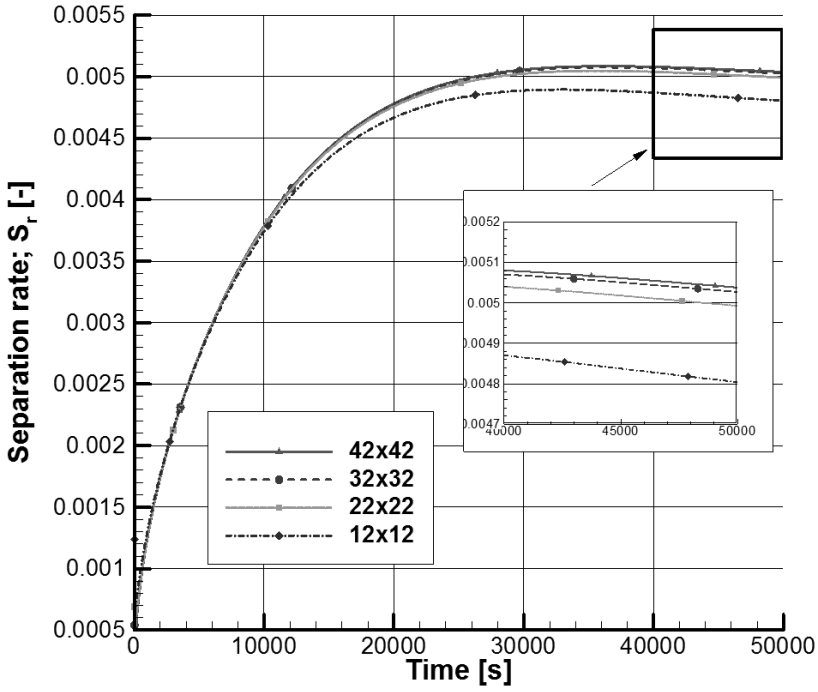

Figure 3-6: Transient separation rate profile for different grid resolutions

3.4.4 Time step control

The effect of the length of the time step on the accuracy of the solution was investigated. There are three factors that restrict the timestep. Choosing large timesteps might result in an inaccurate solution or even divergence due to the use of the explicit scheme. On the other hand, smaller time steps increase the computational time, and finally very small time-steps increase the error of computation due to an increase in round-off error. A double-precision real number in Fortran can be represented by up to 17 digits before truncation occurs. Roughly speaking, the changes in the concentration fields are very small and are in order of 10^{-9} in each second.

In this study the effect of high-frequency vibration on the flow characteristics is of interest; therefore, it is a preference to choose small time steps to provide enough acceleration data points for the code. Various time steps have been tested (0.002s ~ 0.03s) and the results were compared. It was found that a time step of 0.01 s is sufficiently small to guarantee the stability and accuracy of the solution.

3.5 Numerical code

A double-precision CFD code has been developed in FORTRAN. The program is written in a way to optimize the computational power. The program consists of 22 subroutines and more than 1200 lines.

3.5.1 Program algorithm

The program algorithm is illustrated in Figure 3-7 in the form of a flow-chart diagram. In the beginning, the program reads the problem characteristics from the input text files which include all of the options that need to be assigned by the user. These options include the physical properties, dimensions, boundary conditions, solution control parameters, and gravity data which can be either a constant, harmonic equation, or a series of raw data files. In the next step, the code manages a calculation loop which continues until the end of simulation. In each time step, first the Navier-Stokes equations are solved using the described projection method in a multi-step process. Next, the temperature and concentration fields are updated for each timestep. The shaded boxes in the flowchart diagram indicate where a convergence loop is employed.

For exporting the solution at pre-defined times into ASCII formatted files, the solution is written on a single uniform grid. This is done by interpolating the velocity component in accordance to main grid points. The code has the capability to restart from any moment even in the case of g-jitter vibration where the vibration information is provided as raw acceleration ASCII files.

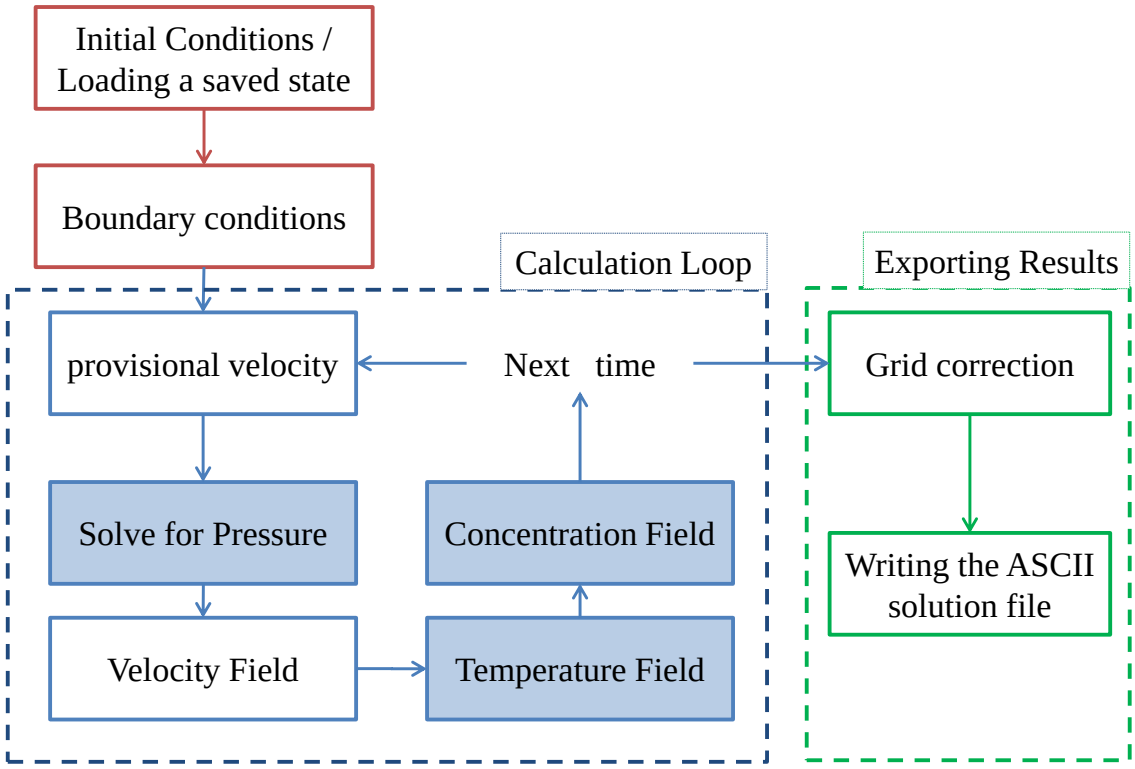

Figure 3-7: Flowchart of the CFD program

3.5.2 Post processing

The main post-processing tasks of the current study are performed using Tecplot®. The output files of the program are compatible with Tecplot®. Further analysis of the current study has been accomplished in Matlab®. Several Matlab® codes have been developed to read the ASCII data files and perform the needed analysis and plot the results.

3.6 Validation of the numerical code

In order to check the accuracy of the code, some benchmark cases for the heat transfer inside a cavity are simulated and the results are compared with benchmark studies [77-79].

In these benchmark cases, a square cavity is subjected to a temperature difference and a constant gravity vector perpendicular to the main temperature gradient. The values for minimum, maximum, and average Nusselt number on the hot wall of the cell are obtained and compared with other investigations as demonstrated in Table 3-3. The Rayleigh number is a dimensionless measure of the ratio of the destabilizing effect of buoyancy to stabilizing effect of the molecular diffusion of momentum and is defined as $Ra = \frac{g_x \beta_T \Delta T L^3}{\nu \chi}$ in which g_x is the gravitation acceleration in x direction, β_T is the thermal expansion coefficient, ΔT is the temperature difference between the hot and cold wall, L is the length of the cavity, and ν and χ are the kinematic viscosity and thermal diffusivity of the fluid, respectively.

Rayleigh number	Nusselt number	Current Study	Ref. [77]	Ref. [78]	Ref. [79]
10^3	Max.	1.492	1.5	1.47	1.501
	Min.	0.687	0.692	0.623	0.691
	Ave.	1.113	1.12	1.074	1.117
10^4	Max.	3.624	3.53	3.47	3.579
	Min.	0.578	0.586	0.497	0.577
	Ave.	2.252	2.243	2.084	2.254
10^5	Max.	7.972	7.71	7.71	7.945
	Min.	0.689	0.729	0.614	0.698
	Ave.	4.567	4.52	4.3	4.598

Table 3-3:Comparison of the results of current study with other investigations

The variation of dimensionless temperature between the hot and cold wall in the centerline of the cavity is illustrated in Figure 3-8 for different Rayleigh numbers. The dimensionless temperature is defined as $\bar{T} = \frac{T - T_c}{T_h - T_c}$ in which T_c and T_h are temperatures of the cold and hot wall, respectively. As shown, the numerical results of the current study are in good agreement with other benchmark studies, indicating good performance and accuracy of the code. In addition to the presented quantitative comparisons, the fluid flow structure is compared with the benchmark studies. In Figure 3-9 the streamlines of the flow are plotted and compared with the contours of streamline function of Wan *et al.* [79]. This figure shows the reliability of the code to simulate the buoyancy driven flow even for high Rayleigh numbers.

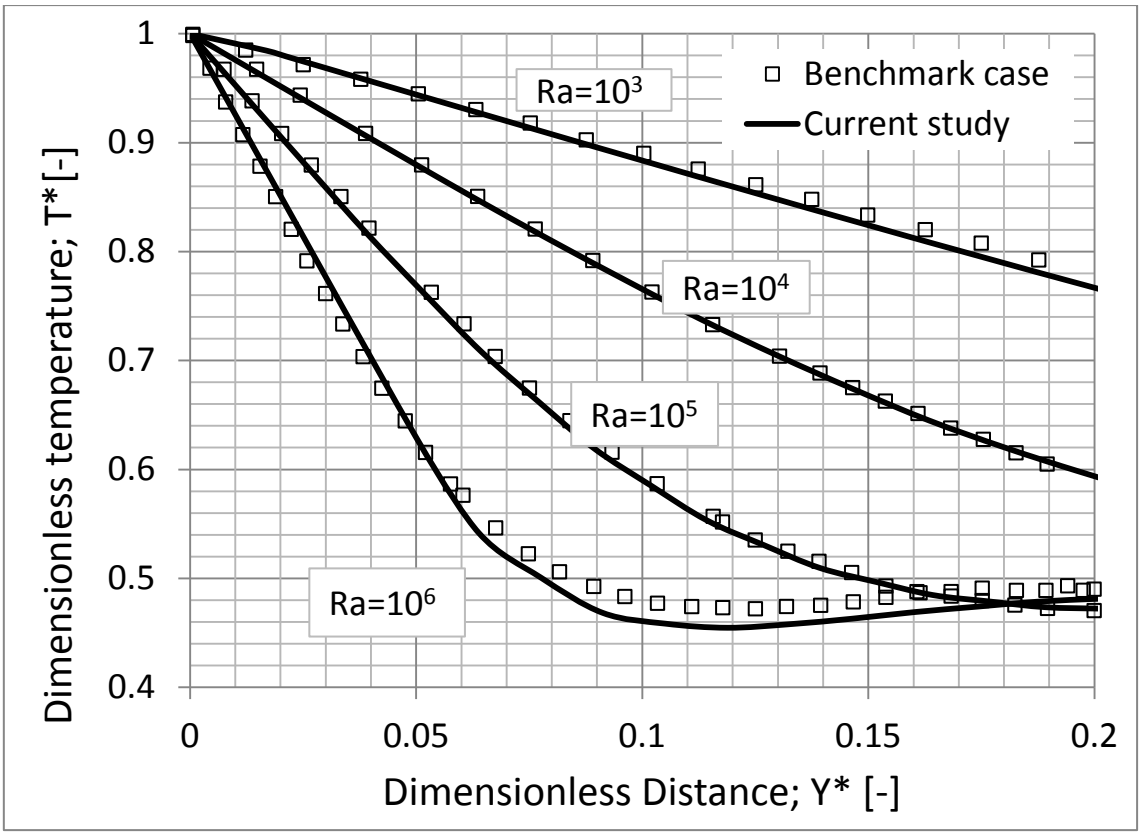

Figure 3-8: Dimensionless temperature profile (comparison with [79]**).**

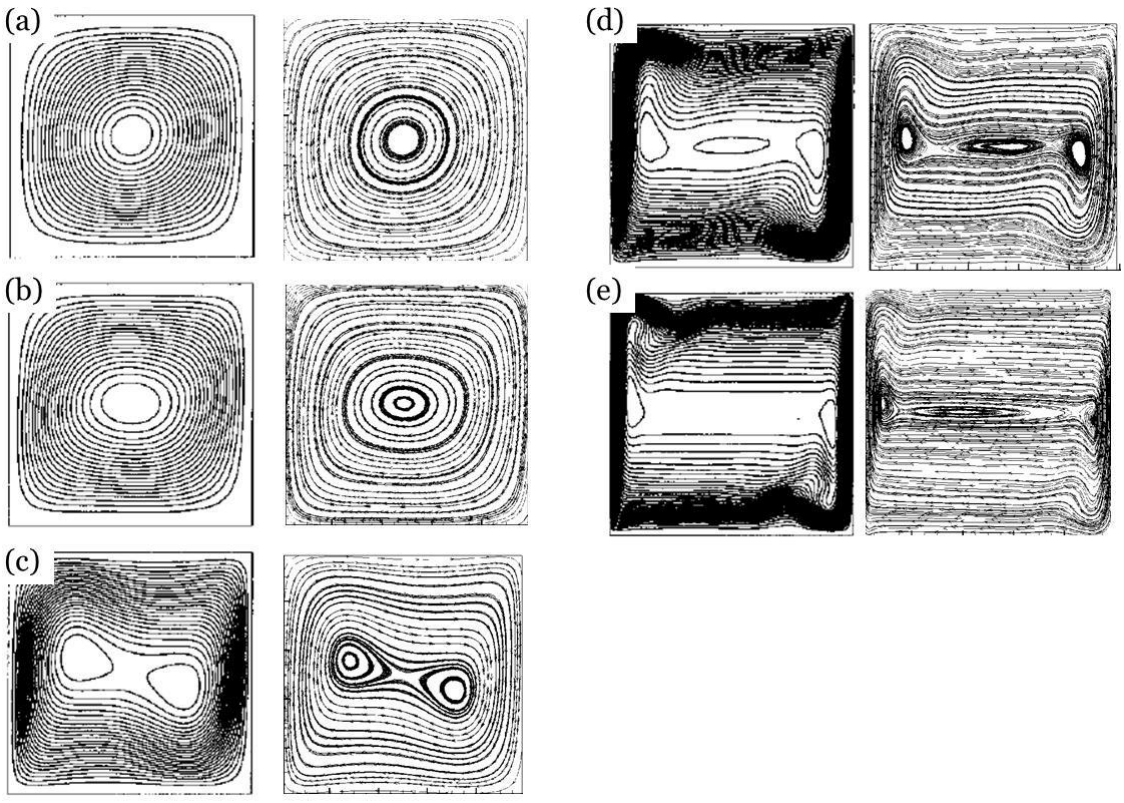

Figure 3-9:Streamlines of the Wan et al simulation (left column) [79] **and current study (right column) for different Rayleigh numbers: (a) Ra= 10^3, (b) Ra= 10^4, (c) Ra= 10^5, (d) Ra= 10^6, (e) Ra= 10^7**

Chapter 4 Results and Discussion

The focus of this dissertation is on the flow characteristics of a typical thermodiffusion experiment (water/IPA mixture 90:10 wt.%) that is subjected to different gravity conditions. Three kind of gravity fields have been analyzed: static (constant), pure oscillatory, and g-jitter. Thus, the gravity field can be written as follow:

$$g = g_{st} + g_{vib}\ \sin(2\pi ft) + g_{jitter} \tag{4-1}$$

in which g_{st} is the static (residual) gravity, g_{vib} and f are the magnitude and frequency of the oscillatory gravity, respectively, and g_{jitter} is the g-jitter component. The separation rate S_r has been used to quantify the component separation. It is defined as the difference between the average mass fraction of the carrier component (water) on the hot and cold wall;

$$S_r = (\tilde{c}_h - \tilde{c}_c) \tag{4-2}$$

in which $\tilde{c}_h$ and $\tilde{c}_c$ are the average values for mass fraction of water on the hot and cold walls, respectively. The quality of a thermodiffusion experiment can be indicated by its normalized separation rate S_r^* which is the ratio of the separation rate to the maximum possible separation rate in an ideal, zero-gravity condition:

$$S_r^* = S_r \Big/ S_{r\,ideal} \tag{4-3}$$

The calculation of the local Nusselt number is performed on the heated walls according to the following equation:

$$Nu_x = \frac{h_x L}{k} = \frac{-1}{2}\frac{\partial T}{\partial y}\frac{L}{(T - T_r)} \tag{4-4}$$

in which h_x is the local heat transfer coefficient and T_r is the reference temperature (25°C). The gradient of the temperature on the surface is calculated using a third-order finite difference scheme with the use of 4 points:

$$\frac{\partial T}{\partial y} = \frac{1}{3}\frac{-9.2T_j + 11.25T_{j+1} - 2.5T_{j+2} + 0.45T_{j+3}}{dy} \tag{4-5}$$

The coefficients are calculated based on the expansion of the Taylor series. It should be noted that due to the use of a staggered grid, the distance between the first two grid points is half of the standard grid spacing dy.

In the following section, we will briefly discuss the effects of the orientation of the cell in order to indicate the most critical alignment. Moreover, we will show how the static residual and pure oscillatory gravity fields affect the diffusion process. At the end we will discuss the effects of g-jitter using different approaches.

4.1 Physical properties

The properties of the mixture used in the simulations are listed in Table 4-1. These properties have been used by other researchers for the same mixture [56,59]. As described earlier, the properties are considered to be constant and are not affected by the variation of temperature and concentration.

Table 4-1: Physical properties of the mixture; Water/Isopropanol (90%wt) at 25°C.

Parameter	Density (ρ)	Kinematic viscosity (υ)	Thermal diffusivity (χ)	Molecular Diffusion Coefficient (D_c)	Soret Coefficient (S_T)	Thermal expansion coefficient (β_T)	concentration expansion coefficient (β_c)
Unit	kg/m^3	m^2/s	m^2/s	m^2/s	1/K	1/K	-
Value	984	1.4 E-6	1.3 E-7	8.7 E-10	-7 E-3	3.1 E-4	0.138

4.2 Influence of orientation of the cell

In a thermodiffusion experiment, flow is induced inside the experimental cell as a result of a density gradient. For the case of static gravity, the angle between the acceleration vector and the temperature (density) gradient fundamentally controls the stability of the fluid flow. The angle (α in Figure 3-1) may vary from 0 to 180 degrees which corresponds to the case of heating from the bottom or top, respectively. Figure 4-1 illustrates the separation process during 13.8 hours for the case of a 5°C temperature difference between the hot and cold walls subjected to a residual gravitational field of $g_x = 0.005\, m/s^2$. The separation process is highly affected in the case of α = 90°, in which the gravity field is perpendicular to the density gradient. In this case the induced flow inside the cell is the strongest.

In contrast, for cases of α=0 and α=180° the induced flow is weak and the process is dominated by diffusion as the separation follows the trend of ideal zero gravity.

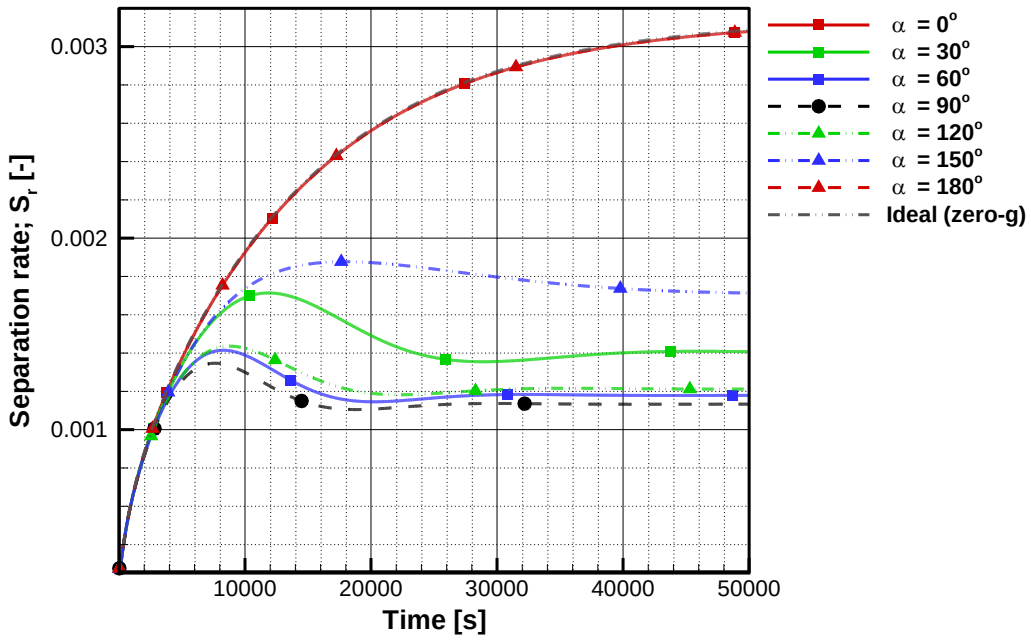

Figure 4-1: Effect of orientation of the cell on separation process

Figure 4-2, shows the normalized separation rate (Eq(4-3)) for different cell orientations at steady state. This figure shows that the impact of residual acceleration applied orthogonally to the direction of the temperature gradient negatively affects the thermodiffusion process. Moreover, the separation is more restricted for cases of heating from below (α < 90°) compared to heating from the top (α > 90°) due to more stable flow conditions for the former case. The results shows that with a residual acceleration smaller than $g_s = 10^{-3}\ m/s^2$, disturbances from the static gravity field can be avoided by proper orientation of the experimental cell (α = 0). This finding is consistent with pervious investigations [47].

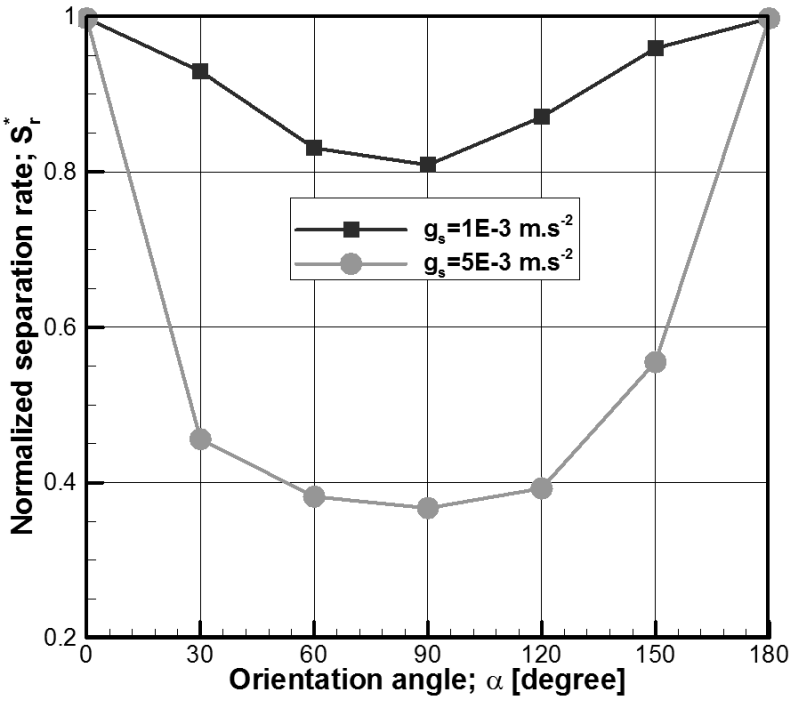

Figure 4-2: Effect of orientation angle on the steady-state separation

4.3 Influence of residual gravity

In the presence of residual gravity, flow is induced as long as there is a density variation in the domain. When this convective motion comes into the picture, the process is not only governed by pure diffusion, as the separation will be influenced by the mixing effect. The effect of the magnitude of static gravity (applied in the orthogonal direction to the temperature gradient) on the separation of species is shown in Figure 4-3. The results show that residual gravity, depending on its magnitude, restricts the separation of species due to the mixing effect; the higher the magnitude of residual gravity, the less separation of species.

The other effect of convection is that the system reaches a steady-state condition much faster. As seen for the case of $g_s = 5 \times 10^{-4}$, 2×10^{-3} and $0.01\, m/s^2$ the system reaches a steady-state condition in 13.8, 10.5 and 3 hours, respectively. This shows that the deviation of a steady-state time from the diffusion time could be used as an indication of the role of convection inside the cell. It is also evident in Figure 4-3 that for $g_s = 10^{-4}\, m/s^2$ the process is dominated by diffusion, and the negative effect of gravity is practically negligible.

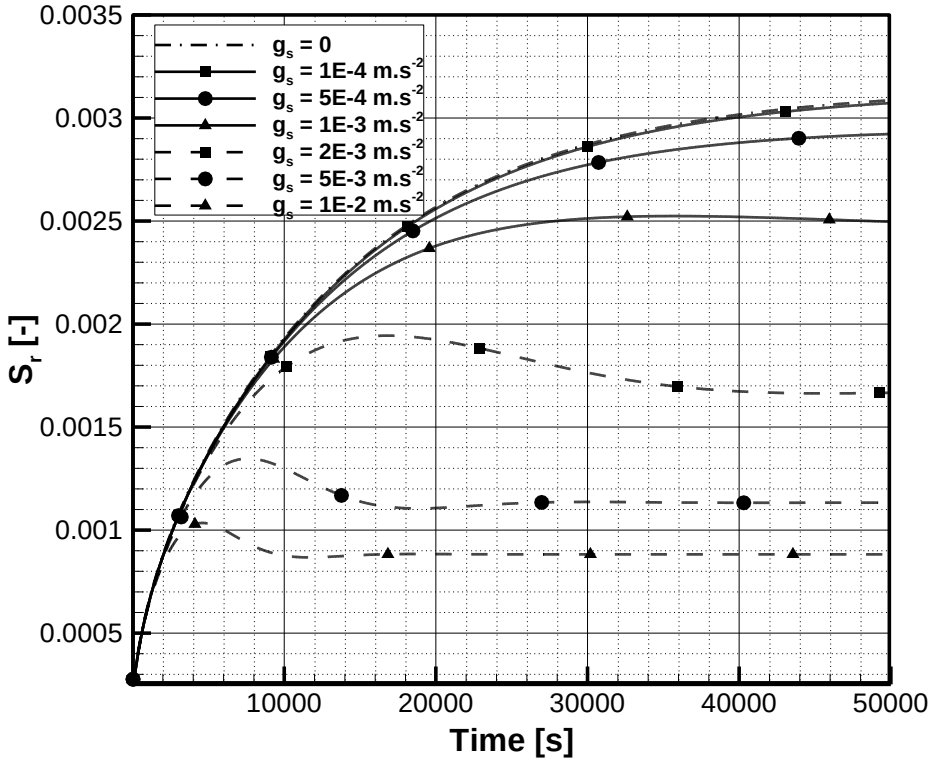

Figure 4-3: Separation of components subjected to static gravity field for ΔT=5°C

In addition to the separation rate, the concentration field is affected by the fluid flow inside the cell. Figure 4-4 illustrates the contours of the concentration of the water mass fraction in the presence of different static gravity fields. Increasing the magnitude of the gravitational acceleration (Figure 4-4-b) deviates the concentration field from the linear distribution as a result of the mixing effect. In the case of $g_s = 2 \times 10^{-3}\, m/s^2$, the isotherms (Figure 4-4-c) are highly distorted by this effect, and by increasing g_s to $0.01\, m/s^2$ the effects of mixing become significantly noticeable (Figure 4-4-d).

This effect also can be observed in Figure 4-5, which shows the mass fraction of water on the center line of the cell between hot (Y=0) and cold (Y=0.01m) wall. For low residual gravity fields, the variation of the mass fraction between the walls is close to linear. However, by increasing the strength of the gravity field, the mass fraction of water is maintained closer to the initial value (c=0.9) due to flow convection and mixing, which restrict the Soret effect.

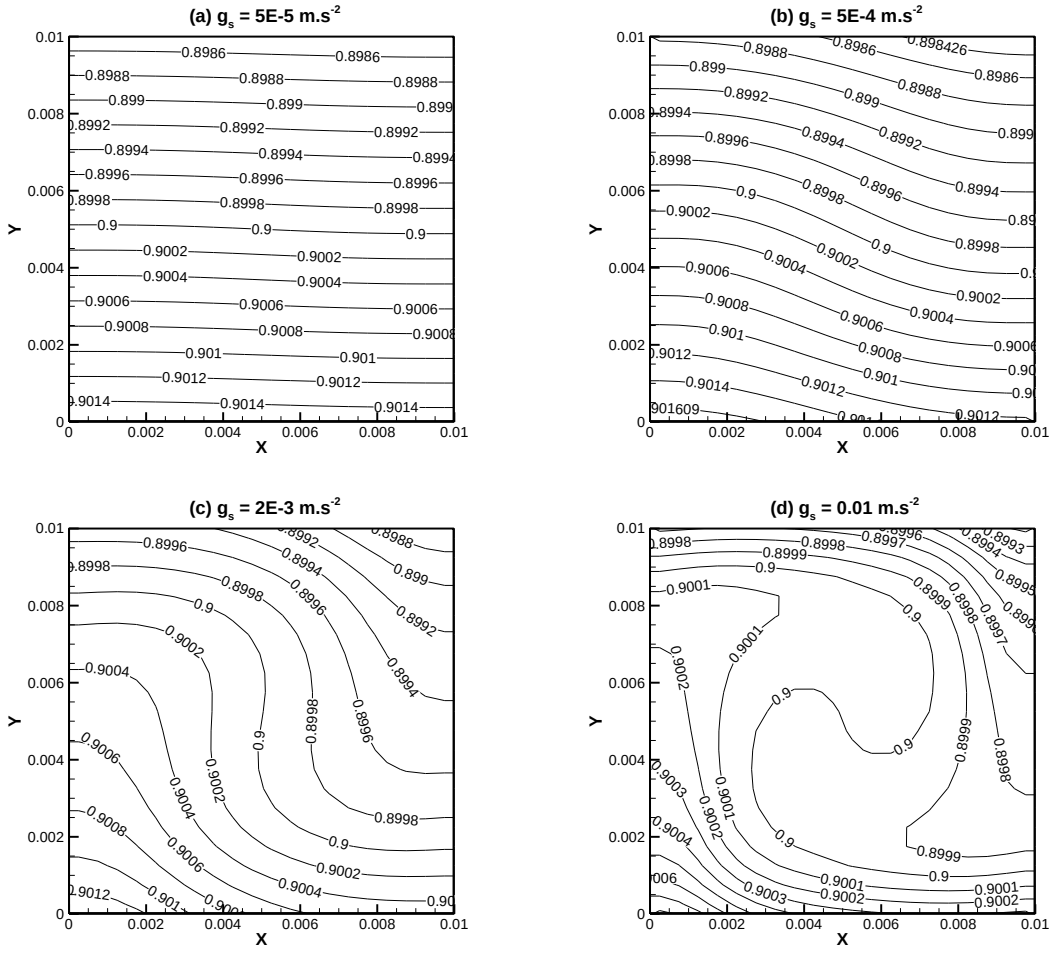

Figure 4-4: Concentration field in presence of static gravity (ΔT=5°C).

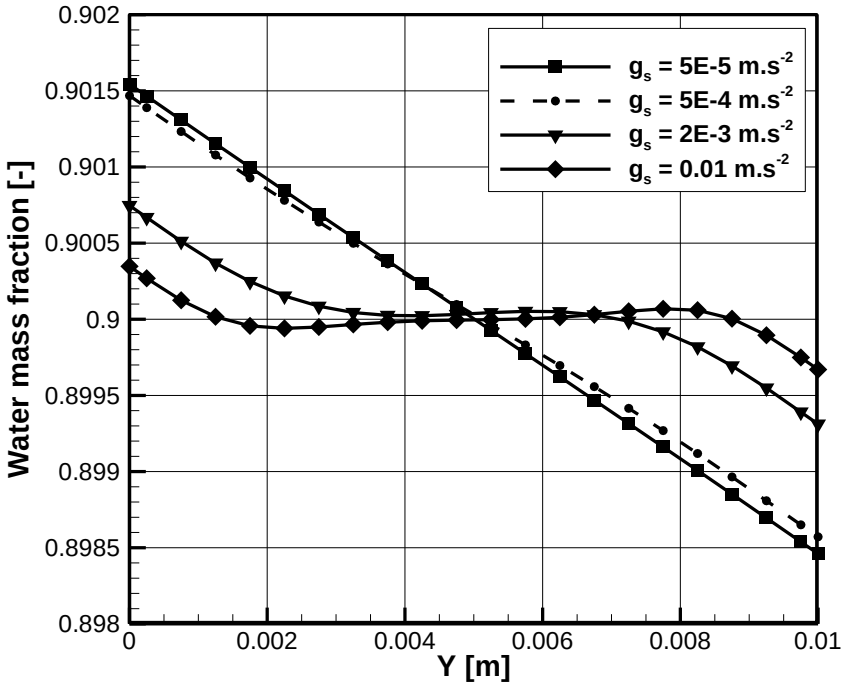

Figure 4-5: Variation of mass fraction of water along the middle vertical line.

The flow structure is always a single-cell in the range of $0.5 < g_s < 10^{-6}\ m/s^2$). The typical pattern of velocity vectors inside the cell is shown in Figure 4-6. The magnitudes of the velocities depend on the applied gravitational acceleration, the density difference in the cell (due to temperature and concentration variation), and the dimensions of the cell. Figure 4-7, illustrates the mean value of the induced velocity inside the cell versus the residual gravity for two different applied ΔT. As shown, one can consider a certain relationship between the mean value of acceleration and gravitational acceleration while keeping the other parameter constant (ΔT).

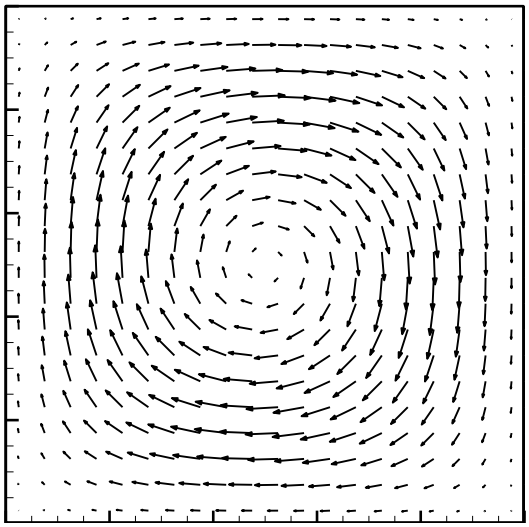

Figure 4-6: Typical flow pattern inside the cell in presence of residual gravity field.

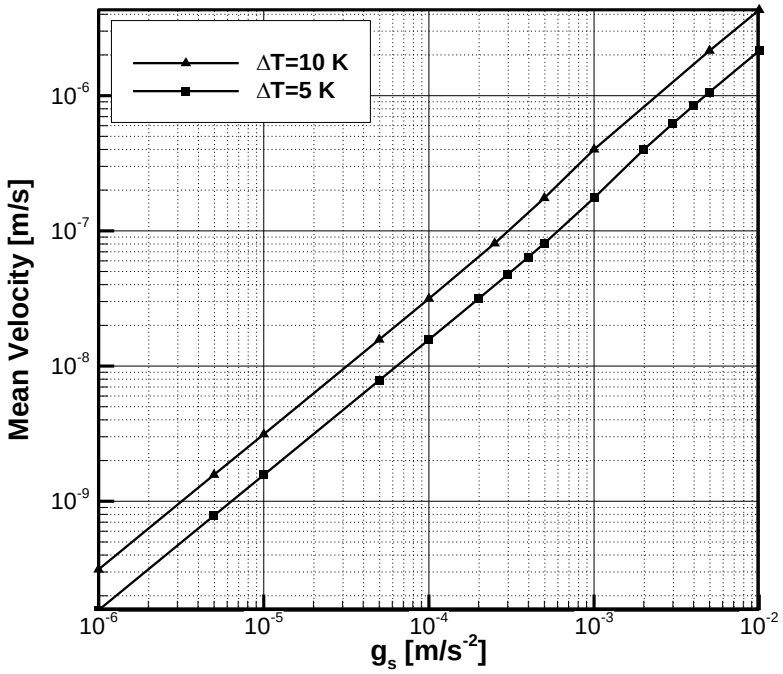

Figure 4-7: Mean velocity versus magnitude of residual gravity

Thus, depending on the experimental conditions, including the physical properties of the mixture and the temperature difference, there is a critical value for the residual gravity that indicates the suitability of the thermodiffusion experiment. The heat transfer process can be represented by the Rayleigh number, which is a dimensionless measure of the ratio of the destabilizing effect of buoyancy to the stabilizing effect of the molecular diffusion of momentum and buoyancy and is defined as:

$$Ra = \frac{g_s \beta_T \Delta T L^3}{\nu \chi} \tag{4-6}$$

Several simulations have been performed for different ΔT and g_s for the mixture. The results are shown in Figure 4-8, in which the variation of the average Nusselt number and normalized separation rate are plotted versus Rayleigh number. The results show that for a Rayleigh number less than a critical value, i.e. $Ra_{cri} = 1$, the process is dominated by the Soret effect and the separation of components is close to the ideal condition ($Sr^* \sim 1$).

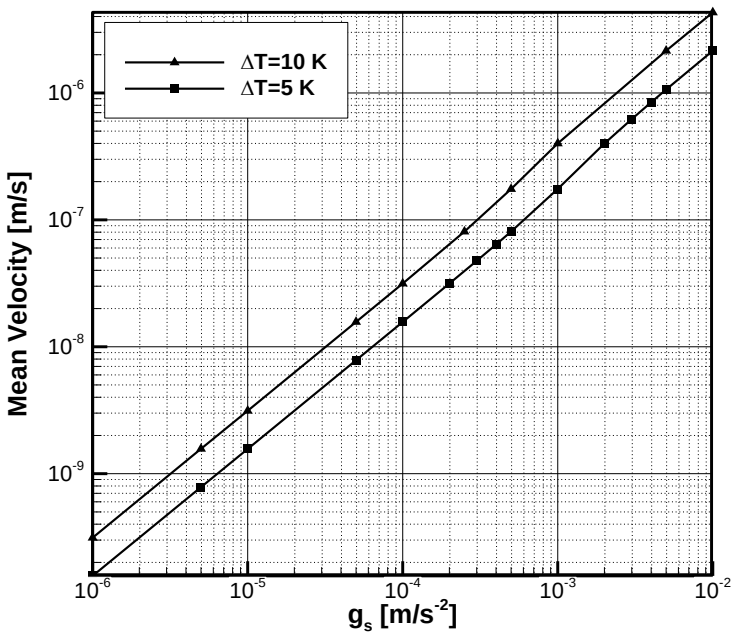

Figure 4-8: Normalized separation and Nusselt number versus Rayleigh number

A further increase in the Rayleigh number results in greater deviation from the ideal zero-g condition, whereas a steep reduction in the separation rate is observed. In this state, the role of convection and mixing becomes noticeable, for example for a *Ra* = 200, only 20% of the ideal separation can be obtained. Figure 4-8 also illustrates the variation of the Nusselt number.

It is interesting to note that the variation of the Nusselt number is smooth in the range of Ra < 100 and remains close to 1. This shows that even a small increase in the Nusselt number can result in large error in a thermodiffusion experiment. The Nusselt number is widely used to indicate the contribution of convection; however, for thermodiffusion experiments its usefulness is controversial. Thermodiffusion is a slow process, which deals with very small changes in the mass fraction of species. Thus, any small disturbance might significantly alter the quality of the experiment.

It is worthwhile to mention that for the current mixture, because of the negative Soret coefficient, the heavier component (water) migrates toward the hot side, which is the low-density region. This means that as separation proceeds, the density difference in the system decreases due to weaker induced convection. Therefore, the conditions for thermodiffusion in mixtures with a positive Soret coefficient are more critical, since separation occurs is in a way that intensifies the density gradient in the cell.

4.3.1 The positive effect of induced convection

The mixing effect dominates when the convective transport of the species becomes significant enough that the gradient of concentration becomes trivial. In this condition, strong vortices transport the chemical component from a high-density region to a low-density one, providing a uniform distribution of species. The negative effects of convection on thermodiffusion have been the subject of many studies. However, the induced flow can sometimes be beneficial in terms of increasing the separation. To the best knowledge of the author, this phenomenon has not been discussed in the literature.

In the presence of convection, heat transfer on the heated wall increases. According to Eq(3-26), the flux of species on the wall is related to the temperature gradient. Therefore, by increasing the local temperature gradient (Nusselt number), the separation of species is locally augmented. Although, due to a strong mixing effect, the average separation rate might decrease overall.

The local values of the Nusselt number on the hot wall are plotted in Figure 4-9, for different magnitudes of residual gravity. For small gravity magnitudes ($g_s < 0.01 ms^{-2}$), the local variation of the Nusselt number is close to 1. However, these small variations will affect the thermodiffusion process.

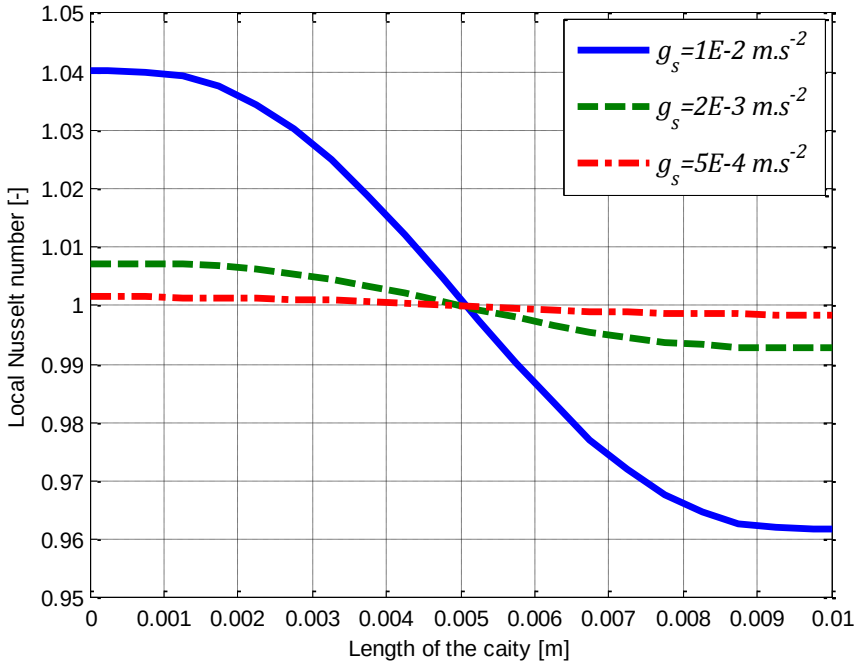

Figure 4-9: Local Nusselt number on the hot wall for different gravity fields

The average Nusselt number increases smoothly with an increasing residual gravity, as illustrated in Figure 4-8. Nevertheless, the value of the local Nusselt number is larger than 1 on the left side and smaller than 1 on the right side. As one can predict, the local separation follows the same trend accordingly. However, the mixing is becoming more dominant at the same time. The opposition between these phenomena determines the concentration field. For comparison, the mass fraction of water on the hot wall is shown in Figure 4-10 for different values of the same conditions.

By considering Figure 4-9 and Figure 4-10, it is evident that an increase in the local heat transfer results in more separation. However, mixing effect dominate in most of these cases. Interestingly, for the case of $g_s = 5E-4$, the maximum of the mass fraction on the hot side is even larger than in the case of pure diffusion ($g_s = 5E-5$), which demonstrates the positive effect of convection on the separation process. However, the average value of mass fraction is still less than the ideal case.

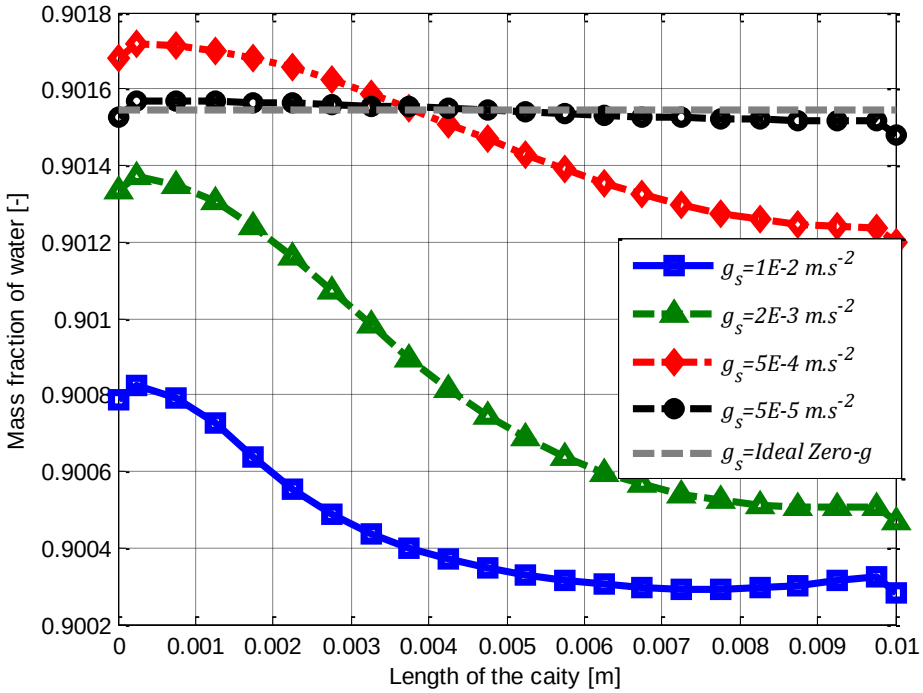

Figure 4-10: Local mass fraction of water along the hot wall

4.4 Influence of oscillatory gravity

The effects of a pure oscillatory gravity field on a thermodiffusion experiment are investigated by considering the following expression for the gravity vector when the cell is subjected to an external vibration perpendicular to the main temperature gradient:

$$\vec{g} = g_x = A(2\pi f)^2 \sin(2\pi ft) = g_{vib} \sin(2\pi ft) \qquad (4\text{-}7)$$

in which A and f are the amplitude and frequency of the applied vibration, respectively, and $g_{vib}=(2\pi f)^2 A$, which is the amplitude of the oscillatory gravity. In this study, the effects of vibrational gravity were surveyed by considering several cases with different values for f and g_{vib} as shown in Table 4-2. These values were chosen in order to cover the range of performed experiments in the IVIDIL project, in terms of frequency and amplitude of the oscillatory gravity.

In the literature, the vibrational Rayleigh number has been widely used in order to characterize the strength of vibrationally induced convection. It was suggested that it should be called the Gershuni number [13] in honour of his significant contribution to the theory of thermal vibrational convection. This number is defined according to Eq(4-8).

Table 4-2: Range of studied parameters

Parameter	f (frequency of vibration) [Hz]	g_{vib} (Amplitude of oscillatory gravity) [m/s^2]
Range of study	0.05 ~ 2 (0.05, 0.2,0.5, 1, 2)	0.1 ~ 9.8 (0.1, 0.3, 0.7, 1, 4, 7, 9.8)

$$Gs = \frac{\left(2\pi\, fA\beta_T \Delta TL\right)^2}{2\chi\nu} = \frac{\left(g_{vib}\beta_T \Delta TL / 2\pi f\right)^2}{2\chi\nu} \tag{4-8}$$

In the presence of an external vibration, a single-cell flow is induced in the domain (similar to Figure 4-6), which is harmonized according to the applied vibration. The direction of the flow changes from clockwise to counter-clockwise with respect to the sign of the acceleration. This is called as the "fast" response. Separation of the components proceeds due to the Soret effect and might be affected by the induced flow field. Nevertheless, even in the presence of large induced velocities, thermodiffusion is not immediately affected by the "fast" response of the fluid. This is because of the rapid changes in the instantaneous velocity field. However, due to the non-linearity of the system the average flow field during a periodic excitation is not zero. In fact, in addition to the mentioned "fast" response, there is also a "slow" motion, which can be characterized by examining the average flow field in the period of excitation. This "slow" motion is relatively stable during the experiment, and it affects the distribution of the species.

4.4.1 Effect of frequency and amplitude of the oscillatory gravity

The significance of induced convection in the cell can be characterized by the magnitude of the induced velocity. Figure 4-11 illustrates the maximum value of the induced velocity in the cell after t = 13.8 h for different cases. It is evident that the induced velocity decreases with increasing the frequency of excitation for constant amplitude of oscillatory gravity. Within the short available time in each period, fluid particles are not able to accelerate further. Moreover, a decrease in the amplitude of the oscillatory gravity results in a lower induced velocity in the system.

Interestingly, different excitations might result in the same velocity fields. For instance, an excitation with $g_{vib} = 0.1\ m.s^{-2}$ and $f = 0.5\ Hz$ results in the same maximum velocity with the case of $g_{vib} = 0.3\ m.s^{-2}$ and $f = 2\ Hz$. However, in spite of this similarity, the effect on the diffusion process is not the same and is more dependent on the average flow regime ("slow" motion) as will be discussed in the following section.

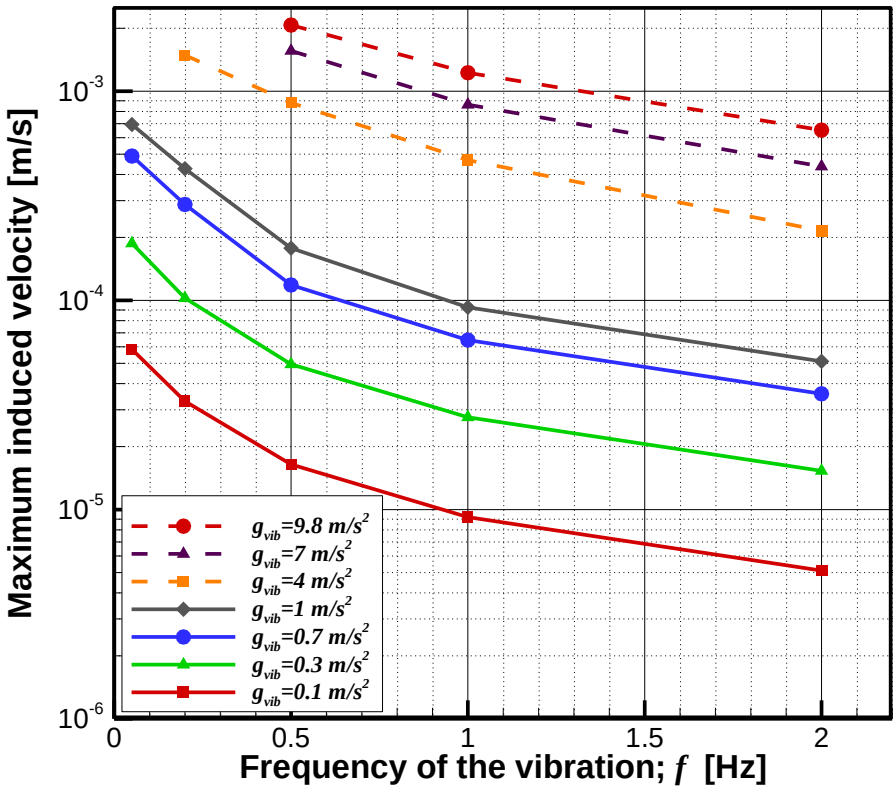

Figure 4-11: Maximum induced velocity versus frequency of excitation

The average flow field is obtained by finding the average of flow properties in each grid point for the period of the excitation. The average flow fields presented here were obtained after the steady-state time for the diffusion process (t > 13.8h). Average velocity vectors are shown in Figure 4-12 for different frequencies and amplitudes of excitation. Starting from the upper right of the figure, the average flow pattern is a weak cell. As the frequency decreases or the magnitude of vibration increases, 4 symmetric cells appear. Further on, two of the vortices merge and a 3-cell pattern with a large central diagonal vortex is formed (Figure 4-12-lower left). The strength of the average velocity field increases from the upper right of the figure to the lower left. The 3-cell structure is much stronger than the other flow regimes. This phenomenon can be seen by looking at the temperature field for the same condition.

The average temperature field (for the same conditions of Figure 4-12) is illustrated in Figure 4-13. The average temperature field is less deviated from a linear distribution for low g_{vib} and high f values (weak one-cell or 4-cell structure). Nevertheless, when the strength of the induced flow is increased (3-cell structure), the temperature field is highly distorted, as demonstrated in the lower left region of Figure 4-13. In this condition, the fluid flow is strong enough to induce an unsteady periodic pattern in the temperature and concentration. In other words, the steady-state condition is not achieved, as these fields are changing constantly with the same period as the external excitation.

The effects of induced convection on the temperature field can be characterized by considering the deviation of temperature from the ideal linear distribution. The distortion in the temperature field is a time-dependent process, which occurs with the same frequency as the applied excitation. The maximum deviation of temperature from the ideal case in each time step is a key parameter in presenting the level of disturbance in the system. Moreover, this value is important and can be used in image processing of the experiments since the data are provided using an optical interferometry technique. Therefore, it is important to know the level of disturbance in the system to make sure that the temperature field has reached a steady-state condition after a certain time in the experiment.

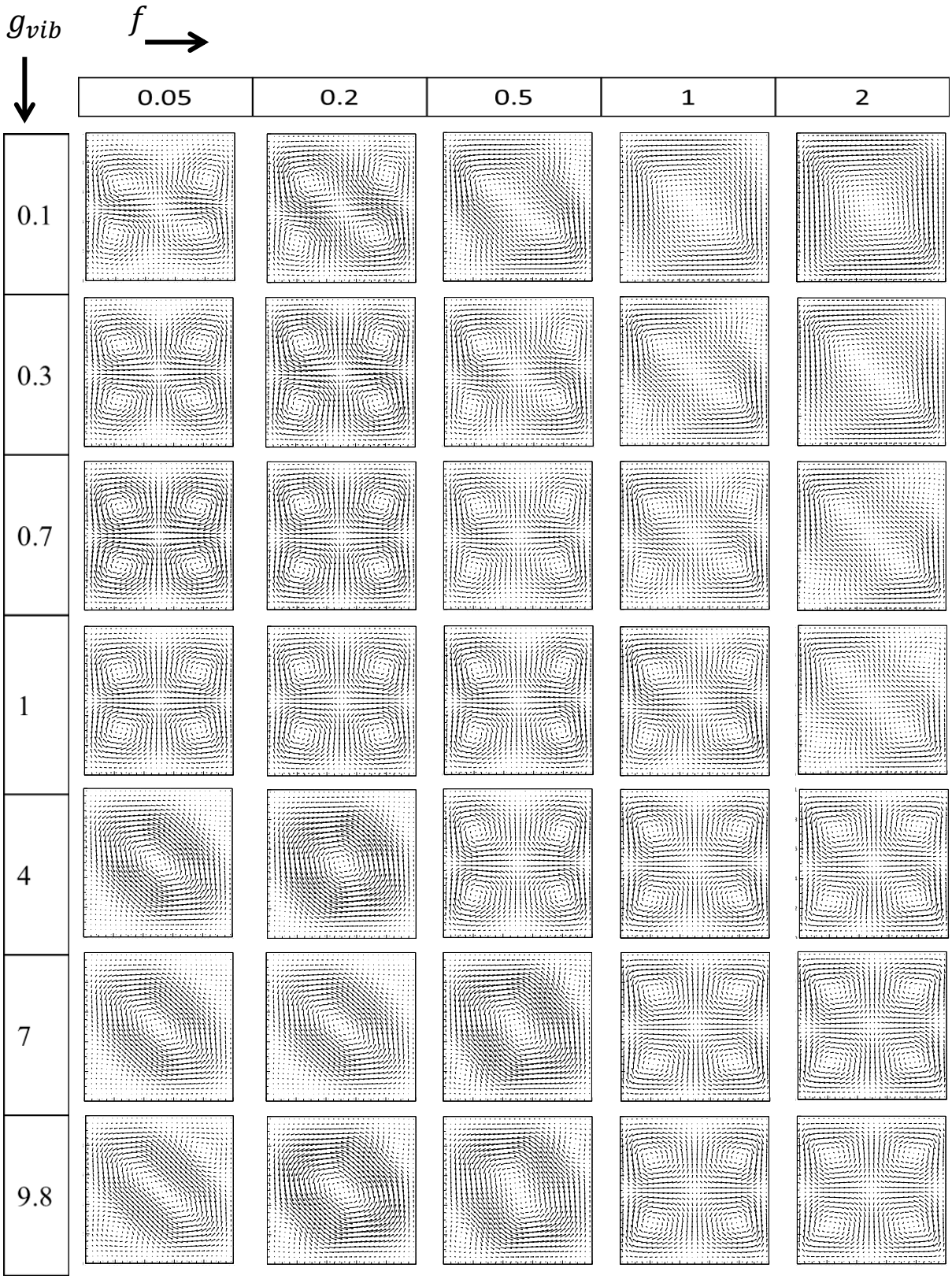

Figure 4-12: Average flow field for different excitations g_{vib} [m.s^{-2}], f [Hz]

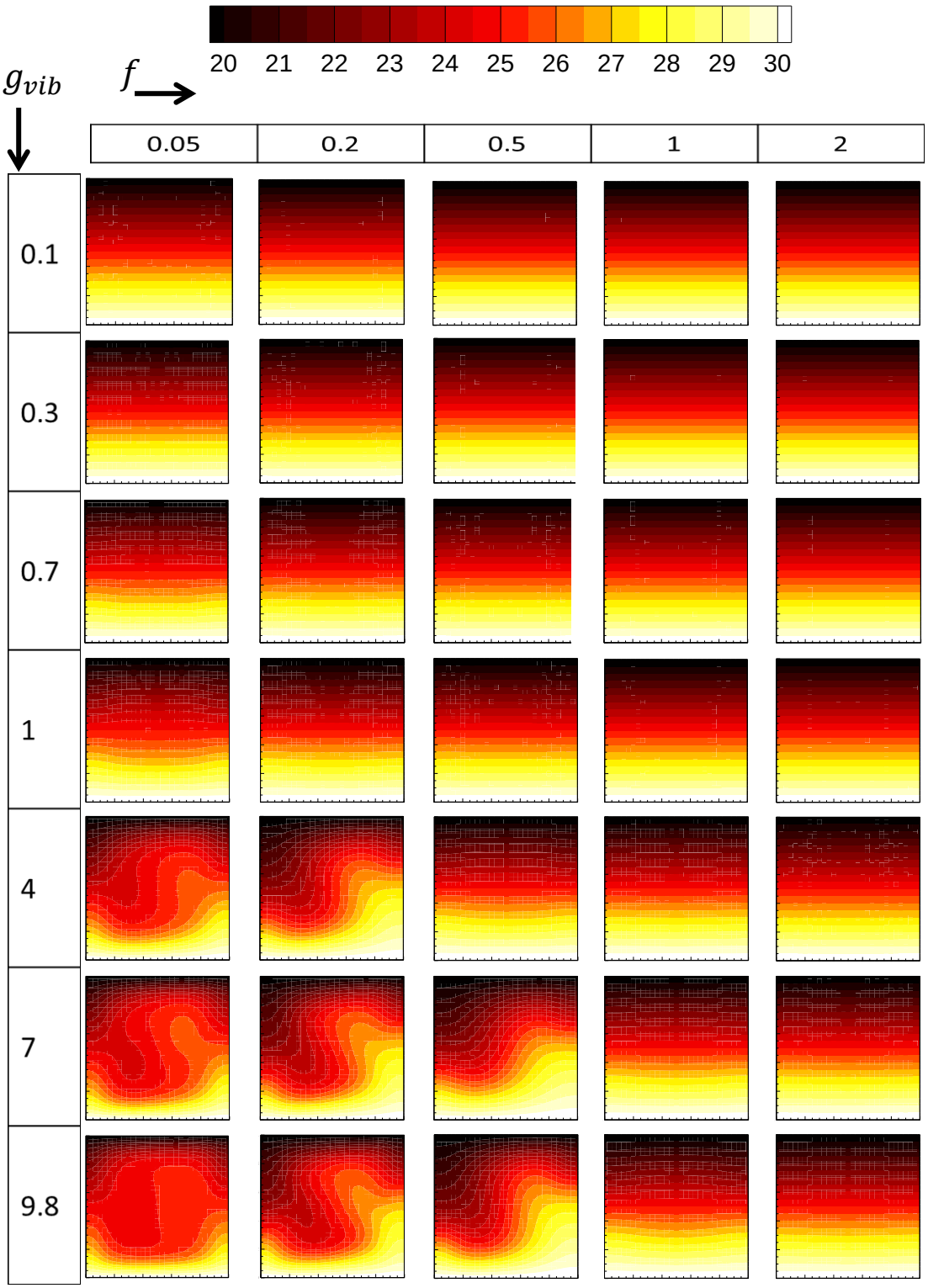

Figure 4-13: Average temperature field for different excitations, g_{vib} [m.s^{-2}], f [Hz]

The maximum deviation of temperature with respect to the ideal zero-g condition is plotted in Figure 4-14 for different excitations. As shown, the magnitude of deviation from the ideal case increases for larger g_{vib}. Moreover, for excitations with the same magnitude of vibration, the temperature field is more distorted for lower frequencies. Figure 4-14 shows that, even in the presence of a very low vibration, the temperature distribution is affected, although the deviation can be small ($\sim 10^{-3}\,K$). When the deviation becomes larger, assuming a steady-state condition for the temperature field is not valid since the field changes with the same frequency as the excitation, and the amplitude of the field change with the maximum temperature deviation.

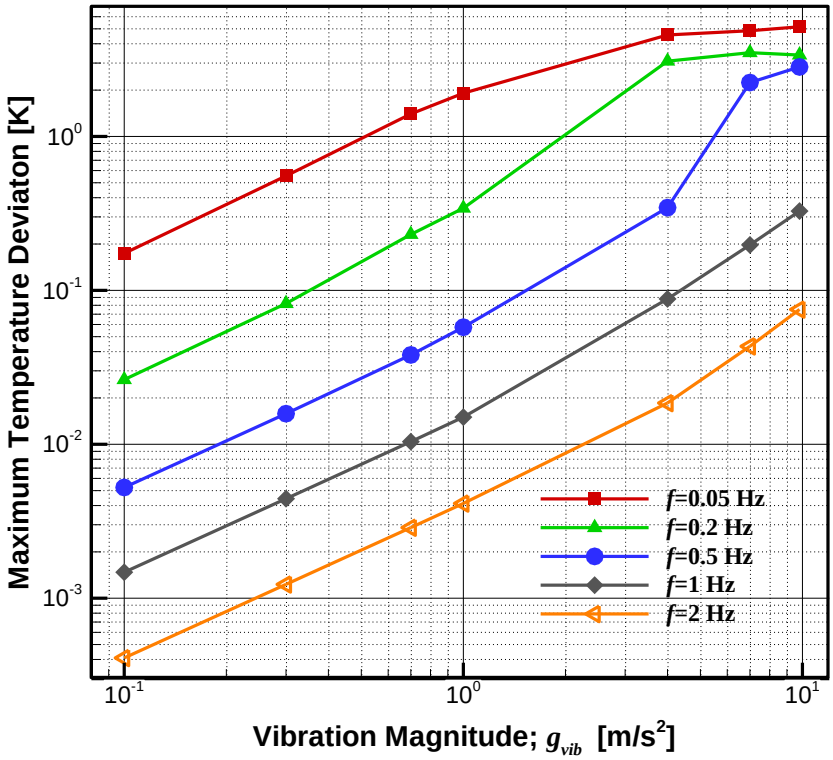

Figure 4-14: Maximum temperature deviation for different excitation cases

The Nusselt number is usually used to determine the strength of the convection. The variation of the average Nusselt number is shown in Figure 4-15 versus the Gershuni number. As shown for Gershuni numbers lower than 8×10^{-3}, the Nusselt number is relatively close to 1. Beyond this critical point, the Nusselt number increases considerably depending on the two possible average-flow regimes. When the average flow has a 3-cell structure, the increase in the Nusselt number becomes more significant, which indicates stronger flow circulation and mixing.

Yet, for the same Gershuni number but different average flow structure, i.e. 4-cell solid-line branch, the Nusselt number gradually increases for higher Gershuni numbers.

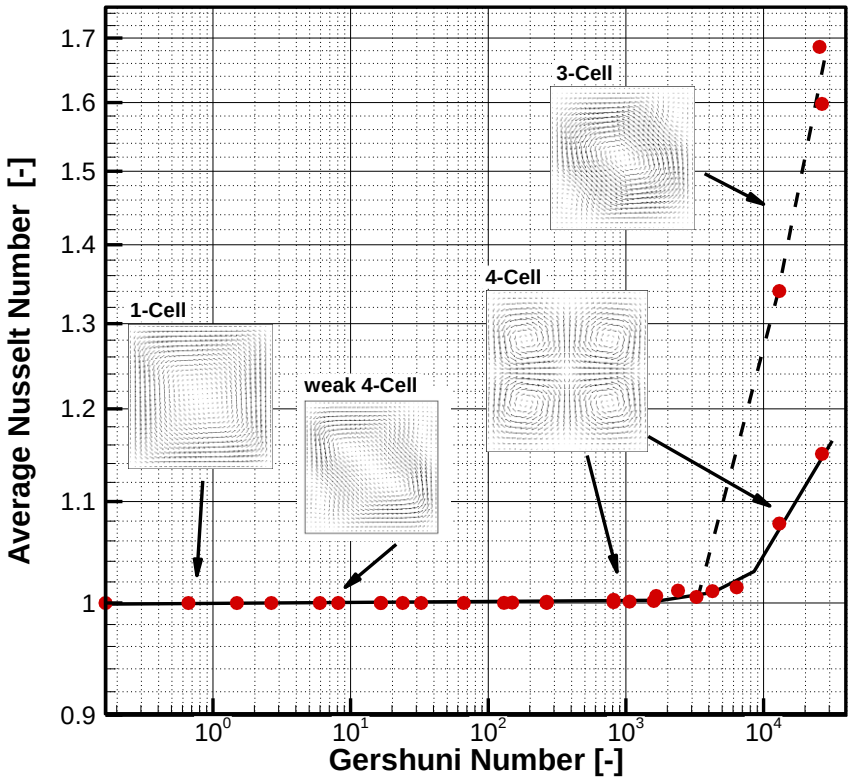

Figure 4-15: Average Nusselt number versus Gershuni number

As a result of the influence on the flow and temperature fields, the distribution of species is also affected in the presence of forced excitation. The average concentration field of water is shown in Figure 4-16 for different cases. The average value for each grid point is obtained by averaging within a period of the applied excitation right after the steady-state time (t > 13.88 hours). For relatively small amplitudes of oscillatory gravity and high frequencies (Figure 4-16-[A]), the concentration field maintains its ideal linear variation. By increasing the strength of the vibration, (Figure 4-16-[B]) distortion in the concentration field becomes observable as the diffusion challenges the convection. Distortion in the concentration field intensifies as a result of the external excitation. The mixing effect predominates for cases with low frequency and high magnitudes of vibration (Figure 4-16-[C]). In this condition, the components are almost uniformly distributed throughout the entire domain.

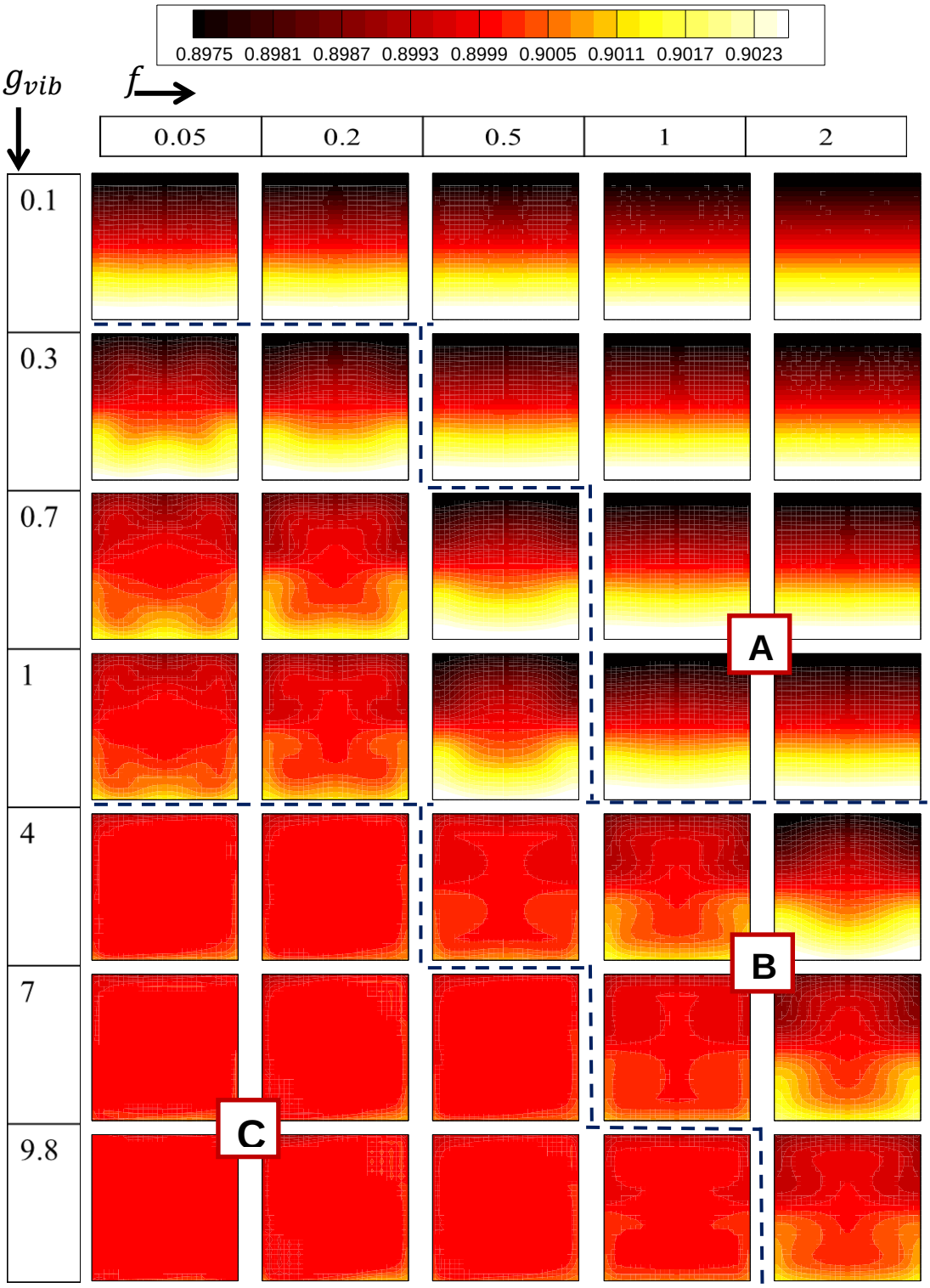

Figure 4-16: Average concentration field for different excitations, g_{vib}[m.s^{-2}], f [Hz]

The mass fraction of species is affected by applying external vibration on the experimental cell. This transient process of separation is illustrated in Figure 4-17. This figure shows the significance of vibration parameters on the quality of the thermodiffusion experiment. The separation is more restricted in the case of higher amplitude of oscillatory gravity or lower frequency. Nevertheless, for the case of $f = 1$ and $g_{vib} = 0.7\, m.s^{-2}$, the diffusion process is not affected as the trend overlaps with the ideal condition ($g_{vib} = 0$). Similar to the residual gravity field, the steady-state time decreases when the separation rate is restricted. As a result, the rate of separation can be an indication of the contribution of convection in the system.

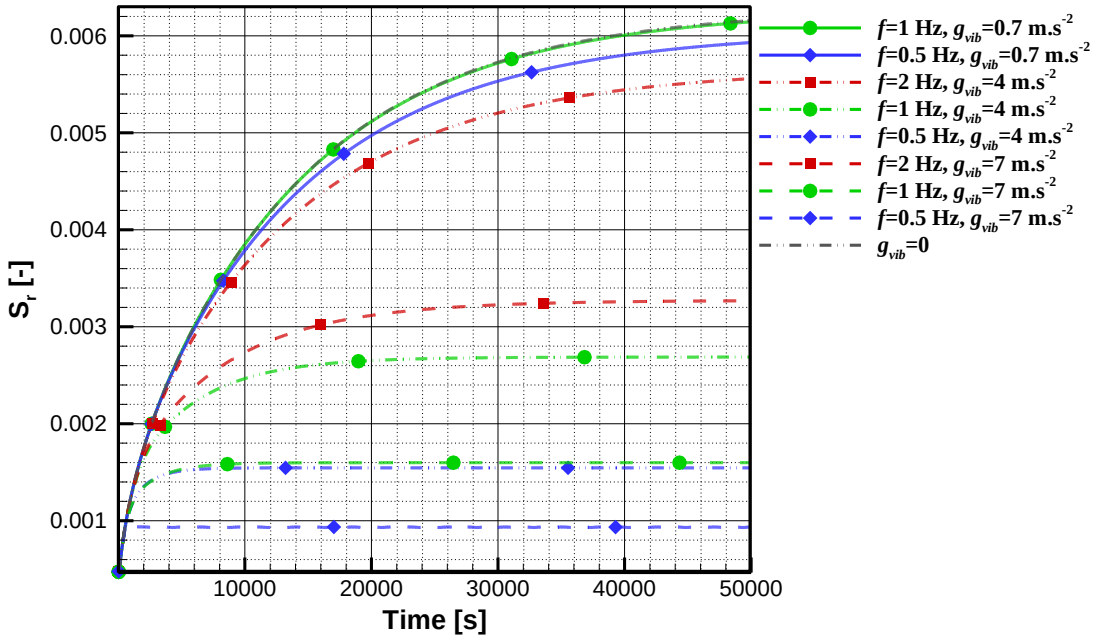

Figure 4-17: Transient separation rate in presence of oscillatory gravity field

Figure 4-18 provides a map demonstrating the deviation of the thermodiffusion experiment from the ideal condition. This figure shows the non-linear relationship between both the magnitude and frequency of the acceleration and the separation rate. Diffusion is not affected for $g_{vib} = 0.1\, m.s^{-2}$ even for low frequencies. For higher amplitudes of oscillatory gravity ($0.1 < g_{vib} < 1$ m.s^{-2}), disturbances from the vibration is diminished for higher frequencies ($f > 1$). For the case of a typical microgravity environment, the maximum magnitude of the g-jitter vibrations is on the order of $0.1\, m.s^{-2}$. Thus, it can be concluded that high-frequency vibrations (higher than 1) have no effect on the thermodiffusion experiment and can be neglected.

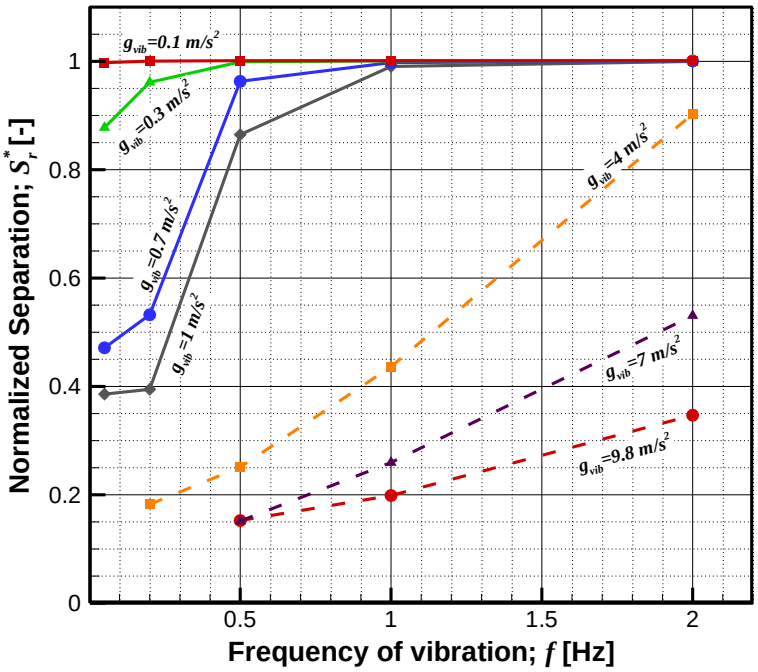

Figure 4-18: Normalized separation rate for different excitations

When plotting the normalized separation rate versus Gershuni number (vibrational Rayleigh number), one can obtain certain trends as demonstrated in Figure 4-19. However, the trends do not correspond to different average flow regimes (as is in Figure 4-15) but rather indicate low and high frequency vibrations.

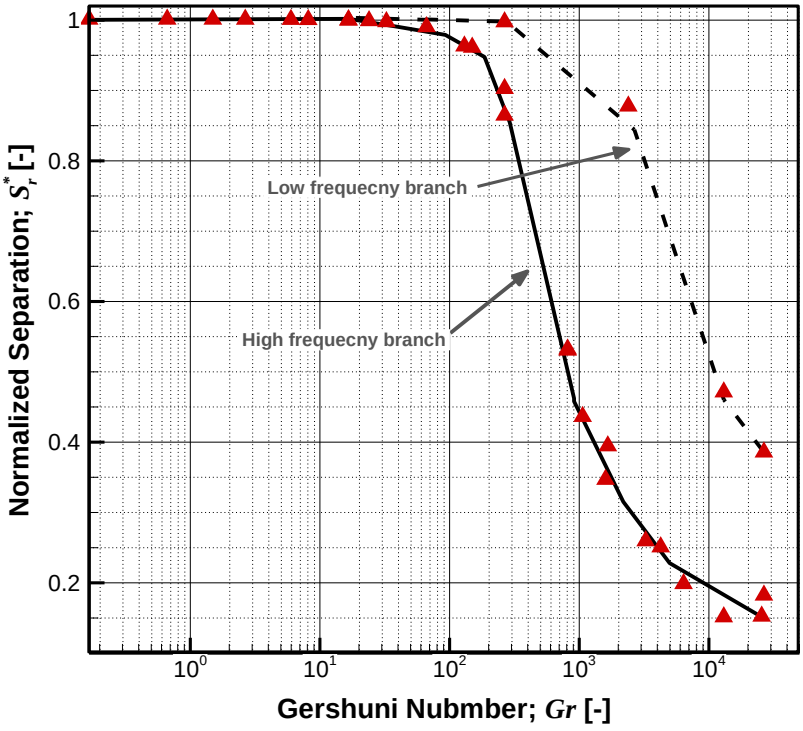

Figure 4-19: Normalized separation versus Gershuni number

This figure shows that by increasing the Gershuni number the separation decreases due to induced convection. However, depending on the frequency of the vibration different trends can be obtained. It was found that the concentration field is more affected in the case of lower frequencies. However, as this figure depicts, at the same time the Gershuni number would be relatively large. The results of this study indicate a critical value for the vibrational Rayleigh number (Gershuni number) of 20, beyond which the process is affected by the external vibration. However, for vibrational Rayleigh numbers of less than 100, more than 95% of the ideal separation can be obtained. Similar analyses can be performed for different mixtures with different diffusion and Soret coefficients.

4.5 Simulation of IVIDIL

In this section, the experimental runs of the IVIDIL project are studied numerically. To the best knowledge of the author, results of the IVIDIL forced-vibration runs have not been published yet. The numerical simulations were performed for an IPA mixture with 90% by weight of water and with a maximum temperature difference of 10°C, i.e. experimental runs 1 to 12, excluding run2 (see Table 1-1).

4.5.1 Concentration and Temperature field

The main objective of the IVIDIL project was to study the influence of controlled vibration on the diffusion process. It was shown earlier how the frequency and the amplitude of vibration influence the diffusion process. In this section, some of the significant features of the IVIDIL experiment will be presented that could be used in companion with experimental results for a better understanding of the complex double diffusion process. The transient profile of the separation process is shown in Figure 4-20.

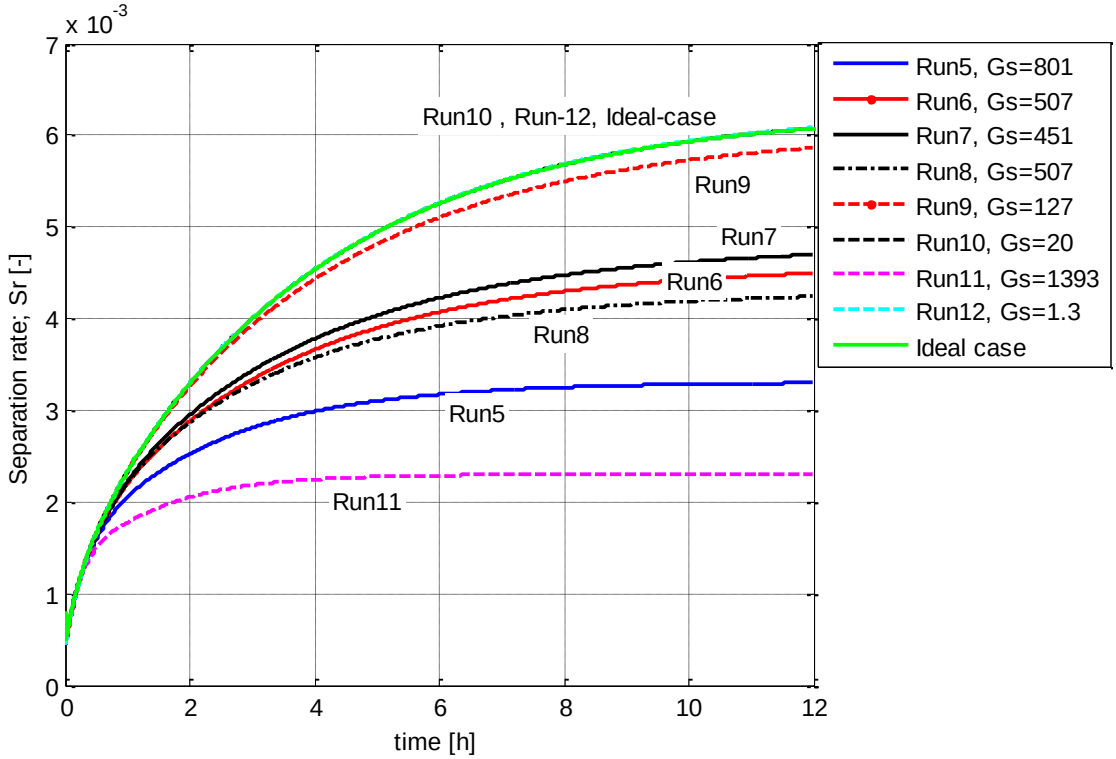

Figure 4-20: Transient separation profile of IVIDIL runs with ΔT=10°C

This figure shows the influence of forced vibration on the separation process. Generally, by increasing the Gershuni number, the separation is restricted due to the formation of stronger flow fields. The results of Run10 and Run12 are positioned extremely close to the ideal zero-gravity case. Although these two cases have the lowest frequency of vibration (See Table 1-1) no negative effect on the diffusion process observed. The reason for this is discussed earlier in the text; as shown in the previous section, low frequency vibrations are more detrimental to the amplitude of the acceleration (g_{vib}). However, in the case of a pure low-frequency vibration, an extremely large amplitude of vibration (A) is needed to cause an effect on the process.

The Gershuni number can be used as an indicating parameter; however, the process is not dependent only on this number. As shown earlier, the effect of the frequency (f) and amplitude of vibration (g_{vib}) are not the same. Nevertheless, the Gershuni number depends on the product of these two parameters. As a result, one Gershuni number could result in different outcomes.

This issue was tested in the IVIDIL project, as both Run6 and Run8 have the same Gershuni number but different vibration parameters. As shown in Figure 4-20, the transient separation profiles of these two runs are different, and more separation is achieved in case of run6.

The results of the IVIDIL runs for ΔT = 5°C are illustrated in Figure 4-21. The transient profile of the separation for all of these cases is close to the ideal condition. The Gershuni numbers for these runs are small (Gs <= 65).

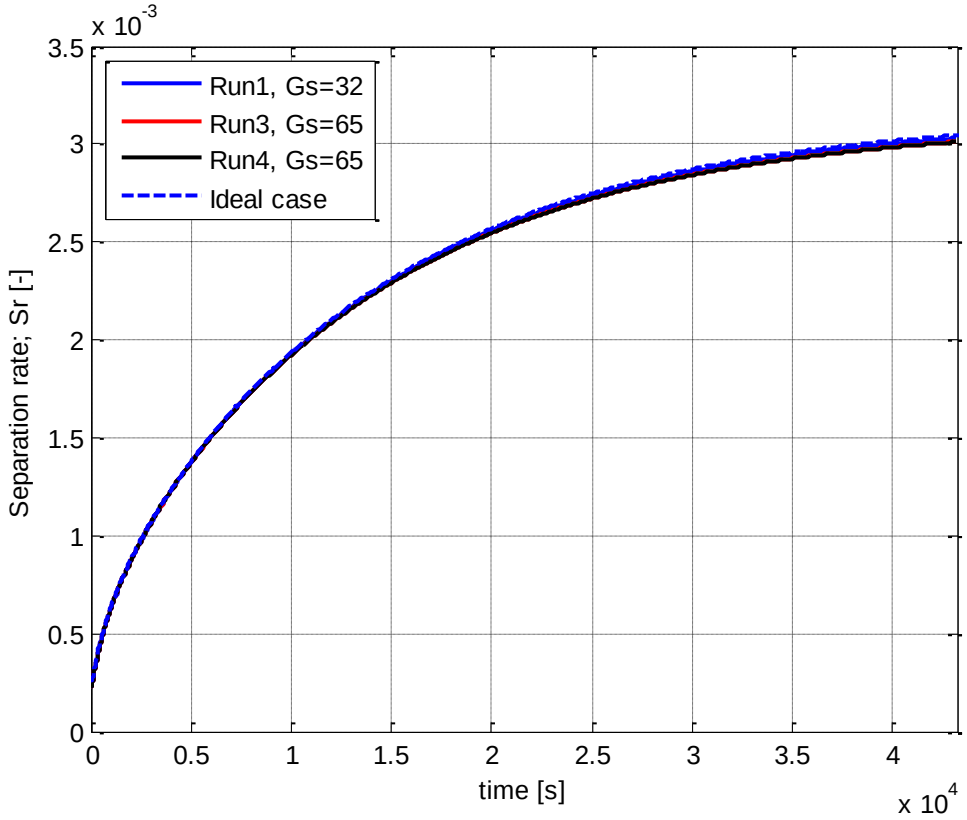

Figure 4-21: Transient separation profile of IVIDIL runs with ΔT=5°C

The critical Gershuni number that was proposed in the previous chapter can be extended to the scope of IVIDIL. The values of separation rate are normalized with respect to the ideal conditions for each run and are listed in Table 4-3. The runs are sorted from left to right according to the value of the Gershuni number. As shown, the effect of vibration is negligible up to Run9 (Gr~100) in which 95% of the separation of the zero-gravity condition is achieved. Further increase in the Gershuni number seriously affects the diffusion process as induced convection dominates the diffusion process.

In the same table, the maximum value of temperature deviation with respect to the ideal linear profile is included. This value shows how much the temperature field is affected by the induced flow. This value is important in the image processing of experimental data. In order to decouple the effects of the variation of temperature and concentration on the density (refractive index), it is assumed that the temperature field reaches a steady-state condition soon (compared to the diffusion time) after the start of the experiment. However, in the case of external vibration, the temperature field is affected. The numerical results show that within the scope of te IVIDIL project, the applied excitations are not strong enough to cause a considerable disturbance in the temperature field. Although, for image processing, a more precise investigation should be performed by considering the maximum temperature deviation and the contrast factors, which are the changes of the refractive index due to the temperature or concentration of the mixture.

Run#	12	10	1	3	4	9	7	6	8	5	11
Gershuni number [Gr]	1.3	20	32	65	65	127	451	507	507	801	1393
Normalized Separation Rate [Sr*]	0.99	0.99	0.98	0.98	0.98	0.95	0.76	0.73	0.69	0.54	0.37
Maximum Temperature Deviation x 10^{-2} [K]	1.41	3.56	1.11	0.51	0.90	4.49	3.09	2.64	5.58	4.56	6.88

Table 4-3: Normalized separation rate for IVIDIL runs

A linear distribution of concentration in the cell is an indication of a purely diffusive process. When convection occurs, this linear pattern is disturbed. The variation of the water concentration on the centre line of the cavity is illustrated in Figure 4-22 at $t = 12h$.

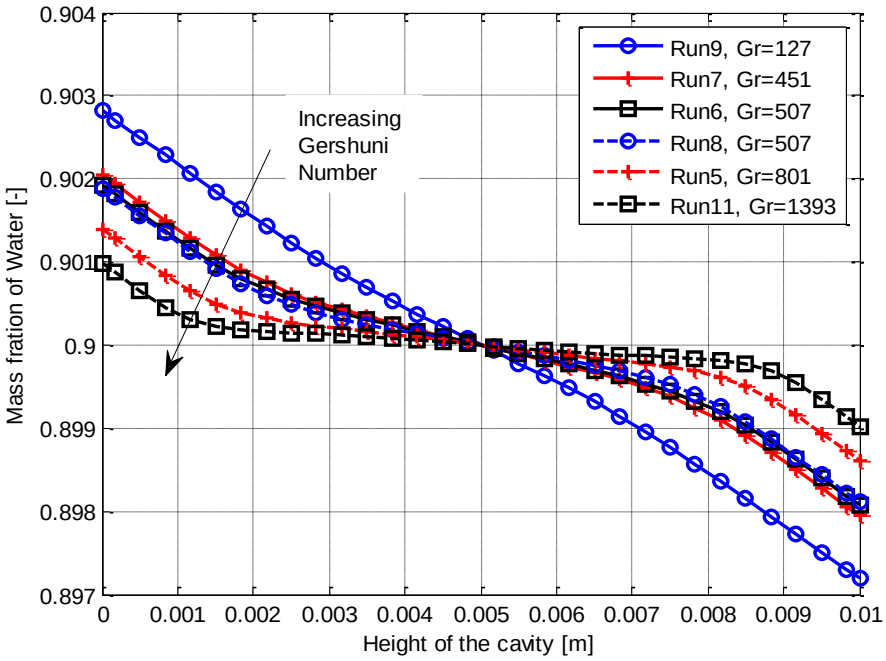

Figure 4-22: variation of concentration of water between the walls (t=12h)

By increasing the Gershuni number, the linear profile of concentration is affected by the induced vibration. Mixing becomes dominant in the cell as the variation of concentration become insignificant in the central region. For example, for Run11, about 60% of the cell has the same concentration. The separation process is dominant only near the wall where the velocities are small due to the no-slip boundary condition enforced. Run9 demonstrates an almost linear profile in which 95% of the separation of the ideal case is achieved. The variation of water mass fraction for other runs (with lower Gershuni numbers) is linear and not plotted here.

The concentration field for four sample runs are shown in Figure 4-23. These fields are obtained after 12 hours of the start of the simulations. The average velocity field is also calculated for a period of vibration and the average vectors are plotted in the same figure. For all of the presented runs, the average flow is in the 4-cell symmetric regime. This regime can affect the concentration field, but it has negligible influence on the temperature distribution. By increasing the Gershuni number (in Figure 4-23), the strength of the average flow increases and the distortion in the concentration field becomes more intense.

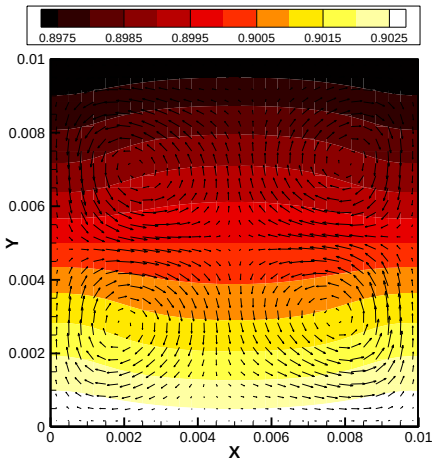

(a) Run 9, f= 0.5Hz, A=70 mm, Gs=127

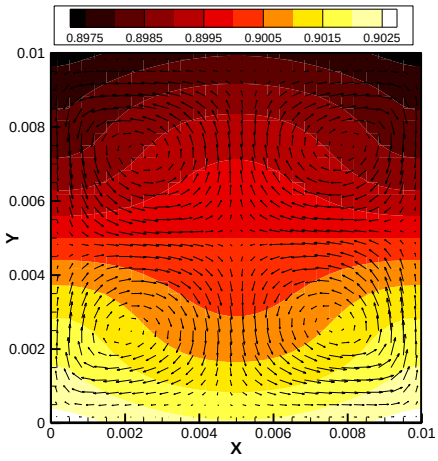

(b) Run 7, f= 2Hz, A=33 mm, Gs=451

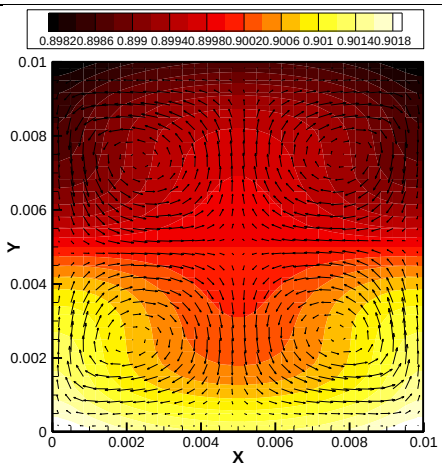

(c) Run 5, f=2Hz, A=44 mm, Gs=801

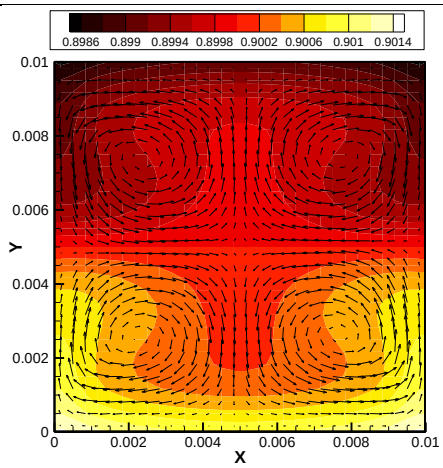

(d) Run 11, f=2 Hz, A=58 mm, Gs=1393

Figure 4-23: Average velocity and concentration fields for IVIDIL runs (t=12h)

The transient behaviour of the separation rate is controlled by convection. In the case of no convection (pure diffusion), separation occurs near the heated walls as a result of the Soret effect. The separated components diffuse through the system. This process is slow and is on the order of the diffusion time. However, when convection is introduced into the system, the transport of species accelerates. In this condition, the system reaches steady state in a shorter time. Figure 4-23 illustrates the transient separation process in which the contours of water mass fraction are plotted for Run5.

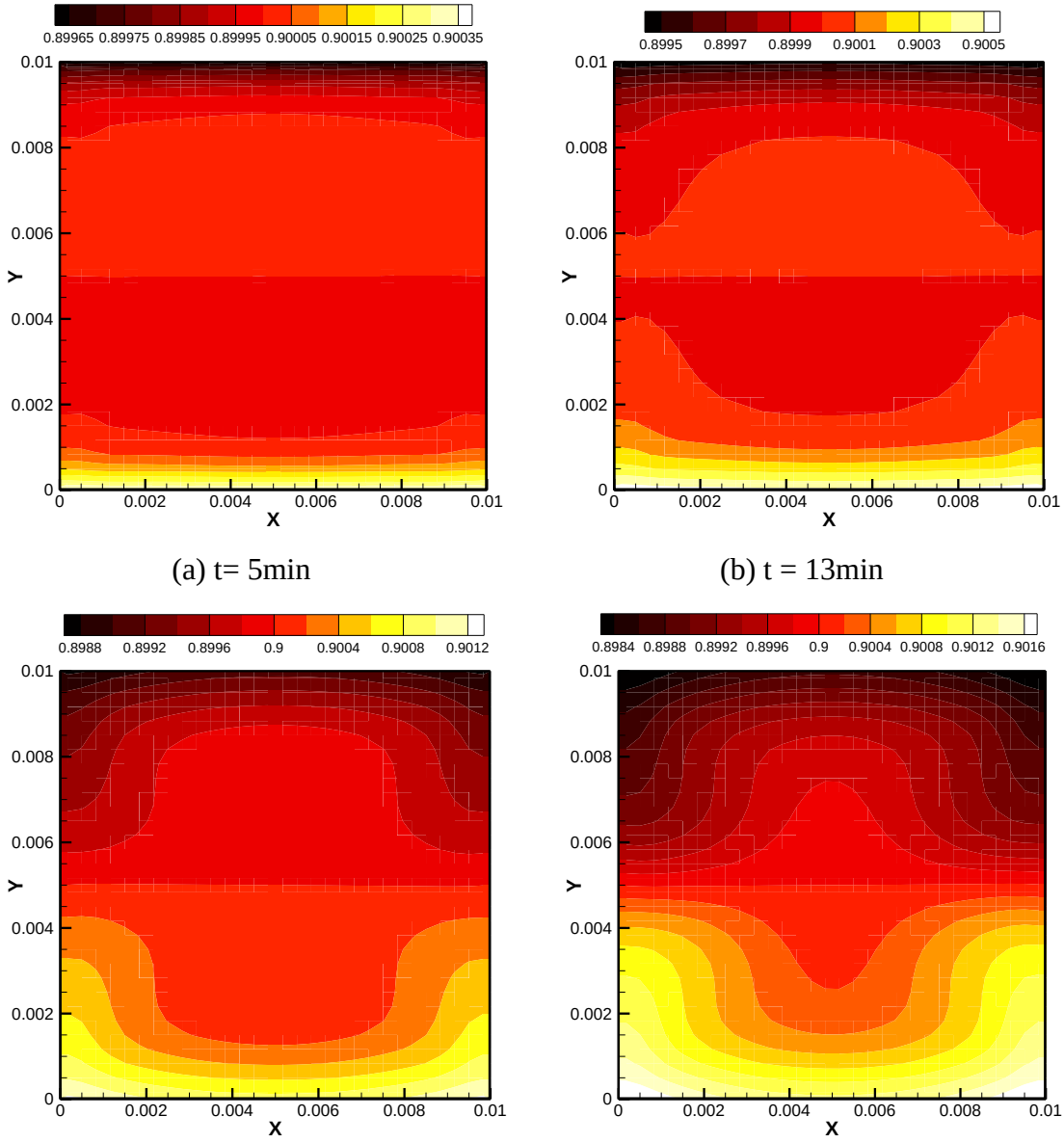

(a) t= 5min (b) t = 13min

(c) t= 1 hour (d) t= 4 hour

Figure 4-24: Development of separation inside the cell for Run5

The role of convection in governing the concentration field is evident from the beginning of the simulation (Figure 4-23-(a,b)). Only after 4 hours does the system reach the steady-state condition, as shown by comparing this image (Figure 4-23-(d)) with that of the solution at t = 12 hours (Figure 4-23-(c)).

4.6 Influence of microgravity environment

The suitability of the microgravity environment for fluid experiments has been a controversial issue. As discussed in Chapter1, many researchers have studied different aspects of the problem. The IVIDIL experiment has the capability to provide intensive information on this subject. Nevertheless, extensive investigation of the experimental results has not yet been published. In the recent publications [39], it was concluded that the damaging role of g-jitter is not major.

Figure 4-25 illustrates the results of image processing of IVIDIL-Run2 (without forced vibration) adapted from reference [40]. In the same figure, the numerical results of the ideal pure weightlessness condition are plotted. Good agreement is obtained between the experimental results and the ideal solution. This indicates that the diffusion process is likely not affected by any induced flow. In addition to the value of the separation rate at the steady-state condition, which is close to the ideal case, the trend of the separation rate also verifies this conclusion. The separation is still in progress after 12 hours where the steady-state condition has not yet been reached.

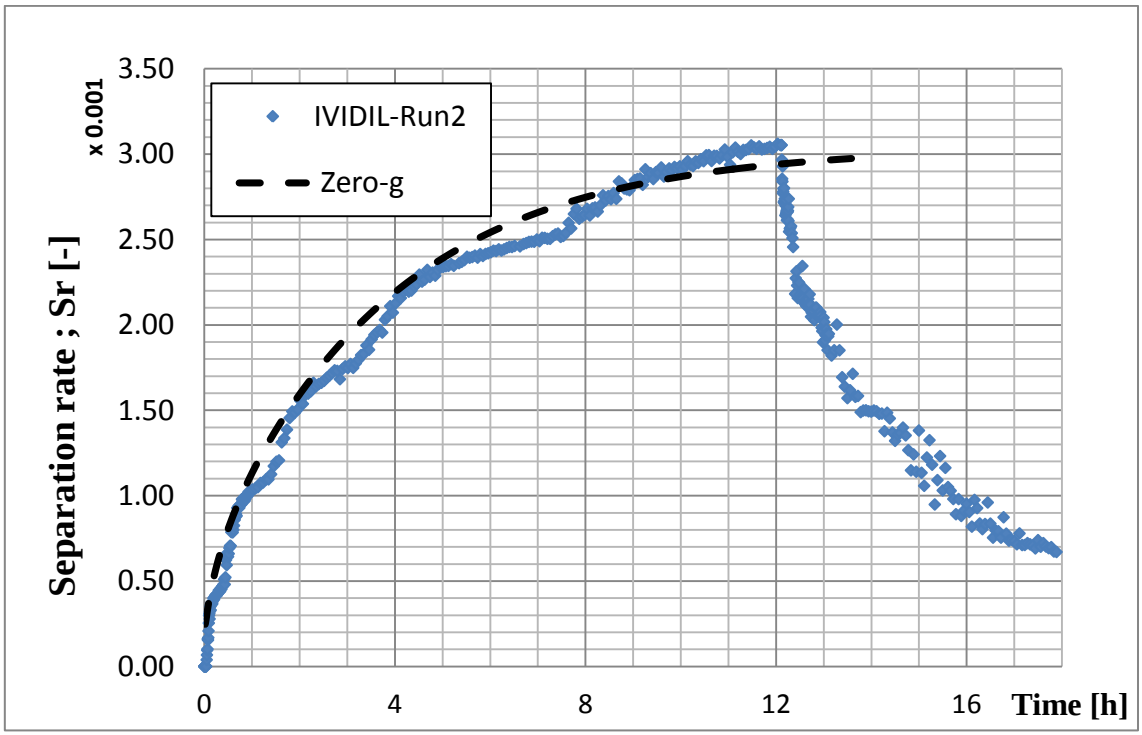

Figure 4-25: Separation profile of IVIDIL-Run2 [40] and numerical results

As shown in the same figure, in the IVIDIL experiments the separation ceases at t = 12h when the temperature gradient is removed in order to survey the pure diffusion process for the next 6 hours.

At the beginning of the current work, the experimental results had not been published and the effect of g-jitter was a rather serious question. In this section, we will survey the effects of g-jitter by the presentation of different methodologies.

Although it has now been found that the effect of g-jitter during the normal performance of the ISS is minimal; however, in the profile of the separation some local fluctuations are noticeable. For instance, in Figure 4-25, a rather large deviation is observable starting at t = 5h, which lasts for the next 3 hours. Smaller fluctuations are also visible at t = 1 h and t = 2 h. One possible explanation of these small fluctuations is that the source of these deviations is the prevailing micro-acceleration onboard the ISS. The aim of this study is to check if such small variations can be detected using numerical tools. It can be added here that in other, similar numerical studies [61], it was found that the effect of g-jitter has been significant when RMS values of the raw data were employed.

In this section we will survey the effects of g-jitter by considering different acceleration data. But we will start with the quasi-steady accelerations prevailing on the International Space Station.

4.6.1 Quasi-steady (residual) acceleration

The quasi-steady acceleration on board the ISS is measured by the MAMS probe. The acceleration data for the period of IVIDIL-run2 is illustrated in Figure 4-26.

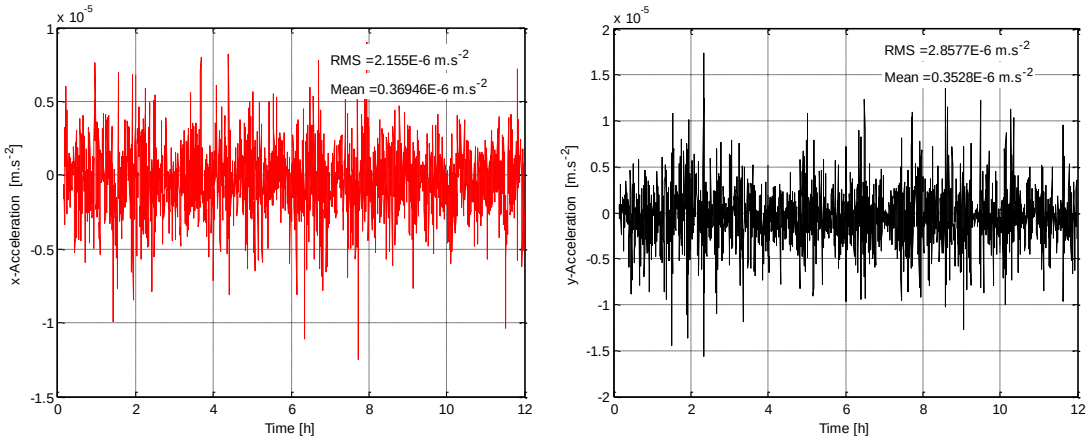

Figure 4-26: Quasi-steady accelerations measured during IVIDIL-Run2

The magnitude of the quasi-steady acceleration are fairly small (compared to g-jitter); however, the average of these accelerations is not zero and is in fact on the order of μg_0. The simulations were performed using MAMS accelerations data. In addition, a supplemental case was also simulated in which the raw data were multiplied by a factor of 10.

A scaling factor C is defined that is 10 for the described supplemental case and 1 for the raw-data case. The scaling factor is defined for a few reasons. First, the accelerometers are positioned with a certain distance to the experimental cell. Thus, there is a possibility that the recorded accelerations may not be those that are sensed by the experimental cell due to structural damping. Second, we would like to intensify the effects of accelerations in order to check the sensitivity of the system against the microgravity condition.

The maximum induced velocity is illustrated in Figure 4-27 for the case of quasi-steady micro-accelerations. As shown, the magnitude of the induced velocities is small, on the order of 10^{-8} for the case of the real MAMS data. When the accelerations are multiplied by 10, the magnitude of the induced velocity is increased approximately by the same order. However, still the induced velocity is still not strong enough to further affect the process.

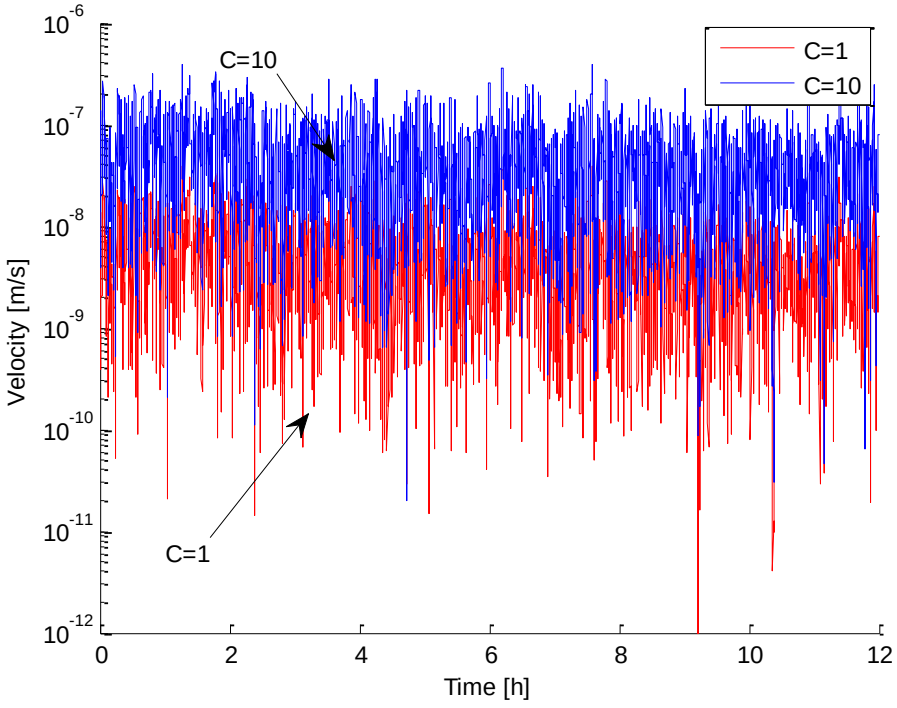

Figure 4-27: Maximum induced velocity in the cell in case for quasi-steady accelerations

The separation process is not affected by the induced convection due to the quasi-steady accelerations on board the ISS. This fact is shown in Figure 4-28, in which the transient separation process is depicted. The separation trend is close to the case of the ideal zero gravity condition. Even when the accelerations are considered to be 10 times larger, no deviation in the diffusion process is observed.

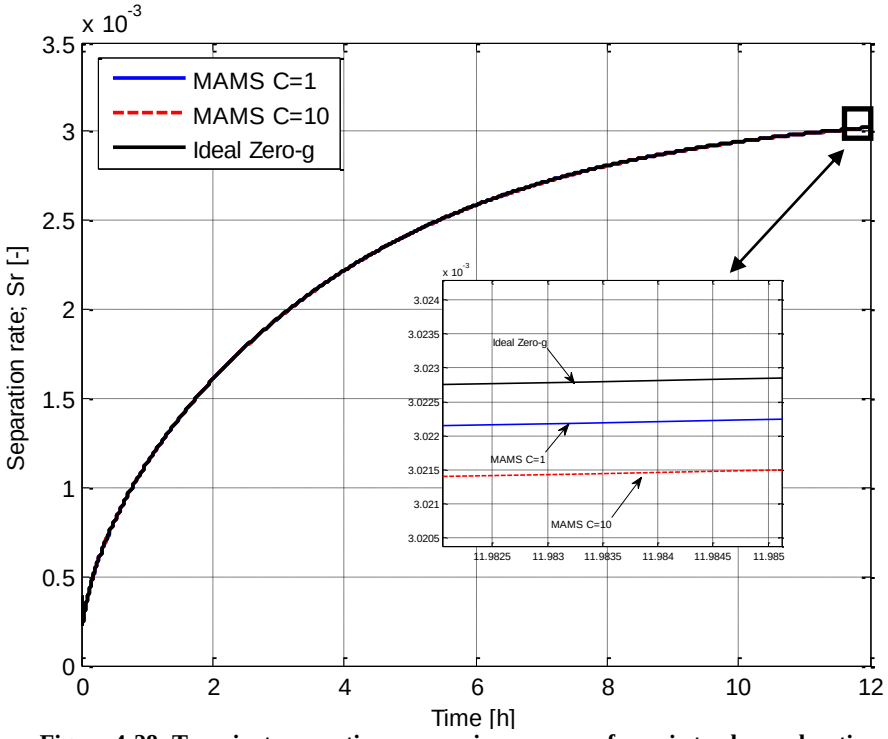

Figure 4-28: Transient separation process in presence of quasi-steady acceleration

The results show that thermodiffusion process is not affected by the prevailing quasi-steady accelerations on board the ISS. Fundamentally, these micro-accelerations are too weak to cause an effect on the diffusion process.

Accordingly, the temperature and concentration fields are close to the ideal case (linear distribution). Thus, no further discussion is provided for the effects of the quasi-steady (residual) acceleration of the ISS on the flow characteristics.

4.6.2 Vibratory full-range g-jitter

Simulations are performed using the acceleration data of SAMS-es08 (for the duration of Run2). In Figure 4-29, the generated acceleration data for the CFD code is plotted. This figure shows the results of different methods used for data extraction. The Max/Min method is shown in black, RMS-AVE, RMS and Average method are shown in red, blue, and green, respectively.

As shown in Figure 4-29, the magnitudes of accelerations are larger for the Max/Min method and smaller for the Average method. The RMS values are positive while the RMS-AVE method resulted in both negative and positive values (positive values are covered by the RMS method). The same plot for y-axis accelerations is shown in Figure 4-30. In these figures, the variation of accelerations is almost in a constant range for all of these methods, indicating a periodic high-frequency regime. Therefore, in some points high peaks are observable that are identified as pulse-like accelerations. These spikes may affect the experiment.

Simulations were performed for Run2 to compare the results of different interval methods. The transient separation process is illustrated in Figure 4-31. The results are packed together and are coherent with respect to the ideal zero-g case, except for the case corresponding to the RMS method. It is shown that when the RMS method is used, separation is significantly limited (by about 0.3). This shows the significance of using the proper model to extract the data. In the RMS method, all of the data have the same sign (positive). Therefore, the vibratory nature of the g-jitter is overlooked and the system behaves similar to the case of the residual gravity condition.

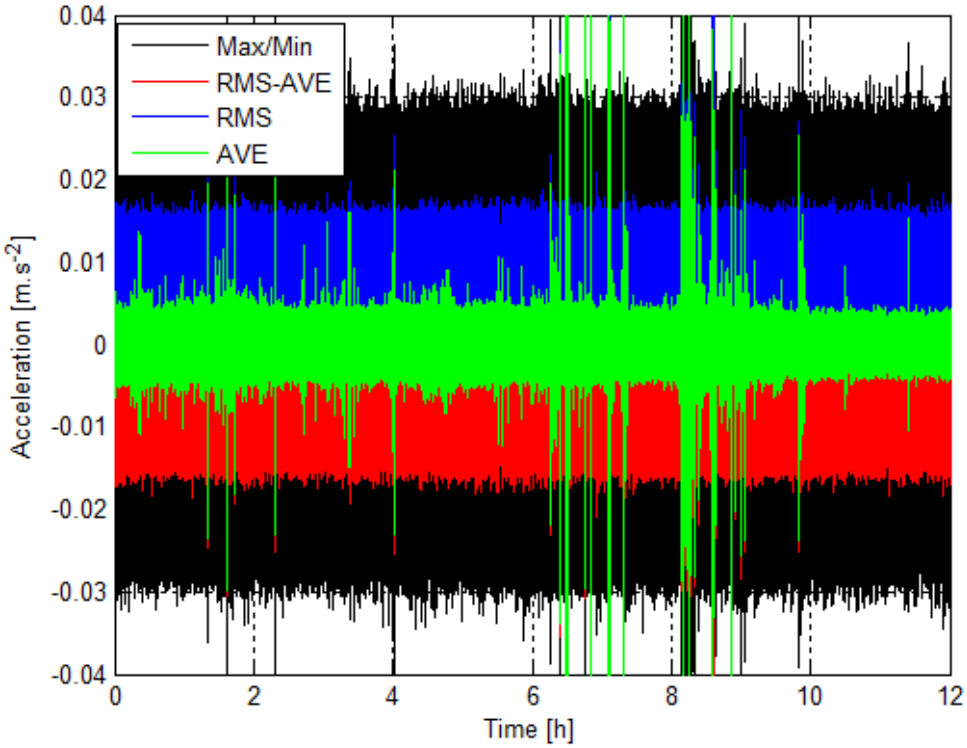

Figure 4-29: X- acceleration (Run2) generated for CFD analysis [Color]

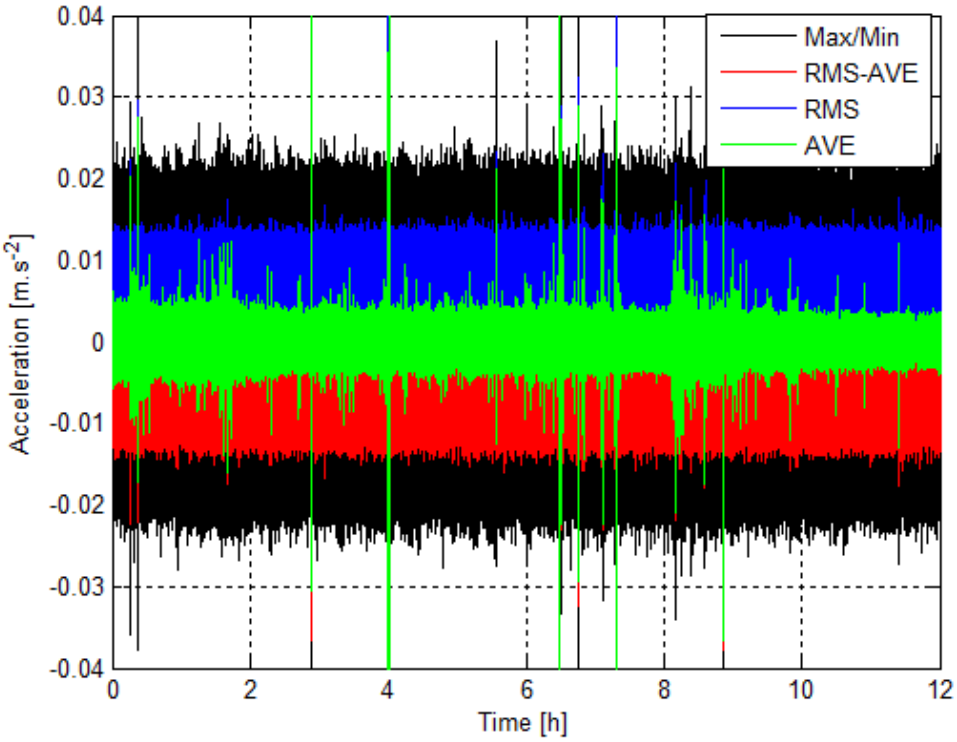

Figure 4-30: Y- acceleration (Run2) generated for CFD analysis [Color]

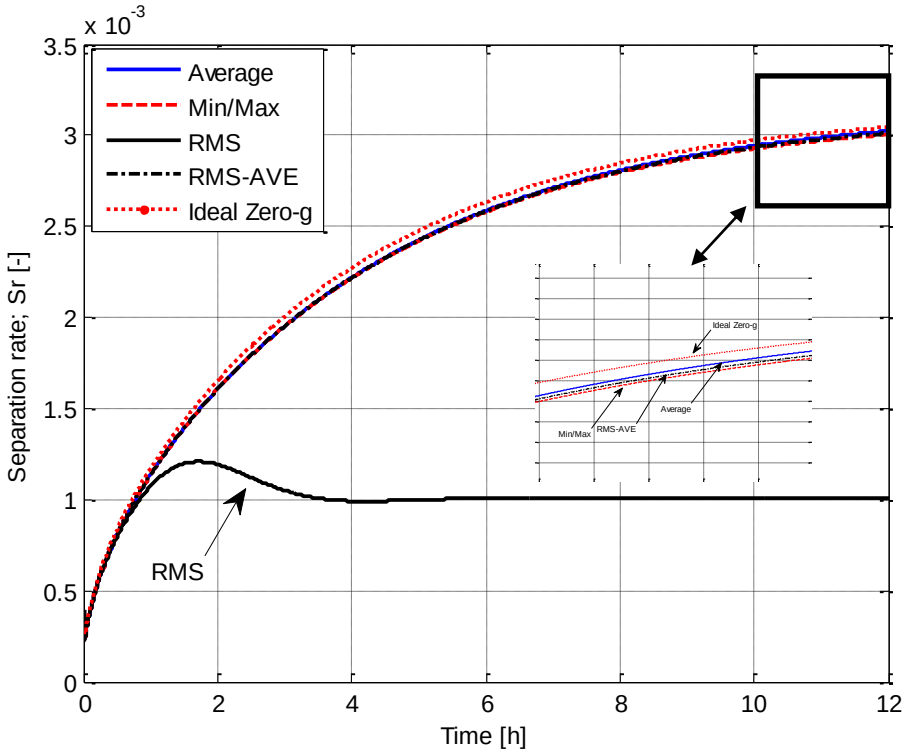

Figure 4-31: Transient separation process (Run2) in presence of vibratory g-jitter

Furthermore, Figure 4-31 shows that in the simulation of g-jitter the most important parameter is the sign change of the acceleration, rather than its magnitude. The amplitude of the acceleration varies between the Average, RMS-AVE, and Min/Max methods. Therefore, their results are in near agreement, which show the low dependence of the system on the amplitude of g-jitter (in the range of scope).

When the accelerations are all positive or negative, the induced flow inside the cell has a clockwise or counterclockwise direction, respectively. The change of the magnitude of the acceleration does not seriously affect the induced convection, and, in fact, its strength remains relatively constant. This phenomenon is shown in Figure 4-31, where the x-component velocity of a typical point (P[0.005, 0.0012]) close to the hot wall is plotted for different interval methods. This point is located in the high-velocity region and roughly exhibits the maximum value of the induced velocity.

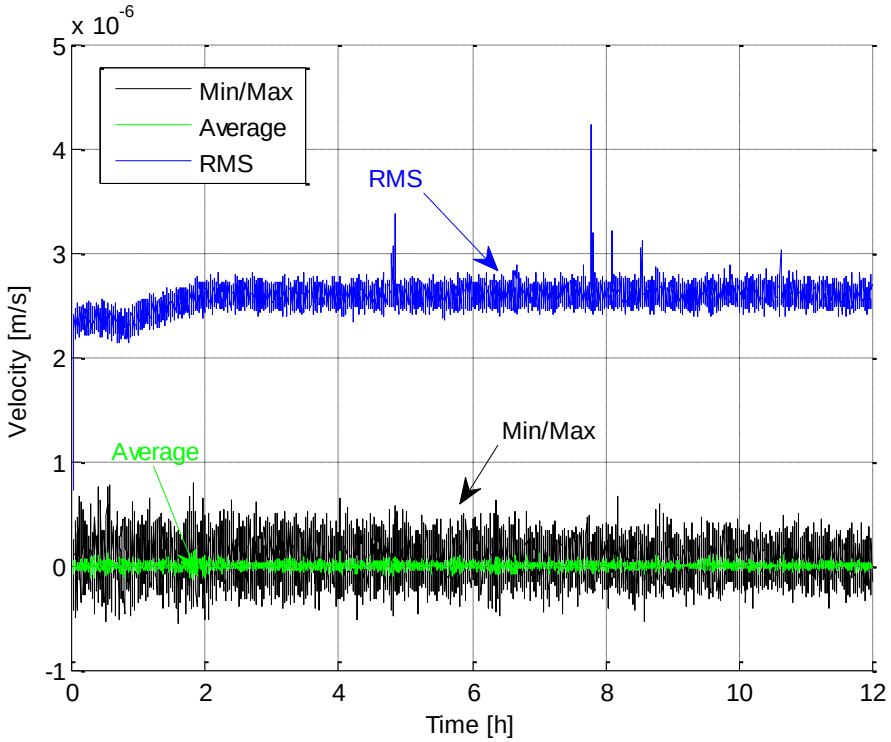

Figure 4-32: X-component velocity of a point close to the hot wall for different methods of applying g-jitter

As seen for the case of the Max/Min or Average methods, the magnitude of velocity is fairly small compared to the RMS case, by at least one order of magnitude. The reason is due to the direction of the secondary flow changing constantly with the sign change of the accelerations. Thus, there is not enough time for the velocity vectors to evolve. As a result their magnitude is much smaller. The obtained velocities for the RMS-AVE case are omitted in this figure since the values were fairly close to the Max/Min method.

The magnitude of the velocity for the RMS case is relatively constant throughout the simulations and is less affected by the fluctuations of the applied acceleration. In this case one convection cell that preserves its direction for the whole time is formed in the domain.

A linear distribution of components is expected as a result of the Soret effect in a pure weightlessness condition. Figure 4-33 illustrates the mass fraction of water between the heated walls inside the cell. The variations are almost the same for the methods that consider the sign change in the acceleration data (Interval Average, RMS-AVE and Min/Max).

Linear distribution of concentration inside the cell is obtained for the methods that are almost identical to the ideal zero-g case. The variation of concentration inside the cell for the case of the interval RMS method, displays a considerable role of buoyancy force inside the cell. The mixing effect is noticeable in the central region of the cavity.

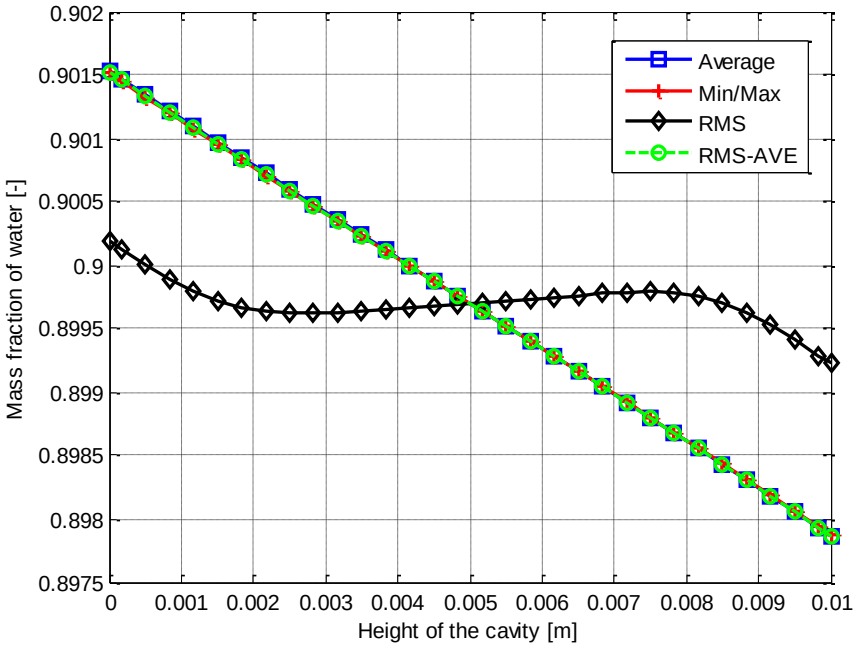

Figure 4-33: Variation of mass fraction of water on between the heated walls

The variation of mass fraction of the water component on the hot wall is illustrated in Figure 4-34. The case of the Average method is much closer to the ideal case as the variation of mass fraction is almost constant along the length of the wall. The Max/Min and RMS-AVE methods are also close to the ideal case, but the effect of convection is also discernable. As expected, the RMS results differ largely from the other three methods. The separation of water is much restricted in this case and the curve-like distribution of the water on the hot wall is an indication of strong convection in the cell, which is inconsistent with the experimental observations.

The influence of g-jitter on the temperature field is also surveyed. The variation of temperature along the height of the cell (on the middle line) is illustrated in Figure 4-35 at a time equal to 12 hours. Linear variation for temperature is obtained for all of the cases. The flow is highly disturbed when the RMS method is used; however, the induced convection is not strong enough to cause fluctuations in the temperature field.

This is good news for the researchers working on the image processing of the IVIDIL project. The result of this study shows that the temperature field reaches steady state after few minutes and remains unchanged during the rest of the experiment. Thus, the variation of the refractive index after the thermal time is only due to the concentration difference.

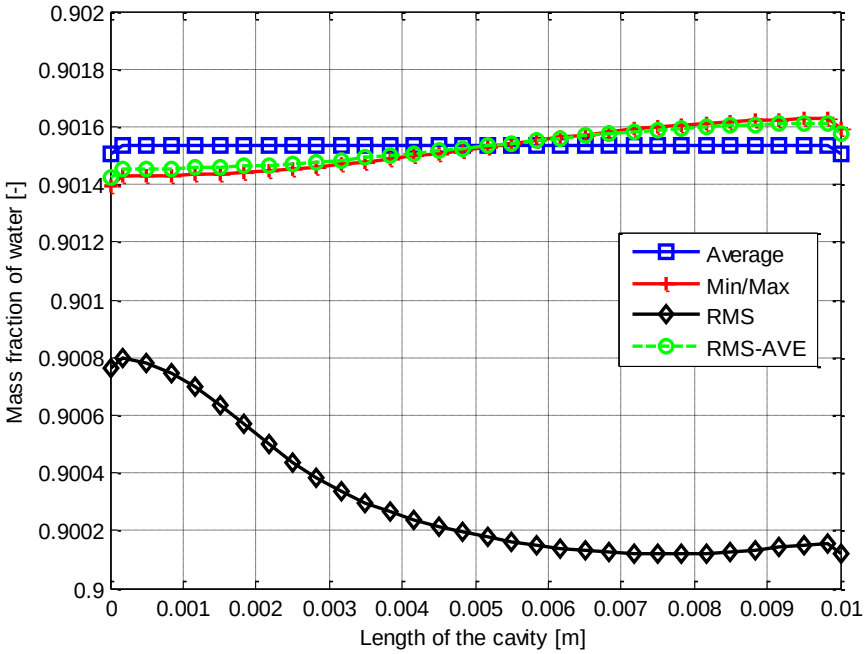

Figure 4-34: Variation of mass fraction of water on the hot wall

The summary of different methodologies for extracting the acceleration data from the raw g-jitter data is included in Table 4-4. In this table, the characteristics of induced velocities are compared for different interval methods. The statistics of the velocity fields including the maxima, means, and rms values are calculated for the whole duration of the simulations (12 h). The normalized separation rate is also obtained for each case at t = 12h. Both RMS-AVE and Max/Min methods resulted in identical outcomes for both the velocity and the separation rate. For the case of the Average method, the obtained velocities are smaller than the other methods; thus, its effect on the separation rate is insignificant. For the case of the RMS method, the obtained velocities are at least one order of magnitude larger than the other methods. As discussed previously, higher velocities, in addition to the stable velocity field (due to the same sign of applied accelerations), resulted in a small separation rate (0.33 of the ideal case).

Therefore, it is concluded that the interval RMS method is not suitable for study of g-jitter for CFD simulations.

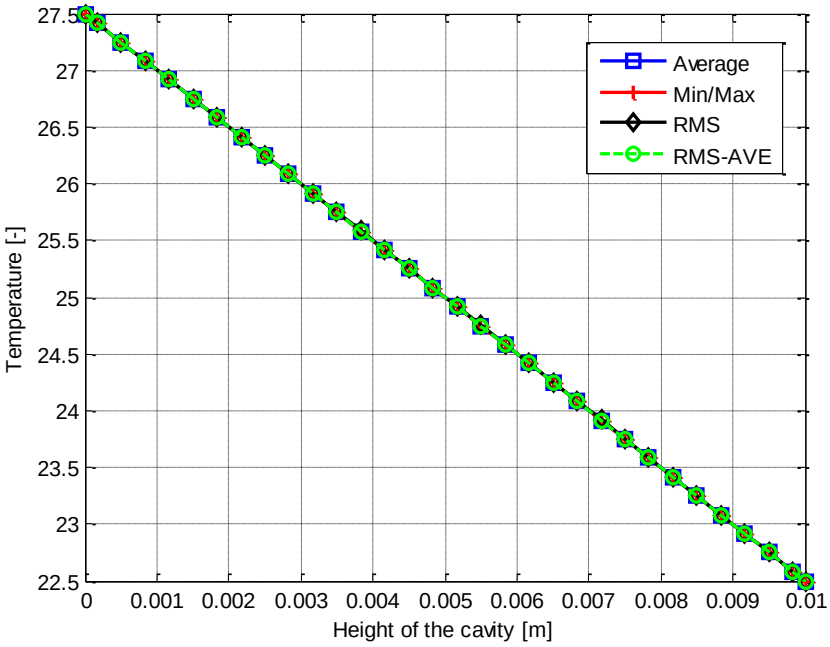

Figure 4-35: Temperature in the middle-line of the cell in presence of g-jitter

Parameter		***Interval Method***			
		Average	RMS-AVE	Max/Min	RMS
Induced Velocity	Maximum	2.05E-08	1.09E-07	1.62E-07	2.96E-06
	Mean value	9.99E-09	5.43E-08	8.06E-08	1.53E-06
	RMS value	1.19E-08	6.44E-08	9.56E-08	1.82E-06
Mass fraction	Sr^*	0.992	0.989	0.987	0.332

Table 4-4: Results of different acceleration calculation methodologies

The outcomes of the simulations are practically the same when any of the appropriate interval methods (excluding RMS) are used. However, the fluctuations in the transient profile of the separation have not been observed when the full-range of g-jitter data is used.

More simulations have been performed to investigate the sensitivity of the system to g-jitter vibrations. We have considered scaling factors to intensify the effects of g-jitter. For case of full-range g-jitter, scaling factors of C = 10 and 100 were considered for the Max/Min interval method.

The simulations were conducted for the first 8 hours of the experiment. The variation of the maximum induced velocity in the system is shown in Figure 4-36. As shown, the magnitude of the induced velocity is increased when larger scaling factors are used. As the induced velocities become larger, their effects on the thermodiffusion are more pronounced.

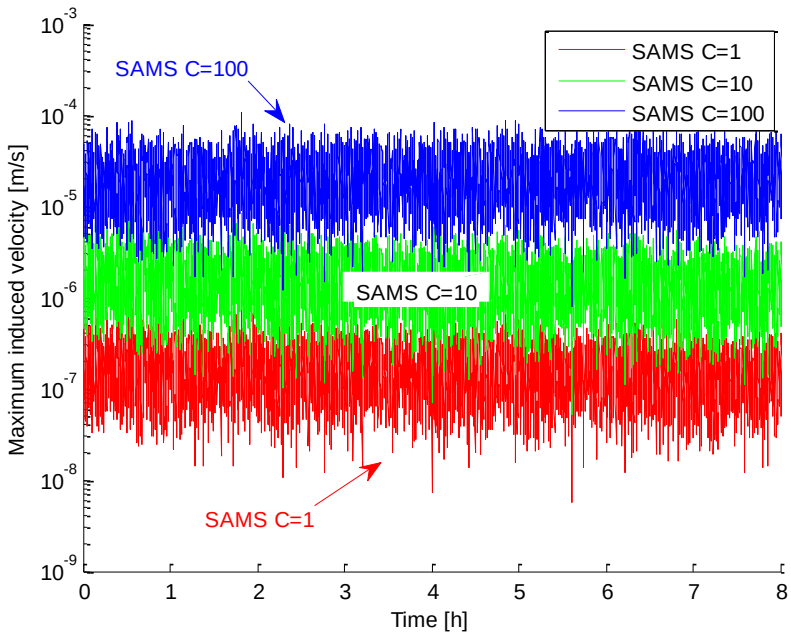

Figure 4-36: Maximum induced velocity in presence of scaled g-jitter

The sensitivity of the separation process to the g-jitter vibration is demonstrated in Figure 4-37. In this figure, the transient separation profile is shown for different scaling factors for the Max/Min interval method. As seen, the process is highly affected by the exaggerated g-jitter; the separation rate is reduced considerably, and about 73% of the ideal condition is obtained. When g-jitter is multiplied by 100, the deviation of the separation profile becomes extreme. In this case, some fluctuations appear on the curve. This figure represents the fact that the amplified g-jitter may affect the system. Such a condition may occur in non-nominal vibrational periods including spacecraft dockings or thruster ignition. Another possibility is that the accelerometers may not measure precisely the vibrations applied to the system due to structural damping.

In addition, according to Figure 4-37, fluctuation in the separation profile is not observed until large values of the scaling factor have been employed. In the case of C = 10, the separation is limited, but still a smooth curve is evident. The local disturbances in the separation rate are only observed at C = 100.

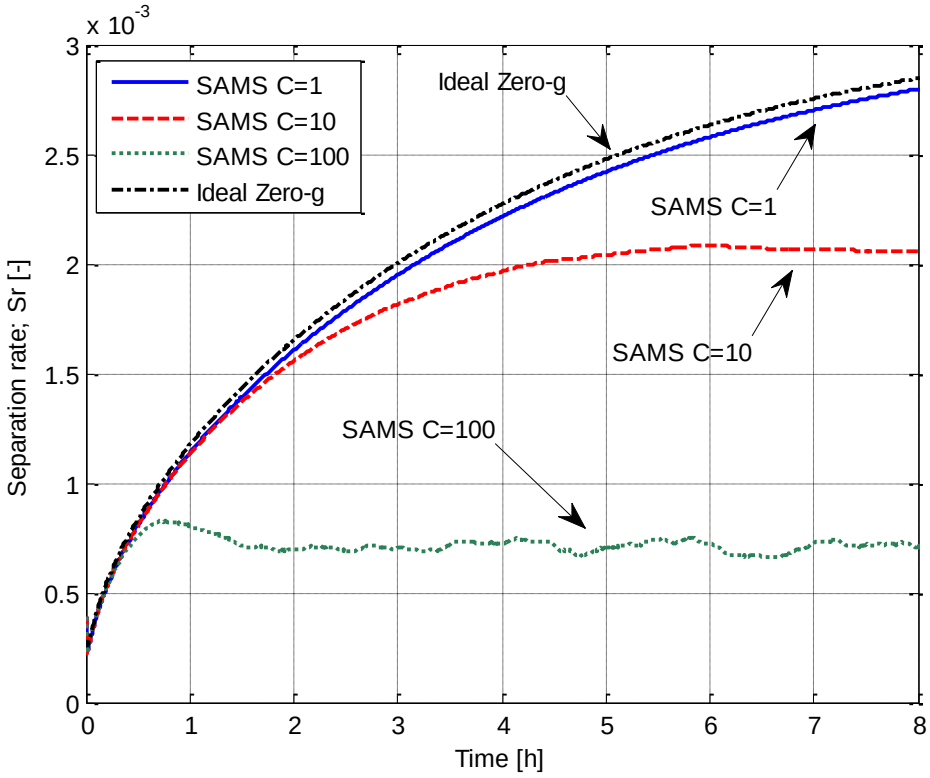

Figure 4-37: Transient separation profile in presence of scaled g-jitter

The concentration fields for cases of scaled g-jitter are shown in Figure 4-38 for C = 10 and C = 100. It is shown that a strong convection can form in the cell even in the case of vibratory data where the sign of accelerations changes rapidly. Indeed, the highly distorted concentration field for the case of C = 100 (Figure 4-38-(b)) is not realistic and is only the result of applying exaggerated vibrations.

For case of C = 10 (Figure 4-38-(a)), distortions in the concentration field are smoother. The distortions are even smaller for the scaling factors less than 10. The results show that the vibrational characteristics of the ISS are in an acceptable range; however, they are close to a sensitive range. If the current accelerations increase by a factor of 10, the consequences would be devastating for the diffusion experiments.

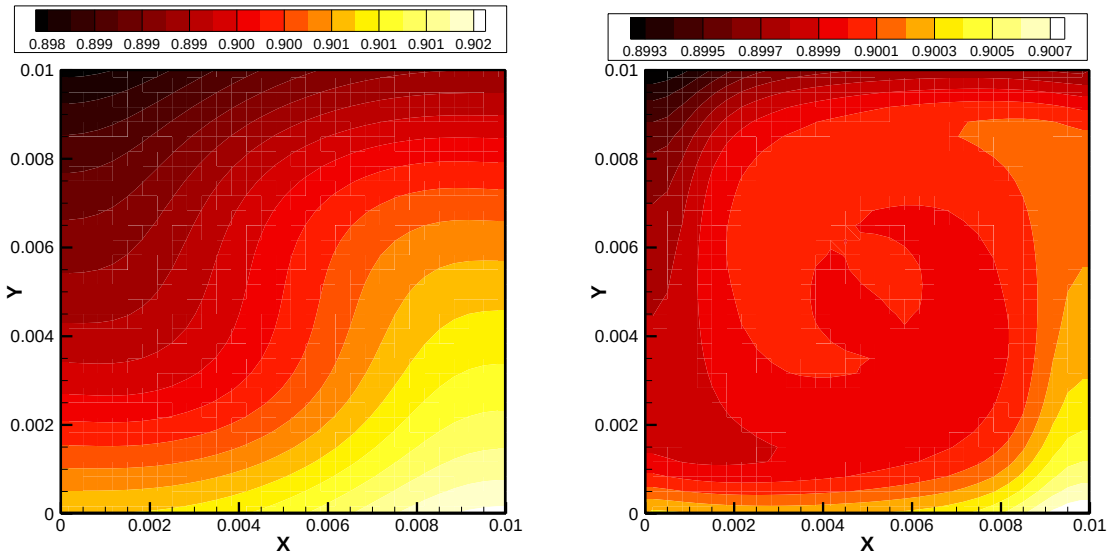

(a) SAMS C =10 (b) SAMS C =100

Figure 4-38: Contours of mass fraction of water for scaled g-jitter case (t=8h)

4.6.3 Low-frequency g –jitter

It is a fact that the system may not respond to the high-frequency vibrations. Earlier (4.4 Influence of oscillatory gravity) it was shown that the strength of the induced flow inside the cell is reduced considerably by increasing the frequency of vibrations. The SAMS accelerometers collect vibration data in the range of 0-300Hz. Nevertheless, it is believed that in the range of microgravity micro-accelerations, oscillations with frequency of higher than 10 Hz may not affect the system at all. Consequently, there is an interest to extract the low frequency contribution of g-jitter and determine its effect on the diffusion process.

In previous Chapter it was shown that this can be achieved by evaluating the Power Spectral Density (PSD) using a Fourier transform. Accordingly, the low-frequency contribution of the g-jitter has been extracted and is used in our CFD simulations. The acceleration data (extracted with this methodology) are all positive in sign. As discussed earlier this may not be the proper interpretation of the real conditions, but it allows some explanation for the deviations in the separation curves. The low-frequency contribution of g-jitter vibration during the IVIDIL-run2 is plotted in

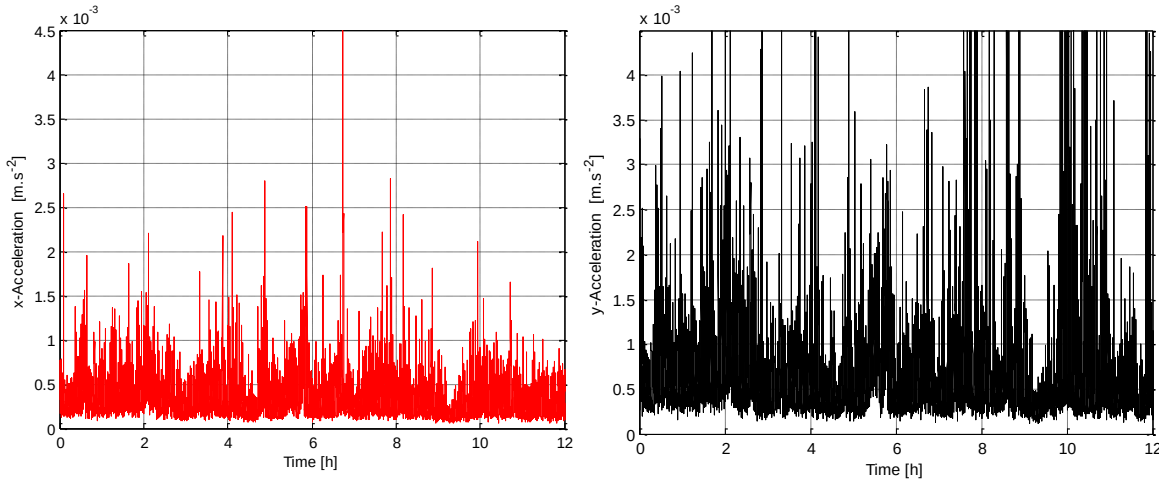

Figure 4-39. As shown, the amplitude of the acceleration is small compared to the original g-jitter since the data are integrated in the range of 0 – 10 Hz.

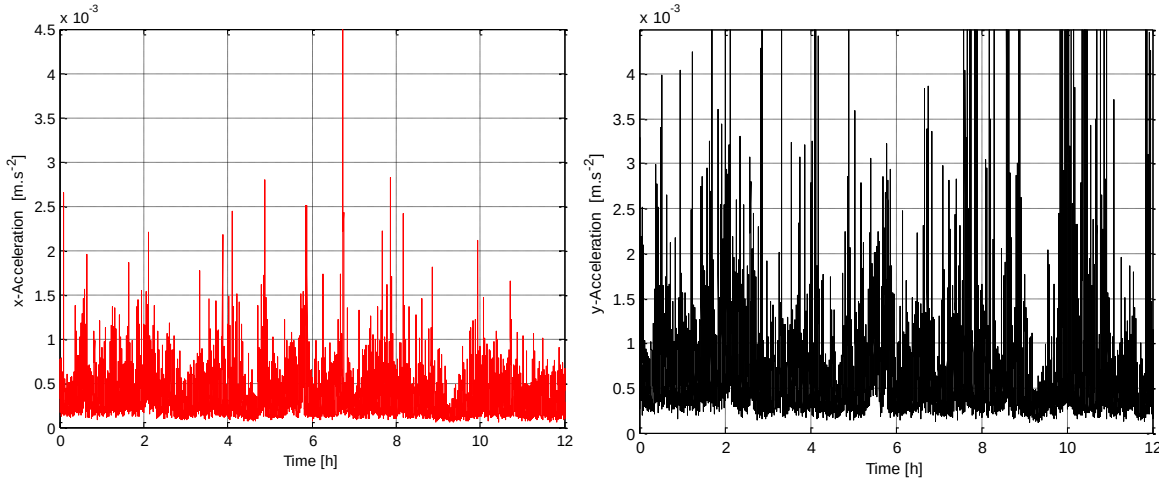

Figure 4-39: Low-frequency (0-10Hz) contribution of g-jitter during IVIDIL-run2

The effect of low-frequency g-jitter is studied by considering scale factors in order to exaggerate the situation. The maximum value of the induced velocity is illustrated in Figure 4-40 for these conditions. As shown, the original low-frequency g-jitter has resulted in a weak flow inside the cell ($\sim 10^{-7}\,\frac{m}{s^2}$). The maximum values of the velocity for the exaggerated cases are obtained in higher ranges that can affect the diffusion process. The profile of maximum velocity follows the spikes of the applied acceleration.

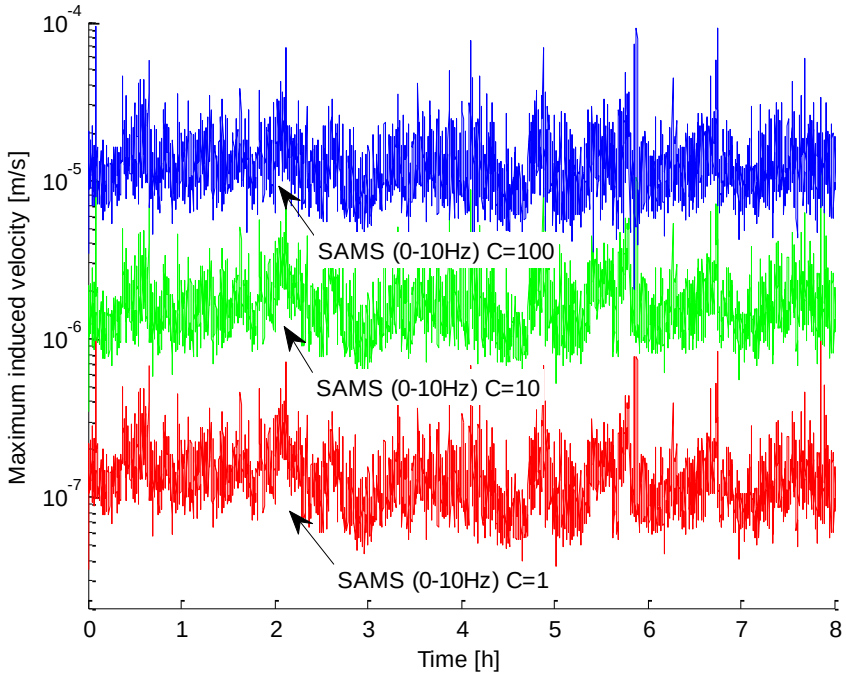

Figure 4-40: Maximum induced velocity in presence of the low-frequency contribution of g-jitter

The effect of the low-frequency g-jitter on the separation rate is shown in Figure 4-41. When low-frequency g-jitter (C = 1) is used, the separation process is slightly deviated from the ideal case. A stable convection cell forms in the system similarly to the case of static gravity. This structure can affect the diffusion process depending on its strength.

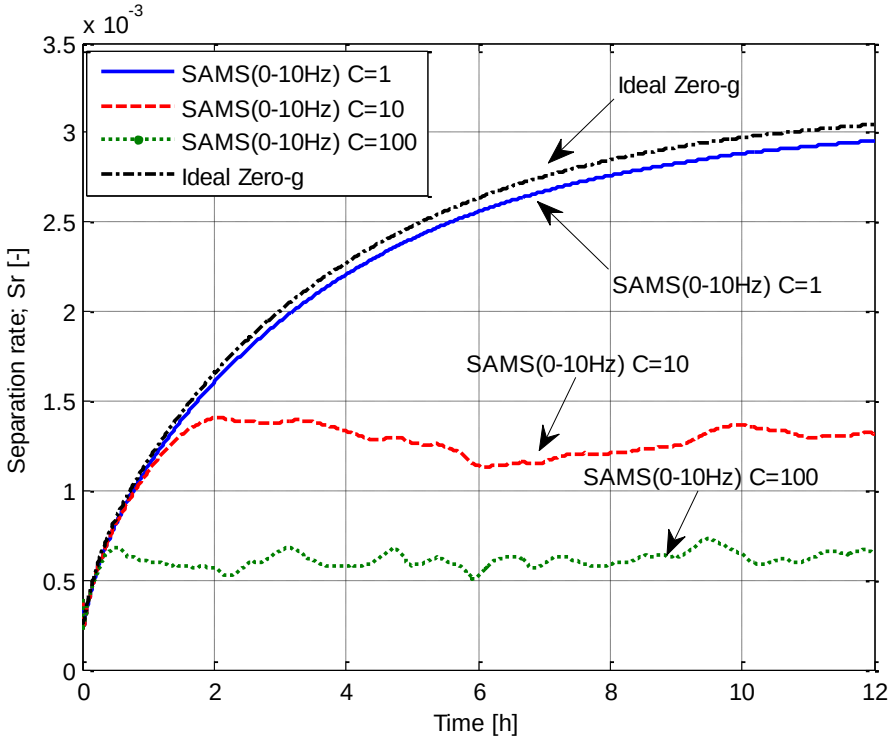

Figure 4-41: Transient separation profile in presence of the low-frequency contribution of g-jitter

Earlier in this chapter (4.3 Influence of residual gravity), it was shown that the diffusion process (for the current mixture and $\Delta T = 5$ °C) is affected for residual gravity higher than 5E-4. Interestingly, the mean value of the low-frequency g-jitter is on the same order of magnitude. When the low-frequency g-jitter is multiplied with the scale factors, the results are highly deviated from the original case. Remarkably, fluctuations in the separation curve are observed for C = 10. The distortions in the curve of C = 100 are very large, as the amplitude of the applied acceleration becomes higher.

Comparison between the last figure and the experimental results of the IVIDIL project (Figure 4-25) is eye-catching. As mentioned earlier, there is a remarkable deviation in the experimental trend which starts at t = 5 h and lasts until t = 8 h.

In Figure 4-41 the same phenomenon is observed for the case of C = 10 (dashed line). For this curve, there is a noteworthy change in the slope of the curve at t = 2 h, which lasts until t = 4 h. One can mark the same behaviour in the experimental results (Figure 4-25) in the same location.

The acceleration data representing the low-frequency g-jitter are all positive in sign and may not reflect the real conditions of the microgravity environment. When the original values are used, the separation rate is close to the ideal (experimental) case. However, when exaggerated by a factor of 10, some similarities between the numerical and experimental results were obtained. In fact, these similarities are in the local disturbances that occur in the main trend of the separation. This might indicate the role of low-frequency g-jitter vibrations on the thermodiffusion experiments. Such a connection has not been observed when other accelerations are used, e.g. full range frequency of the g-jitter and quasi-steady vibrations.

Thus, this study presents evidence that the fluctuations in the species separation are related to the low-frequency contribution of the g-jitter. More investigation is needed to verify this assertion. Fundamentally, acceleration measurements with cut-off

frequencies of a few hertz (0 – 10 Hz) are valuable. Comparing more CFD simulations with more experimental results will also provide more information in this regard. Unfortunately, at the time of preparing this dissertation only a few experimental results of the IVIDIL project have been published.

Chapter 5 Conclusion and Recommendations

5.1 Conclusion

Absolutely "undisturbed" experimental conditions are a prerequisite for thermodiffusion experiments. Very small disturbances due to buoyancy driven flows can highly affect the results. Thermodiffusion measurements can be performed on a space platform benefiting from the long-term weightlessness conditions found there. However, unavoidable micro-accelerations onboard space vehicles are still a concern. A considerable amount of research has been devoted to this field. Fundamentally, the accelerations are categorized to residual (static) and vibratory (g-jitter). The study of g-jitter vibrations has been performed by many researchers; although, in most of them g-jitter has been simplified to single or multi-frequency sinusoidal vibrations.

This study has investigated a typical thermodiffusion experiment subjected to different gravity fields. A second-order numerical code was developed to solve the unsteady governing equations.

For the case of static (residual) gravity field, a single convection cell is formed in the cell, which disturbs the concentration field depending on its strength. Various simulations were performed and a critical Rayleigh number of 1 is proposed, beyond which the process is dominated by convection. The variation of the average Nusselt number in the critical range is very small and the number cannot be used to evaluate the creditability of the thermodiffusion experiments.

For the case of a purely vibratory gravity field, the fluid flow is governed by the amplitude and frequency of the vibration. Different average flow regimes have been identified. When frequency increases, the convection effects diminish. The separation rate of the species is also affected by the average flow. The relation between the Gershuni (vibrational Rayleigh) and the separation rate is not linear. However, it was found that when the Gershuni number is below 20 the process is completely governed by the diffusion. Further increase in Gershuni number triggers the mixing effect. Moreover, other simulations have been performed to study the IVIDIL project that was performed onboard ISS in late 2009.

Simulation of a real microgravity condition was accomplished by considering real ISS acceleration data that was recorded during one of the IVIDIL experiments. Both quasi-steady and g-jitter accelerations were investigated. It was found that the influence of the quasi-steady vibrations is very small and in fact they cannot perturb the system even when amplified by a factor of 10. G-jitter vibrations have been surveyed by considering various methodologies. The interval RMS method is not suitable in preparation of raw acceleration data for CFD simulations. The role of the full-frequency range of g-jitter on thermodiffusion experiment is minimal.

Additionally, the low-frequency contribution of g-jitter has been extracted and used in the simulations. Although the processed acceleration data may not be the best interpretation of real condition, certain relations between the experimental and numerical results were monitored. This would suggest the significant role of low-frequency g-jitter vibration on the thermodiffusion experiments.

5.2 Recommendations

This study has investigated the effects of different gravity fields on a thermodiffusion problem in detail. Thus, following studies are suggested for future investigations.

- In terms of CFD modeling, expanding the capability of the code to model 3-D flows is recommended in order to investigate on the possible 3D effects of g-jitter.

- Theoretical work is needed for a better understanding of the thermo-vibrational flows. More specifically more appropriate dimensionless numbers to relate the separation rate is required.

- Numerical study of other mixtures such as water-IPA (50:50 wt.%) under the influence of oscillatory vibrations is suggested, which can be insightful since the results can be compared with the experimental data of IVIDIL.

- More detailed study on the effects of g-jitter would be of interest. Further investigation on the proposed connection between the low-frequency contribution of g-jitter and the component separation rate, which essentially needs better methodologies for data extraction is recommended.

Appendices

Appendix A: MATLAB code to generate acceleration for the CFD code

```
%Raw_to_mat.m
%% Vibration raw data to MAT files
tic
clear
clc
close all
% this folder should only holds the acceleration raw data
basefolder='.\RUN2 - Cut\MAMS\';
 %% Calculation
s=1;
list=dir(basefolder);
for i=3:length(list)
    file_id(s,1)=cellstr(list(i).name);
    s=s+1;
end

for p=1:length(file_id)
     filename=[basefolder char(file_id(p))];
     fid = fopen(filename);
    [A b] = fread(fid,'float32');
 caption= sscanf(char(file_id(p)),
'%d_%d_%d_%d_%d_%f+%d_%d_%d_%d_%d_%f.es08');
 caption=caption';
 s=1;
 %Zeros Definition;
  data=zeros(b/4,4);
  time=zeros(b/4,6); %*caption(1:6);
 % sorting the data
  for i=1:b/4
        data(i,1)=A(4*i-3);
        data(i,2)=A(4*i-2);
        data(i,3)=A(4*i-1);
        data(i,4)=A(4*i-0);
        time(i,:)=caption(1:6);
        time(i,6)=time(i,6)+data(i,1); %+0.002*(i-1);
  end
time=datecorrector(time);
save([num2str(p) '.mat'], 'time', 'data')
end
toc

%Function Date corrector; Corrects the date id of the data
function [ time ] = datecorrector( time )
[m n]=size(time);
for i=1:m
date=time(i,:);
date(5)=fix(date(6)/60)+date(5);
date(4)=fix(date(5)/60)+date(4);
date(3)=fix(date(4)/24)+date(3);
date(6)=date(6)-fix(date(6)/60)*60;
date(5)=date(5)-fix(date(5)/60)*60;
date(4)=date(4)-fix(date(4)/24)*24;
time(i,:)=date;
end
```

```
%data_cfd_write.m
%% Writing the acceleration data for CFD code
clc
close all
fclose all;
clear all
tic
basefolder='.\Vib_data\MATs\Run2\'; % Folder that have raw data (MAT)
write_folder='.\Vib_data\CFD\Run2\'; % Output folder; CFD ASCII files
dt_sample=0.002;
dt_cfd_code=1;

%% Indication of the outputs
EXPORT =[1 1 1 1]; % results to be written [RMS AVE MIN/MAX RMS_AVE]
                   %1 writes the data, 0 skip
g0=9.81;  % g0 value
max_line=200000;  % maximum line of CFD code reader

%% Calculations
N_points=fix(dt_cfd_code/dt_sample)+1;
N_writes=fix(dt_sample/dt_cfd_code);
s=max_line;
count=0.0;
File_id=10;
mkdir(write_folder);
mkdir([write_folder 'rms']);
mkdir([write_folder 'ave']);
mkdir([write_folder 'maxmin']);
mkdir([write_folder 'rms_ave']);

for i=1:length(dir(basefolder))-2;
    load ([basefolder num2str(i) '.mat']);
    %% Demean process
    ACC=data(:,2:4);
    ADD=sum(ACC)/length(ACC);
    for p=1:length(ACC);
        ACC(p,:)=(ACC(p,:)-ADD)*g0;
    end
     %% Calculation of data points for the intervals
    for k=1:N_points:length(data)-N_points
        sumX=0.0;
        sumY=0.0;
        sumX2=0.0;
        sumY2=0.0;
        X_acc=zeros(N_points,1);
        Y_acc=zeros(N_points,1);
        for j=0:N_points-1
            sumX=sumX+ACC(k+j,3); %X = z for SAMS
            sumY=sumY+ACC(k+j,1); % Y = x of SAMS
            sumX2=sumX2+ACC(k+j,3)^2;
            sumY2=sumY2+ACC(k+j,1)^2;
            X_acc(j+1)=ACC(k+j,3);
            Y_acc(j+1)=ACC(k+j,1);
        end
        % RMS
        rmsX=sqrt(sumX2/N_points);
        rmsY=sqrt(sumY2/N_points);
        % AVE
        aveX=sumX/N_points;
        aveY=sumY/N_points;
```

```
        % MIN / MAX
        [X_max l]=max(abs(X_acc));
        X_max=X_max*sign(X_acc(l));
        [Y_max l]=max(abs(Y_acc));
        Y_max=Y_max*sign(Y_acc(l));

        %% Creating new text files when reaching 200,000
        if s==max_line
            fclose('all');
            if (EXPORT(1)== 1)
                fid1 = fopen([write_folder
'rms\rms_',num2str(File_id),'.in'],'w');
                fprintf(fid1,'%d \n', max_line);
            end

            if (EXPORT(2)== 1)
                fid2 = fopen([write_folder
'ave\rms_',num2str(File_id),'.in'],'w');
                fprintf(fid2,'%d \n', max_line);
            end

            if (EXPORT(3)== 1)
                fid3 = fopen([write_folder
'maxmin\rms_',num2str(File_id),'.in'],'w');
                fprintf(fid3,'%d \n', max_line);
            end

            if (EXPORT(4)== 1)
                fid4 = fopen([write_folder
'rms_ave\rms_',num2str(File_id),'.in'],'w');
                fprintf(fid4,'%d \n', max_line);
            end
            File_id=File_id+1;
            s=0;
            %Defining Storing variables

            if File_id>11;
                save([write_folder num2str(File_id-11) '.mat'],
'TIME','RMS','AVE','MAX_VAL','RMS_AVE')
            end

            TIME=zeros(max_line,1);
            RMS=zeros(max_line,2);AVE=zeros(max_line,2);
            MAX_VAL=zeros(max_line,2);RMS_AVE=zeros(max_line,2);

        end


        %% Writing the results into text file
        for o=1:N_writes
            if (EXPORT(1)== 1)
                fprintf(fid1,'%e \t %e \t \n',rmsX,rmsY);end;
            if (EXPORT(2)== 1)
                fprintf(fid2,'%e \t %e \t \n',aveX,aveY);end;
            if (EXPORT(3)== 1)
                fprintf(fid3,'%e \t %e \t \n',X_max,X_max);end;
            if (EXPORT(4)== 1)
                fprintf(fid4,'%e \t %e \t
\n',rmsX*sign(aveX),rmsY*sign(aveY));end;
```

```
            s=s+1;
            %% Storing the calculated results
            count=count+1;
            TIME(s)=count*dt_cfd_code;
            RMS(s,1)=rmsX;
            RMS(s,2)=rmsY;
            AVE(s,1)=aveX;
            AVE(s,2)=aveY;
            MAX_VAL(s,1)=X_max;
            MAX_VAL(s,2)=Y_max;
            RMS_AVE(s,1)=rmsX*sign(aveX);
            RMS_AVE(s,2)=rmsY*sign(aveY);
        end
    end
            fprintf('Files to be done= %d \n',
length(dir(basefolder))-2-i)
end

if (EXPORT(1)== 1); frewind(fid1);fprintf(fid1,'%06d',s);end;
if (EXPORT(2)== 1); frewind(fid2);fprintf(fid2,'%06d',s);end;
if (EXPORT(3)== 1); frewind(fid3);fprintf(fid3,'%06d',s);end;
if (EXPORT(4)== 1); frewind(fid4);fprintf(fid4,'%06d',s);end;
TIME=TIME(1:s);RMS=RMS(1:s,:);AVE=AVE(1:s,:);MAX_VAL=MAX_VAL(1:s,:);RM
S_AVE=RMS_AVE(1:s,:);
save([write_folder num2str(File_id-10) '.mat'],
'TIME','RMS','AVE','MAX_VAL','RMS_AVE')
fclose('all');
toc

%% Plotting the results
for i =1:File_id-10
    load ([write_folder num2str(i)])
    figure(1)
    plot(TIME/3600,MAX_VAL(:,1),'k')
    hold on
    plot(TIME/3600,RMS_AVE(:,1),'r')
    plot(TIME/3600,RMS(:,1),'b')
    plot(TIME/3600,AVE(:,1),'g')
    figure(2)
    plot(TIME/3600,MAX_VAL(:,2),'k')
    hold on
    plot(TIME/3600,RMS_AVE(:,2),'r')
    plot(TIME/3600,RMS(:,2),'b')
    plot(TIME/3600,AVE(:,2),'g')
end

 figure(1);legend('Max/Min','RMS-AVE','RMS','AVE')
 figure(2);legend('Max/Min','RMS-AVE','RMS','AVE')
```

Appendix B: Executing the CFD code

The code is written in FORTRAN language. Thus there is no graphical user interface for the user. However, the executing the code is rather easy and straight forward. The code is designed to read the files and options through the input text files. Nevertheless, the input parameters should be provided in accordance to the information provided in below.

Three folders should be provided for the code; Input, Results and Errors. The input folder holds 5 input files named as casein.txt, kill.txt, material.txt, sol_control.txt and vibdata.txt which are described in below.

- casein.txt: holds the information about the physical dimensions, boundary condition, the total time of simulation, outputs and etc.

- kill.txt: Is to cease the calculation. Put 1 instead of 0 to stop the program.

-Material.txt: material properties should be provided in this file.

- sol_control.txt: Set the relaxation factors and convergence criteria in this file.

- vibdate.txt: The gravity field is set in this file that can be either a constant, sinusoidal function or raw g-jitter.

In case of choosing g-jitter, raw data of g-jitter should be provided in the input folder in ASCII format. The filenames should be in format of "rms_NN", in which NN is the 2 digit indicator starting from 10. The files should be successively numbered. Each file can have at most 200,000 lines. The number of data should be written in the first line. The acceleration data has to be written afterward with two components (x,y) in each line.

The results of the code will be written in the results folder. In case of any error in convergence, it will be reported in the error folder. The code writes a file named RESTART each time it exports a solution file. The user can reinitialize the code using this file. In that case, the RESTART file should be renamed to RESTART_IN and the proper option should also set in casein.txt.

The code is provided in the softcopy.

Bibliography

[1] C. Soret, on the equilibrium state of solutions with two parts kept at different temperatures, Archives des Sciences Physiques et Naturelles de Genve. II (1879).

[2] L.J.T.M. Kempers, A comprehensive thermodynamic theory of the Soret effect in a multicomponent gas, liquid, or solid, J. Chem. Phys. 115 (2001) 6330-6341.

[3] P. Costesèque, A. Mojtabi, J.K. Platten, Thermodiffusion phenomena, Comptes Rendus Mécanique. 339 (2011) 275-279.

[4] A. Mialdun, V. Yasnou, V. Shevtsova, A. Koniger, W. Kohler, D.A.d. Mezquia, M.M. Bou-Ali, A comprehensive study of diffusion, thermodiffusion, and Soret coefficients of water-isopropanol mixtures, J. Chem. Phys. 136 (2012) 244512.

[5] J.K. Platten, The Soret Effect: A Review of Recent Experimental Results, Journal of Applied Mechanics. 73 (2006) 5-15.

[6] R. Monti, Physics of Fluids in Microgravity, Taylor & Francis, 2001.

[7] M. Sakurai, N. Ohishi, A. Hirata, Oscillatory thermocapillary convection features in a liquid bridge under normal gravity and microgravity conditions—Drop shaft experiments, Advances in Space Research. 24 (1999) 1379-1384.

[8] T. Carlberg, Floating zone experiments with germanium crystals in sounding rockets, Acta Astronaut. 13 (1986) 639-643.

[9] V. Pletser, Short duration microgravity experiments in physical and life sciences during parabolic flights: the first 30 ESA campaigns, Acta Astronaut. 55 (2004) 829-854.

[10] R. Roşu-Pflumm, W. Wendl, G. Müller-Vogt, S. Suzuki, K.-. Kraatz, G. Frohberg, Diffusion measurements using the shear cell technique: Investigation of the role of Marangoni convection by pre-flight experiments on the ground and during the Foton M2 mission, Int. J. Heat Mass Transfer. 52 (2009) 6042-6049.

[11] R. Savino, D. Paterna, Compatibility of the microgravity environment of the international space station with fluid and material science experimentation, Acta Astronaut. 51 (2002) 229-241.

[12] P. Baglioni, R. Demets, A. Verga, ESA payloads and experiments on the Foton-12 mission. (2000).

[13] S. Mazzoni, V. Shevtsova, A. Mialdun, D. Melnikov, Y. Gaponenko, T. Lyubimova, M.Z. Saghir, Vibrating liquids in space, Europhys. News. 41 (2010) 14-16.

[14] M. Touzet, G. Galliero, V. Lazzeri, M.Z. Saghir, F. Montel, J. Legros, Thermodiffusion: From microgravity experiments to the initial state of petroleum reservoirs, Comptes Rendus Mécanique. 339 (2011) 318-323.

[15] J.O. Hirschfelder, C.F. Curtiss, R.B. Bird, Molecular Theory of Gases and Liquids, Wiley, 1964.

[16] B. Hafskjold, Computer simulations of thermal diffusion in binary fluid mixtures, in: Anonymous Thermal Nonequilibrium Phenomena in Fluid Mixtures, Springer, Berlin, New York, 2002, pp. 2-23.

[17] J.M. Simon, D.K. Dysthe, A.H. Fuchs, B. Rousseau, Thermal diffusion in alkane binary mixtures: A molecular dynamics approach, Fluid Phase Equilib. 150–151 (1998) 151-159.

[18] C. Nieto-Draghi, J.B. Avalos, B. Rousseau, Computing the Soret coefficient in aqueous mixtures using boundary driven nonequilibrium molecular dynamics, J. Chem. Phys. 122 (2005) 114503.

[19] R. Haase, Therrnodynamics of Irreversible Processes, Addison Wesley, 1969.

[20] E.L. Dougherty, H.G. Drickamer, A Theory of Thermal Diffusion in Liquids, J. Chem. Phys. 23 (1955) 295-309.

[21] A. Firoozabadi, K. Ghorayeb, K. Shukla, Theoretical model of thermal diffusion factors in multicomponent mixtures, AICHE J. 46 (2000) 892-900.

[22] J. Luettmer-Strathmann, Lattice Model for Thermodiffusion in Polymer Solutions, Int. J. Thermophys. 26 (2005) 1693-1707.

[23] M. Eslamian, M.Z. Saghir, Microscopic study and modeling of thermodiffusion in binary associating mixtures, Physical Review E. 80 (2009) 061201.

[24] M. Eslamian, M.Z. Saghir, Dynamic thermodiffusion model for binary liquid mixtures, Physical Review E. 80 (2009) 011201.

[25] M. Eslamian, M.Z. Saghir, M.M. Bou-Ali, Investigation of the Soret effect in binary, ternary and quaternary hydrocarbon mixtures: New expressions for thermodiffusion factors in quaternary mixtures, International Journal of Thermal Sciences. 49 (2010) 2128-2137.

[26] M. Eslamian, M.Z. Saghir, Modeling of DNA thermophoresis in dilute solutions using the non-equilibrium thermodynamics approach, J. Non Equilib. Thermodyn. 37 (2012) 63-76.

[27] M. Eslamian, M.Z. Saghir, Thermodiffusion (thermomigration) and convection in molten semiconductor–metal layers, International Journal of Thermal Sciences. 50 (2011) 1232-1242.

[28] M. Eslamian, F. Sabzi, M.Z. Saghir, Modeling of thermodiffusion in liquid metal alloys, Physical Chemistry Chemical Physics. 12 (2010) 13835-13848.

[29] M. Eslamian , Advances in thermodiffusion and thermophoresis (Soret effect) in liquid mixtures, Frontiers in Heat and Mass Transfer (FHMT). 2 (2011).

[30] W. Kohler, S. Wiegand, U. Bayreuth , Thermal Nonequilibrium Phenomena in Fluid Mixtures, Springer, 2002.

[31] S. Pan, M.Z. Saghir, M. Kawaji, C.G. Jiang, Y. Yan, Theoretical approach to evaluate thermodiffusion in aqueous alkanol solutions, J. Chem. Phys. 126 (2007) 014502.

[32] A. Abbasi, M.Z. Saghir, M. Kawaji, A new proposed approach to estimate the thermodiffusion coefficients for linear chain hydrocarbon binary mixtures, J. Chem. Phys. 131 (2009) 014502.

[33] K. Ghorayeb, A. Firoozabadi, Molecular, pressure, and thermal diffusion in nonideal multicomponent mixtures, AICHE J. 46 (2000) 883-891.

[34] S. Srinivasan, M.Z. Saghir, Experimental approaches to study thermodiffusion – A review, International Journal of Thermal Sciences. 50 (2011) 1125-1137.

[35] B.D. Butler, J.C.R. Turner, Flow-cell studies of thermal diffusion in liquids: Part 1. - Cell construction and calibration, Transactions of the Faraday Society. 62 (1966) 3114-3120.

[36] A. Mialdun, V.M. Shevtsova, Development of optical digital interferometry technique for measurement of thermodiffusion coefficients, Int. J. Heat Mass Transfer. 51 (2008) 3164-3178.

[37] A. Mialdun, V. Shevtsova, Digital interferometry as a powerful tool to study the thermodiffusion effect, Comptes Rendus Mécanique. 339 (2011) 362-368.

[38] V. Shevtsova, IVIDIL experiment onboard the ISS, Advances in Space Research. 46 (2010) 672-679.

[39] V. Shevtsova, T. Lyubimova, Z. Saghir, D. Melnikov, Y. Gaponenko, V. Sechenyh, J.C. Legros, A. Mialdun, IVIDIL: on-board g-jitters and diffusion controlled phenomena, International Symposium on Physical Sciences in Space. 327 (2011) 012031.

[40] A. Kianian, A. Ahadi, M.Z. Saghir, Experimental Evidence of Low Rayleigh Vibration on Mixture during Thermodiffusion Experiment, The Canadian Journal of Chemical Engineering. (Submitted).

[41] J. Alexander, Low-gravity experiment sensitivity to residual acceleration: A review, Microgravity Sci. Technol. 3 (1990).

[42] G.Z. Gershuni, Thermal Vibrational Convection, John Wiley & Sons, New York, 1998.

[43] G.Z. Gershuni, E.Z. Zhukhovitskii, Vibration induced thermal convection in weightlessness, Fluid Mechanics. 15 (1986) 63-84.

[44] R. Monti, R. Savino, A new approach to g-level tolerability for fluid and material science experiments, Acta Astronaut. 37 (1995) 313-331.

[45] R. Savino, R. Monti, Convection induced by residual-g and g-jitters in diffusion experiments, Int. J. Heat Mass Transfer. 42 (1999) 111-126.

[46] R. Monti, R. Savino, M. Lappa, On the convective disturbances induced by g-jitter on the space station, Acta Astronaut. 48 (2001) 603-615.

[47] R. Monti, D. Paterna, R. Savino, Counter-measures to mitigate residual-G effects on microgravity experiments on the space station, Acta Astronaut. 50 (2002) 209-216.

[48] R. Monti, R. Savino, The fluidynamic disturbances due to the microgravity environment prevailing on the International Space Station, First International Symposium on Microgravity Research & Applications in Physical Sciences and Biotechnology, Vols i and Ii, Proceedings. 454 (2001) 813-822.

[49] Y. Shu, B.Q. Li, H.C. De Groh, Numerical study of g-jitter induced double-diffusive convection, Numerical Heat Transfer, Part A: Applications. 39 (2001) 245-265.

[50] R. Savino, Residual-g and g-jitter effects on the measurement of thermophysical properties in microgravity, Advances in Space Research. 29 (2002) 559-568.

[51] M. Chacha, D. Faruque, M.Z. Saghir, J.C. Legros, Solutal thermodiffusion in binary mixture in the presence of g-jitter, International Journal of Thermal Sciences. 41 (2002) 899-911.

[52] M. Chacha, M.Z. Saghir, Solutal-thermo-diffusion convection in a vibrating rectangular cavity, International Journal of Thermal Sciences. 44 (2005) 1-10.

[53] T. Lyubimova, E. Shklyaeva, J.C. Legros, V. Shevtsova, B. Roux, Numerical study of high frequency vibration influence on measurement of Soret and diffusion coefficients in low gravity conditions, Advances in Space Research. 36 (2005) 70-74.

[54] S. Sharidan, N. Amin, I. Pop, G-jitter fully developed combined heat and mass transfer by mixed convection flow in a vertical channel, Int. Commun. Heat Mass Transfer. 32 (2005) 657-665.

[55] Y. Yan, V. Shevtsova, M.Z. Saghir, Numerical Study of Low Frequency G-jitter Effect on Thermal Diffusion, FDMP: Fluid Dynamics & Materials Processing. 1 (2005) 315-328.

[56] Y. Yan, A. Viviani, M.Z. Saghir, Double diffusion convection under sinusoidal modulations of low-frequency vibrations, Acta Astronaut. 63 (2008) 665-672.

[57] Y. Yan, K. Jules, M.Z. Saghir, A Comparative Study of G-jitter Effect on Thermal Diffusion aboard the International Space Station, FDMP: Fluid Dynamics & Materials Processing. 3 (2007) 231-246.

[58] Y. Yan, S. Pan, K. Jules, M. Saghir, Vibrational effect on thermal diffusion under different microgravity environments, Microgravity Science and Technology. 19 (2007) 12-25.

[59] V. Shevtsova, D. Melnikov, J.C. Legros, Y. Yan, Z. Saghir, T. Lyubimova, G. Sedelnikov, B. Roux, Influence of vibrations on thermodiffusion in binary mixture: A benchmark of numerical solutions, Phys. Fluids. 19 (2007) 017111.

[60] S. Srinivasan, M. Dejmek, M.Z. Saghir, Thermo-solutal-diffusion in high pressure liquid mixtures in the presence of micro-vibrations, International Journal of Thermal Sciences. 49 (2010) 1613-1624.

[61] A.H. Ahadi, M.Z. Saghir, Quasi Steady State Effect of Micro Vibration from Two Space Vehicles on Mixture During Thermodiffusion Experiment, FDMP; Fluid Dynamics and Material Processing. 287 (2012).

[62] A. Firoozabadi, Thermodynamics of Hydrocarbon Reservoirs, McGraw-Hill, 1999.

[63] D. Peng, D.B. Robinson, A New Two-Constant Equation of State, Industrial & Engineering Chemistry Fundamentals. 15 (1976) 59-64.

[64] J. Gross, G. Sadowski, Perturbed-Chain SAFT: An Equation of State Based on a Perturbation Theory for Chain Molecules, Ind Eng Chem Res. 40 (2001) 1244-1260.

[65] A. Parsa, S. Srinivasan, M.Z. Saghir, Impact of density gradients on the fluid flow inside a vibrating cavity subjected to soret effect, The Canadian Journal of Chemical Engineering. (2012).

[66] V. Shevtsova, I. Ryzhkov, D. Melnikov, Y. Gaponenko, A. Mialdun, Experimental and theoretical study of vibration-induced thermal convection in low gravity, J. Fluid Mech. 648 (2010) 53.

[67] K. Jules, K. McPherson, K. Hrovat, E. Kelly, T. Reckart, A status report on the characterization of the microgravity environment of the International Space Station, Acta Astronaut. 55 (2004) 335-364.

[68] Principal Investigator Microgravity Services (PIMS) Results Home Page, http://pims.grc.nasa.gov/pims_iss_index.html,.

[69] K. Jules, K. Hrovat, E. Kelly, Principal Investigator Microgravity Services (PIMS) International Space Station Increment-2 Quick Look Report May to June 2001, TM-211200 (2001).

[70] I.G. Currie, Fundamental Mechanics of Fluids, Marcel Dekker, 2003.

[71] R.W. Fox, A.T. McDonald, P.J. Pritchard, Introduction to Fluid Mechanics, Wiley, 2004.

[72] B. Gebhart, Buoyancy-Induced Flows and Transport, Hemisphere Pub. Corp, 1988.

[73] S.V. Patankar, Numerical Heat Transfer and Fluid Flow, Taylor & Francis, 1980.

[74] M.F. Alfradique, M. Castier, Critical points of hydrocarbon mixtures with the Peng–Robinson, SAFT, and PC-SAFT equations of state, Fluid Phase Equilib. 257 (2007) 78-101.

[75] F.H. Harlow, J.E. Welch, Numerical Calculation of Time-Dependent Viscous Incompressible Flow of Fluid with Free Surface, Phys. Fluids. 8 (1965) 2182-2189.

[76] T.J. Chung, Computational Fluid Dynamics, Cambridge University Press, 2010.

[77] G. De Vahl Davis, Natural convection of air in a square cavity: A bench mark numerical solution, Int. J. Numer. Methods Fluids. 3 (1983) 249-264.

[78] M.T. Manzari, An explicit finite element algorithm for convection heat transfer problems International Journal of Numerical Methods for Heat & Fluid Flow. 9 (1999) 860-877.

[79] Wei, D.,C.Wan, B.S.V.Patnaik, G.W., A new benchmark quality solution for the buoyancy-driven cavity by discrete singular convolution, Numer Heat Transfer Part B Fundam. 40 (2001) 199-228.